学位論文

A Systematic Study of Supernova Remnants in the Scutum Arm as Possible Sources of Low Energy Cosmic Rays

(低エネルギー宇宙線加速源の解明に向けた楯座腕超新星残骸の系統的な研究)

平成27年12月博士(理学)申請

東京大学大学院理学系研究科
物理学専攻
佐藤　有

Abstract

In order to deepen our understanding of supernova remnants (SNRs), we analyze X-ray spectra of four middle-aged SNRs in the Galactic Scutum Arm: 3C 391, Kes 79, Kes 78 and W44. The Large Area Telescope (LAT) onboard the Fermi Gamma-ray Space Telescope (Fermi) has discovered several GeV-bright SNRs as a new category of SNRs. Almost all GeV-bright SNRs are interacting with molecular clouds. X-ray observations have revealed that these SNRs often have over-ionized/recombining plasmas (RPs), which can not be explained by the standard evolution scenario. Whether the ambient dense molecular environment, which is common to these SNRs, gives rise to an irregular evolution or not still remains as an unsolved problem. An X-ray study of these SNRs can open a new window for discerning the production of low-energy cosmic ray (CR) protons at SNRs which cannot be directly measured at Earth.

We perform observations of the Scutum Arm SNRs with Suzaku, an X-ray astronomical satellite which has a superb sensitivity for observing fainter diffuse objects. The major background for observing Galactic SNRs is the Galactic ridge X-ray emission (GRXE), whose flux depends on the sky location. Since it is important to precisely model the GRXE, we select the adjacent GeV-bright SNRs in the Scutum Arm distant from Galactic Center. This region is suitable for a systematic study because we can deal with the relatively low GRXE by using an almost identical plasma emission.

From SNR 3C 391, we discover an RP for the first time. We also reveal that 3C 391 has a low-temperature plasma in collisional ionization equilibrium and a high-temperature ejecta dominant plasma whose origin is likely a $\sim$15–20 $M_{\odot}$ core-collapse supernova. No significant difference in the properties of the RP component is found between the east and west regions whose morphological structures are much different from each other. This result implies that the RP of 3C 391 is produced by an adiabatic cooling or ionization by low energy CRs.

We discover a neutral or lowly-ionized Fe Kα emission ($\sim$ 6.4 keV) from SNR Kes 79 with the significance level of 3.5σ. The emission shows a different spatial distribution from the SNR shell structure, but likely to associate with the location of strong ^{13}CO emission, implying that the most probable origin is an interaction with a molecular cloud. Kes 79 also has two plasma components with different temperatures. The metal abundance of the high temperature plasma indicates that the origin of Kes 79 is a 30–40 $M_{\odot}$ core-collapse supernova. Different from other GeV-bright SNRs, Kes 79 shows no emission feature of RP. We find that the apparent diameter of the low temperature plasma is twice as large as that of the high-temperature component through spacial and spectral analyses taking advantage of the low instrumental background

noise of Suzaku. We can interpret this morphology as the spatial distribution of the ejecta plasma heated by the reverse shock and interstellar materials thermalized by the forward shock.

With our discovery of a statistically significant 6.4 keV emission from Kes 79 and a strong hint of such from the others (3C 391, W44 and Kes 78) with 2.1σ–2.4σ, we proceed to discuss the possible physical origin(s) of this intriguing emission feature at the end of this thesis. The most plausible origin is an excitation of neutral iron by low energy CR-protons ($\sim$10 MeV) in a molecular cloud. Since Kes 79 is a GeV-bright SNR, GeV gamma-rays are likely emitted through the interaction between high energy CR-protons (> 280 MeV). The number density of the low energy CR-protons is lower than that extrapolated from the high energy CR-protons possibly due to a rapid ionization loss of the low energy CR-protons. We construct a time-dependent model to calculate the evolution of the momentum distribution of the CR-protons in the molecular cloud, which we find, can offer a simultaneous explanation to both the 6.4 keV and GeV gamma-ray spectrum. If we apply the model to Kes 79, we can calculate nt as $1.8^{+4.8}_{-1.3} \times 10^9$ cm^{-3} s^{-1}. This low nt is interpreted as that the molecular cloud is clumpy. If the origin of the 6.4 keV emission is the excitation by low energy CRs, the X-ray observation of the Fe Kα line becomes a direct probe of low energy CRs.

Contents

Chapter 1

Introduction

Recent observations over a wide band ranging from radio to X-ray and gamma-ray wavelengths contribute to advance study of supernova remnants (SNRs) for thermal plasma in extreme condition and for acceleration of cosmic-rays (CRs; Vink 2012). However, the evolution, which is the most fundamental framework for our understanding of SNRs, has not even been well established. Interactions with inhomogeneous molecular environments complicate the evolution and photon emission of SNRs (e.g. Ohira et al. 2011). For many middle-aged SNRs ($\sim 10^3$–10^4 yr) interacting with molecular clouds, the evolution of thermal plasma is beyond the standard theory (Yamaguchi et al. 2009) and CRs are efficiently accelerated to energies high enough to emit bright GeV gamma-rays (Abdo et al. 2010).

X-ray observations with the Suzaku satellite reveal the presence of overionized/recombining plasma (RP) in SNRs, which requires a modification of the conventional evolution scenario (IC443, Yamaguchi et al. 2009b; W49B, Ozawa et al. 2009; G359.1−0.5, Ohnishi et al. 2011; W28, Sawada & Koyama 2012; W44, Uchida et al. 2012; G346.6−0.2, Yamauchi et al. 2013). The RP has an ionization temperature ($T_{\rm Z}$) that are higher than an electron temperature ($T_{\rm e}$); $T_{\rm z}$ is a useful parameter that is defined as temperature which would be required to ionize the plasma to the same degree on the assumption that the plasma is in collisional ionization equilibrium (CIE). However, the conventional scenario predicts in reverse ($T_{\rm z} < T_{\rm e}$). These middle-aged SNRs are almost all GeV-bright SNRs which show bright radio shells and strong shock-cloud interactions. X-ray spectra of these SNRs also provide information on not only the evolution but also their births, i.e., supernova explosions (Uchida et al. 2013, Yasumi et al. 2014). The supernova type and progenitor mass can be estimated by X-ray observation from metal abundances of thin thermal plasma in SNRs compared to supernova nucleosynthesis models (e.g. Iwamoto et al. 1999, Woosley & Weaver (1995)).

The bright GeV gamma-rays from these SNRs are confirmed to be emission from accelerated CR-protons (Ackermann et al. 2013). Low energy CR-protons are also of importance for the

chemical evolution through the interaction between SNRs and molecular clouds (Schuppan et al. 2012). The Kα X-rays from neutral or lowly ionized matters in molecular clouds can directly probe low energy CRs from SNRs which are extremely important for completing our understanding of particle acceleration processes at astrophysical shocks, such as the injection mechanism. To investigate the evolution of SNRs, we need a systematic study of these middle-aged SNRs interacting with molecular clouds by using X-ray spectroscopy.

We perform observations of four middle-aged GeV-bright SNRs (3C 391, Kes 79, Kes 78 and W44) in the Galactic Scutum Arm with the X-ray satellite, Suzaku (Mitsuda et al. 2007). The XIS instruments onboard Suzaku have the capability of performing deep X-ray spectroscopic observations for diffuse X-ray objects including SNRs, taking advantage of the low and stable instrumental background (Koyama et al. 2007). The major background component for the Galactic SNRs is the Galactic ridge X-ray emission (GRXE), whose flux strongly depends on the location of SNRs (e.g. Sugizaki et al. 2001, Kaneda et al. 1997). Since it is important to precisely model the GRXE, we select four SNRs adjacent to us in the Scutum Arm region ($l \sim 30°$) where the X-ray background is one order-of-magnitude lower than that at the Galactic Center (Uchiyama et al. 2013). The selected SNRs are very suitable for a systematic study since they are very close to each other and hence have their backgrounds characterized by an almost identical GRXE emission. Figure 1.1 shows an X-ray image of the selected region obtained with the XIS in the energy range of 0.8–3.0 keV.

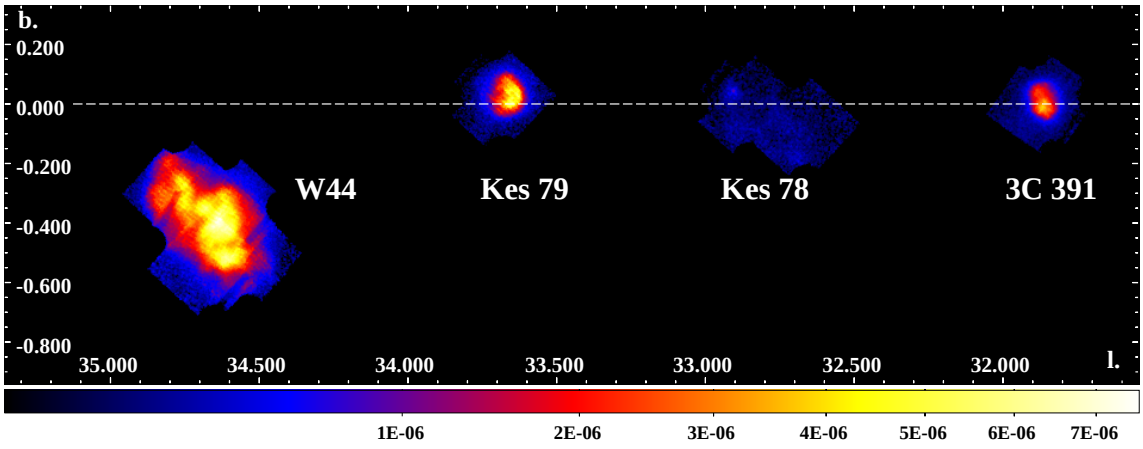

Figure 1.1: The 0.8-3.0 keV X-ray image of the selected Scutum Arm region in units of photons s^{-1} keV^{-1} cm^{-2}. The four SNRs we analyze are close to each other ($l \sim 32$–$35°$). The dashed line indicates $b = 0.0°$.

This dissertation is organized as follows. In Chapter 2, we review the evolution and emission properties of SNRs. In Chapter 3, we describe the observational instruments of Suzaku. We show the observation results for SNR 3C 391, Kes 79, Kes 78 and W44 in Chapter 4, 5, and 6,

respectively. In Chapter 7, we discuss the origin of a newly discovered ∼6.4 keV line from Kes 79 by constructing an evolution model for the interactions between the locally accelerated CRs and molecular clouds. Finally, I summarize the conclusion of these studies in Chapter 8.

Chapter 2

Review

Supernovae (SNe) are known as explosions of stars at the end of their lives. After the SN, a nebular-like astrophysical objects, supernova remnants (SNRs), are left behind. Supernova explosions are one of the most energetic events in the Universe and release bulk kinetic energy of about 10^{51} erg (1 erg $\sim 6 \times 10^{11}$ eV) into their surroundings. The remnants of the exploded stars ("ejecta") expand into the interstellar medium (ISM) at supersonic speeds and create strong collisionless shock waves. These strong shocks sweep up the ambient material outside. These swept-up matters as well as the ejecta are heated by the shocks up to X-ray-emitting temperatures. Many SNRs, such as Cassiopeia A (Figure 2.1; Stage et al. 2006), show rich morphological structures over the entire electromagnetic spectrum. Many of these features still do not have full explanations despite a continuous addition of multi-wavelength observations and theoretical models. In this chapter, we overview SNe and the physics of the evolution and radiation processes of SNRs.

2.1 Supernova Explosion

2.1.1 Classification of Supernovae

SNe are classified into two main categories, Type I and II, according to their optical spectra, as shown in Figure 2.2. Type I or II SNe are categorized by the absence or presence of hydrogen absorption lines, respectively (Minkowski 1939). Type I SNe are sub-categorized as Type Ia SNe if their optical spectra have strong Si lines, while Type Ib and Ic SNe show weak Si lines and they are considered to be produced by core-collapse SNe.

It is thought that Type Ia SN is caused by thermal runaway reaction in a binary system consisting of a near-Chandrasekhar mass white dwarf ($\sim 1.4 M_{\odot}$) and a giant star (single degenerate progenitors; e.g., Nomoto 1982). Another probable mechanism is that Type Ia SN

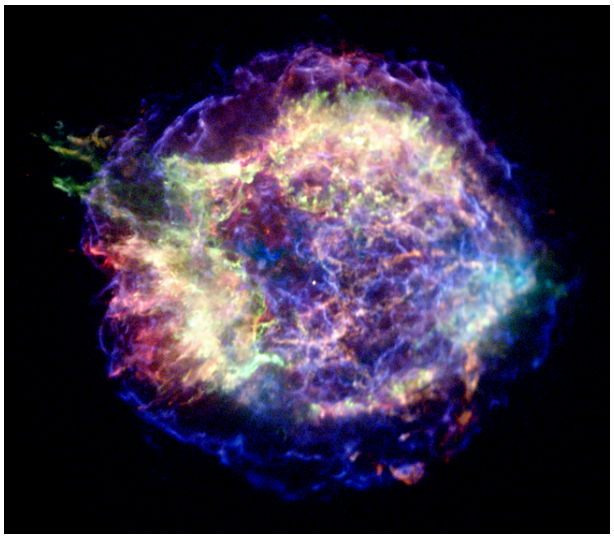

Figure 2.1: An X-ray image of SNR Cassiopeia A observed by the Chandra X-ray Observatory. The color coded energy bands are 0.5–1.5 keV (red), 1.5–2.5 keV (green) and 4.0–6.0 keV (blue).

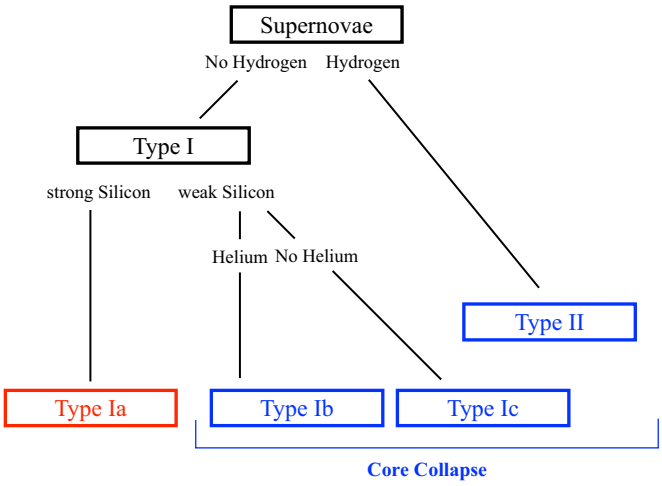

Figure 2.2: Classification scheme of supernovae based on their optical spectra.

is produced by the merger of two white dwarfs (double degenerate progenitors; e.g., Webbink 1984). In any case, SNRs of Type Ia have no compact objects at their center of explosion. Type Ia SNe are observed in all types of galaxies. In the case of single degenerate progenitors, since the energetics of Type Ia SNe are strongly restricted by the degeneracy pressure of electrons, they have been widely used as standard candles to measure cosmological parameters.

Since Type II SNe are mostly found at a star forming region in the spiral galaxy's arm, it is considered that the progenitor is a massive star ($>\sim 8M_{\odot}$). When the nuclear fusion is not able to sustain the core against its own gravity, the massive star undergoes core-collapse and explodes its outer layers. Then, the star collapses into a neutron star or a black hole. The total energy released by a Type II SN is $\sim 10^{53}$ erg, but the typical kinetic energy of the expanding ejecta is $\sim 10^{51}$ ergs and most of the explosion energy is carried by neutrinos. Type Ib and Ic SNe, sub-categories of Type I SNe, are also believed to be core-collapse SNe. While Type Ib show He emission, Type Ic does not show.

2.1.2 Nucleosynthesis

Nucleosynthesis is efficiently performed at the moment of the SNe. The metal abundances of a SN ejecta (SNR) depend on the type of SNe. Figure 2.3 shows the metal abundances of SNR SN1006 compared to SN nucleosynthesis models (Iwamoto et al. 1999, Woosley &Weaver 1995, Uchida et al. 2013). The Suzaku capability of performing deep X-ray spectroscopic enable us to precisely study the SN nucleosynthesis through the SNR observation. While the Type Ia SN shows higher abundances of heavy elements (Si–Fe) than light elements (O–Mg), the core-collapse SN with a high mass progenitor generates relatively low heavy elements (Thielemann et al. 1996).

2.2 Supernova Remnant

After the SN explosion, a supernova remnant (SNR) which consists of ejected material and swept-up ISM is formed. SNRs are mostly discovered by radio survey and up to now 294 SNRs are identified in total in our Galaxy (Green 2014). In addition, about half of them emit X-rays. In this section, we explain basic physics about SNR evolution as well as thermal/non-thermal X-ray emission. First we show a classification of SNRs. Then, we review the SNR evolution and X-ray emission mechanisms caused by heated materials.

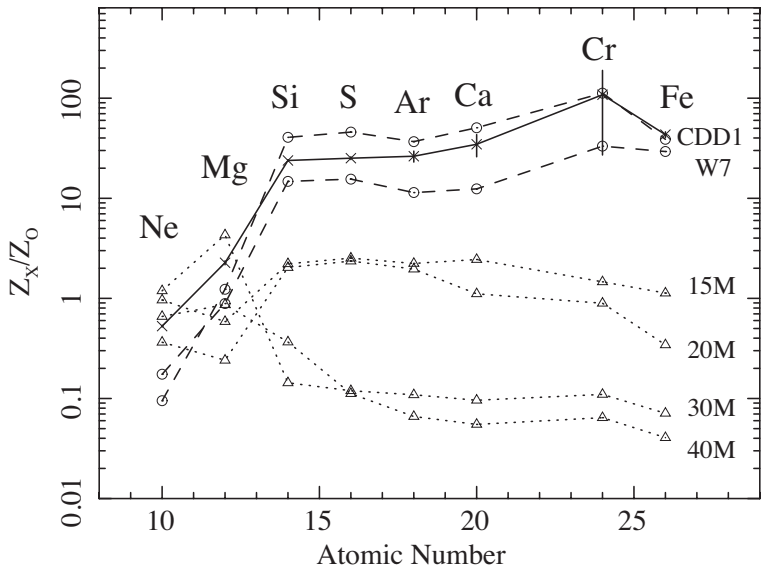

Figure 2.3: Metal abundances of SNR SN1006 relative to O as a function of atomic number. The dashed lines and circles represent the relative abundances of Type Ia models (CDD1, W7; Iwamoto et al. 1999). The dotted lines and triangles represent core-collapse models with progenitor masses of 15 $M_\odot$,20 $M_\odot$, 30 $M_\odot$ and 40 $M_\odot$, respectively (Woosley & Weaver 1995). This figure is taken from Uchida et al. (2013).

2.2.1 Classification of Supernova Remnants

SNRs are basically classified into three categories, shell type, Composite type and Plerion type, based on the radio emission structure. Among 294 SNRs which have been discovered since 2014 (Green 2014), 79%, 12% and 5% are classified as the shell type, Composite type and Plerion type, respectively. The types of the remaining 4% SNRs are not clear. The shell type SNRs are divided into two sub-categories; the Shell type with shell-bright X-ray and the Mixed-Morphology (MM) type with center-filled X-ray (Rho & Petre 1998).

The Shell type SNRs are considered to be now in the free expansion phase or adiabatic phases. Figure 2.4 (a) shows a typical Shell type SNR, Tycho. The Shell type SNRs show a bright X-ray shell of thermal or non-thermal emission. Figure 2.4 (b) shows a typical Plerion type SNR, 3C 58. The Plerion type SNR have center-filled radio and X-ray emission from a neutron star or its wind nebula. Figure 2.4 (c) shows a typical Composite type SNR, G11.2-0.3. The Composite type SNR shows a spatial structure of the mixture of the Shell type and Plerion type.

The MM-SNRs exhibit different morphology in shell-bright radio and center-filled X-ray. Figure 2.4 (b) shows an X-ray image with radio contours of SNR W44. W44 is one of the famous MM-SNRs. 3C 391 and Kes 79 are also reported as MM-SNRs. Moreover, almost all

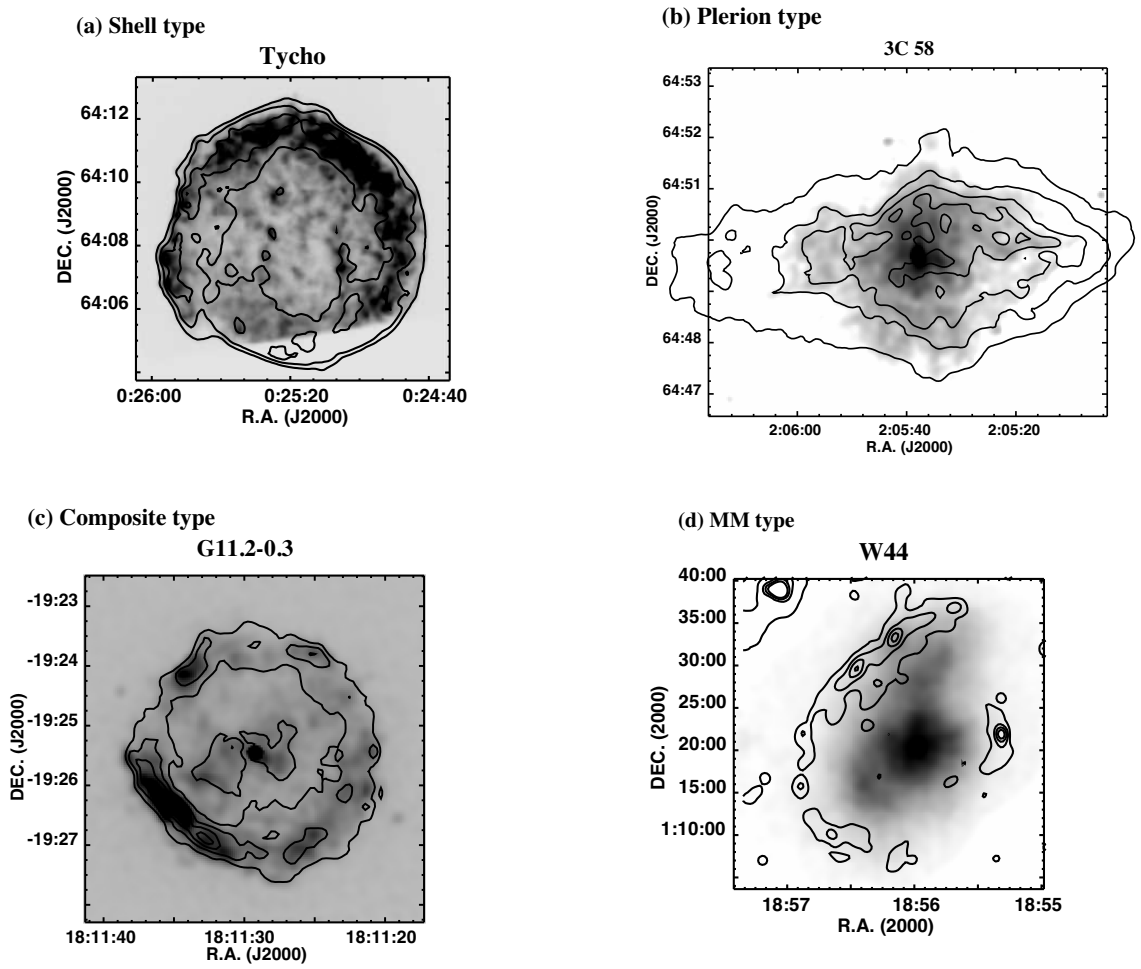

Figure 2.4: Classification examples of SNRs. Contours and grey scale indicate radio and X-ray emission, respectively (Credit: Chandra Supernova Remnant Catalog. http://hea-www.cfa.harvard.edu/ChandraSNR/). (a) Shell type SNR; Tycho SNR, Contour: 1.4 GHz by VLA, Gray scale: 0.3–10 keV by Chandra. (b) Plerion type SNR; SNR 3C 58, Contour: 1.4 GHz by VLA, Gray scale: 0.3–10 keV by Chandra. (c) Composite type SNR; SNR G11.2-0.3, Contour: 1.4 GHz by VLA, Gray scale: 0.3–10 keV by Chandra. (d) MM-SNR; SNR W44, Contour: 1.4 GHz by VLA, Gray scale: 0.7–10 keV by ASCA. These figures are taken from Kawasaki (ph.D.).

GeV-bright SNRs are MM-SNRs with the RP (e.g. W49B, Abdo et al. 2010, Ozawa et al. 2009). Two formation mechanisms are proposed to explain a formation of MM-SNRs (Rho & Petre 1998). A cloud evaporation model explains X-ray emission by evaporated many small interior clouds. On the other hand, a fossil conduction model (Cox et al 1999, Shelton et al. 1999a) predicts that the hot interior plasma gradually become uniform by thermal conduction and creates center-filled X-ray emission. In this fossil conduction model, an X-ray plasma at the shell is too cold to emit X-rays ($kT <\sim 0.1$ keV).

2.2.2 Standard Evolution of Supernova Remnants

SNRs generally evolve through three phases, "Free Expansion phase", "Adiabatic phase" and "Radiative Cooling phase" (Cioffi et al. 1988, Truelove & McKee 1999). These phases are basically determined by the balance of pressure between the mass of the supernova ejecta and swept-up ISM. Here, we assume an expansion inside a uniform ISM.

Free Expansion phase

During the "Free Expansion phase", the ejecta can expand with little deceleration by ISM. Assuming the energy of supernova ($E \sim 10^{51}$ erg) is mostly converted into kinetic energy, the velocity of ejecta becomes $v_f \sim \sqrt{2E/M}$:

$$v_f \sim 8.5 \times 10^3 \left(\frac{E}{10^{51}\ \mathrm{erg}}\right)^{1/2} \left(\frac{M}{1.4M_\odot}\right)^{-1/2} [\mathrm{km\ s^{-1}}]. \tag{2.1}$$

where M is the ejecta mass. When the mass of compressed ambient gas (M_{ISM}) becomes comparable to the ejecta mass, the pressure of the shocked ISM is not negligible. M_{ISM} can be expressed by

$$M_{ISM} = \frac{4}{3}\pi\ r^3 \mu n_0, \tag{2.2}$$

where r, μ and n_0 are radius of the SNR, mean atomic mass and number density of ISM. Assuming solar metallicity (H:He $\sim$ 10:1), μ is $1.4m_H$, where m_H is the mass of hydrogen. The lifetime t_f of this phase and the corresponding radius r_f of the SNR can be calculated as

$$t_f \sim 250 \left(\frac{E}{10^{51}\ \mathrm{erg}}\right)^{1/2} \left(\frac{M}{1.4M_\odot}\right)^{5/6} \left(\frac{n}{1\mathrm{cm^{-3}}}\right)^{-1/3} [\mathrm{yr}] \tag{2.3}$$

$$r_f \sim 1 \left(\frac{M}{1.4M_\odot}\right)^{1/3} \left(\frac{n}{1\mathrm{cm^{-3}}}\right)^{-1/3} [\mathrm{pc}]. \tag{2.4}$$

G1.9+0.3 ($t \sim 100$ yr), the youngest Galactic SNR, is believed to be in "Free Expansion phase" now (Reynolds et al. 2008).

Transition phase

In the transition phase from "Free Expansion phase" to "Adiabatic phase", ISM decelerates the shock wave (the forward shock) and forms the another shock wave, called as a reverse shock which propagates outward first then inward. Inside the SNR, shocked interstellar materials are separated from the ejecta by a contact discontinuity. The reverse shock which propagates away from the contact discontinuity compresses and heats the supernova ejecta. Figure 2.5 shows a schematic view of an SNR in this transition phase. As shown in Figure 2.6 (Gaetz et al. 2000), 1E 0102.2−7219, which is a young SNR in the Small Magellanic Cloud, is a typical SNR in this phase. It is clear that the X-ray emission (shown in blue) is mainly coming from the shock-heated ejecta, while the radio emission (shown in red) is produced by shock-accelerated electrons swept-up from the ISM.

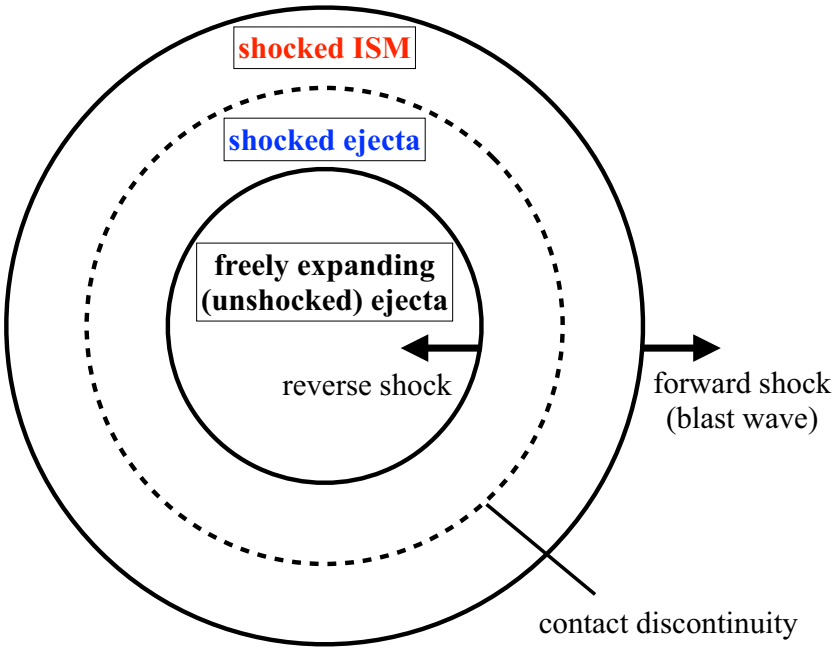

Figure 2.5: A schematic structure of an SNR in the transition phase.

Adiabatic phase

When the mass of the swept-up ISM becomes non-negligible ($M_{\rm ISM} >\sim 10 M_\odot$), the gas is cooled by adiabatic expansion. Since Sedov (1959) and Taylor (1950) obtained the self-similar solution of this stage independently, this "Adiabatic phase" is often called the "Sedov-Taylor phase". The equation of motion can be expressed as follows.

$$\frac{d}{dt}\left(\frac{4}{3}\pi r^3 \mu n_0 \dot{r}\right) = 4\pi r^2 P, \tag{2.5}$$

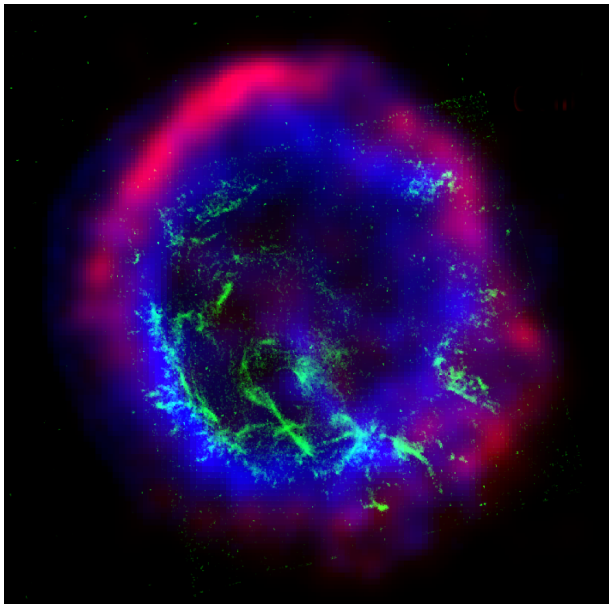

Figure 2.6: A composite image of SNR 1E 0102.2-7219 (Gaetz et al. 2000). The radio, optical and X-ray images are shown in red, green and blue, respectively. Image Credit: X-ray (NASA/CXC/SAO); optical (NASA/HST); radio (CSIRO/ATNF/ATCA).

where $P = E/2\pi r^3$ is the pressure assuming that the gas is mono-atomic and energy loss due to radiation is unimportant. We insert this into the equation and get

$$\frac{d}{dt}\left(r^3 \mu n_0 \dot{r}\right) = \frac{3}{2\pi}\frac{E}{r}. \tag{2.6}$$

Using $r \propto t^{2/5}$ from the dimensional analysis, we can solve equation and obtain the relations below,

$$r_S = 13\left(\frac{E}{10^{51}\ \mathrm{erg}}\right)^{1/5}\left(\frac{n}{1\ \mathrm{cm}^{-3}}\right)^{-1/5}\left(\frac{t}{10^4\ \mathrm{yr}}\right)^{2/5}\ [\mathrm{pc}] \tag{2.7}$$

$$v_S = 500\left(\frac{E}{10^{51}\ \mathrm{erg}}\right)^{1/5}\left(\frac{n}{1\ \mathrm{cm}^{-3}}\right)^{-1/5}\left(\frac{t}{10^4\ \mathrm{yr}}\right)^{-3/5}\ [\mathrm{km\ s}^{-1}]. \tag{2.8}$$

$$T_S = 3\times 10^6\left(\frac{E}{10^{51}\ \mathrm{erg}}\right)^{2/5}\left(\frac{n}{1\ \mathrm{cm}^{-3}}\right)^{-2/5}\left(\frac{t}{10^4\ \mathrm{yr}}\right)^{-6/5}\ [\mathrm{K}]. \tag{2.9}$$

This Sedov-Taylor phase continues for a few tens of thousand years. Until the end of this "Adiabatic phase", about 70 % of the supernova explosion energy is transformed into thermal energy (Chevalier 1974). This expression represents the cooling with time in "Adiabatic phase".

Radiative Cooling phase

The cooling rate has increased along with the temperature drop until around 10^5 K (see Figure 2.7) that means the heavy elements efficiently capture electrons and lose their energies

through recombination radiation. When the temperature drop to $\sim 10^6$ K, SNRs can evolve no longer adiabatically and enter the "Radiative Cooling phase". While the radiative energy loss is efficient, the adiabatic expansion continues because the interior is still hot. This is called "pressure-driven snow plough phase" ($r \propto t^{2/7}$; McKee & Ostriker 1977). When the internal pressure becomes negligible as the temperature drops further, the shell expands with a time dependency of $r \propto t^{1/4}$; this is the so-called "momentum-conserving snowplow phase" (Cioffi et al. 1988). Finally, the boundary of the SNR disappears and the remnant merges with the ISM as the shock velocity decelerates to that of the typical proper motion of the ISM ($\sim$10 km s^{-1}).

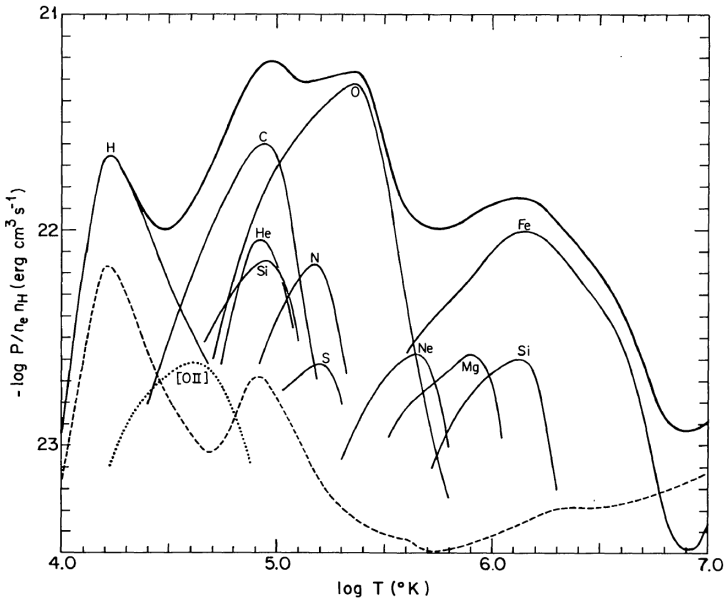

Figure 2.7: Cooling coefficient for an thin thermal plasma as a function of plasma temperature. The individual contributions from major elements are also shown.This figure is taken from Gaetz & Salpeter (1983).

2.2.3 Thermal Radiation Processes

It is well known that thermal X-ray emission from SNRs consists of both optically thin thermal bremsstrahlung and line emission from heavy ions. Here, we summarize the basic theory of the two emission processes.

Bremsstrahlung

In a plasma, electrons scattered by ions emit radiation called bremsstrahlung (free-free emission). The power of bremsstrahlung per unit volume, angular frequency and time is given

by

$$\frac{dE}{dVd\omega dt} = \frac{16e^6Z^2}{3m^2c^3}n_e n_i \frac{1}{v} g(v,\omega), \tag{2.10}$$

where Z, m, v, n_e, n_i, e and c are atomic number, mass and velocity of an electron, number density of electrons and atoms, the charge unit and speed of light. g is known as a Gaunt factor (Karzas and Latter 1961). Assuming a plasma in thermal equilibrium, the velocities of electrons obey the Maxwellian distribution. If we ignore the weak dependence of g on v, we can derive the average value $< 1/v >$ as

$$\left\langle \frac{1}{v} \right\rangle = \left(\frac{m}{2\pi kT}\right)^{3/2} \int_{\hbar\omega}^{\infty} \left(\frac{1}{v}\right) 4\pi v^2 \exp\left(-\frac{mv^2}{2kT}\right) dv \tag{2.11}$$

$$= \sqrt{\frac{2m}{\pi kT}} \exp\left(-\frac{\hbar\omega}{kT}\right), \tag{2.12}$$

where k, $\hbar$ and T is the Boltzmann constant, reduced Planck constant and the electron temperature. Using equation. 2.10 and 2.12, we can obtain the emissivity of the optically-thin thermal bremsstrahlung as,

$$\frac{dE}{dVd\omega dt} = \frac{16e^6Z^2}{3m^2c^3}n_e n_i \sqrt{\frac{2m}{\pi kT}} \exp\left(-\frac{\hbar\omega}{kT}\right) \overline{g}(T,\omega), \tag{2.13}$$

where $\overline{g}(T,\omega)$ is the velocity-averaged Gaunt factor. We then integrate equation 2.13 over all frequencies:

$$\frac{dE}{dVdt} = 4\pi \frac{16e^6Z^2}{3m^2c^3\hbar}n_e n_i \sqrt{\frac{2mkT}{\pi}} \overline{g}(T) \tag{2.14}$$

$$\sim 1.4 \times 10^{-27} n_e n_i T^{1/2} \overline{g}(T) \text{ erg cm}^{-3} \text{ s}^{-1}. \tag{2.15}$$

The frequency-integrated Gaunt factor $\overline{g}(T)$ is ~ 1.3 ($T = 3 \times 10^6$[K]; Itoh et al. 2002). Equation 2.15 shows that the emissivity of a thermal plasma increases with both the density and temperature. Hence, if an X-ray observation determines the spectral shape and flux of the thermal continuum emission, we can obtain these parameters of the thermal equilibrium plasma.

Line emission

The line (bound-bound) emission is originated from the transition between two discrete quantum levels of a bound electron. For hydrogen-like ions (of the atomic number Z) having only one bounded electron, we can roughly derive the transition energy ($E_{\rm bb}$) from quantum theory by using the principle quantum numbers n and n',

$$E_{\rm bb} \sim Z^2 R_y \left(\frac{1}{n^2} - \frac{1}{n'^2}\right), \tag{2.16}$$

where R_y is Rydberg constant (=13.6 eV). The H-like transitions are called as Lyman series, and Lyα, Lyβ, and Lyγ are transitions of $1s$–$2p$, $1s$–$3p$, and $1s$–$4p$, respectively. For example, Lyman" series emission of Fe Lyα ($1s$–$2p$), Lyβ ($1s$–$3p$) and Lyγ ($1s$–$4p$) are 6.966, 8.266 and 8.732 keV, respectively.

On the other hand, when elements have two or more electrons, the transition processes are more complicated. He-like ions, for example, emit three strong emission lines: resonance, forbidden, and inter-combination transition lines. In the case of He-like Fe which have two electrons, the line energy of the transition are 6.702 keV (Kα resonance; $1s^2\,{}^1S_0$–$1s2p\,{}^1P_1$), 6.641 keV (Kα forbidden; $1s^2\,{}^1S_0$–$1s2s\,{}^3S_1$), 6.670 keV (Kα inter-combination; $1s^2\,{}^1S_0$–$1s2p\,{}^3S_{2,1}$), 7.798 keV (Kβ; $1s^2$–$1s3p$), 8.217 keV (Kγ; $1s^2$–$1s4p$) and so on. The typical thermal X-ray emission spectrum from a young SNR is shown in figure. 2.8 (Decourchelle et al. 2001).

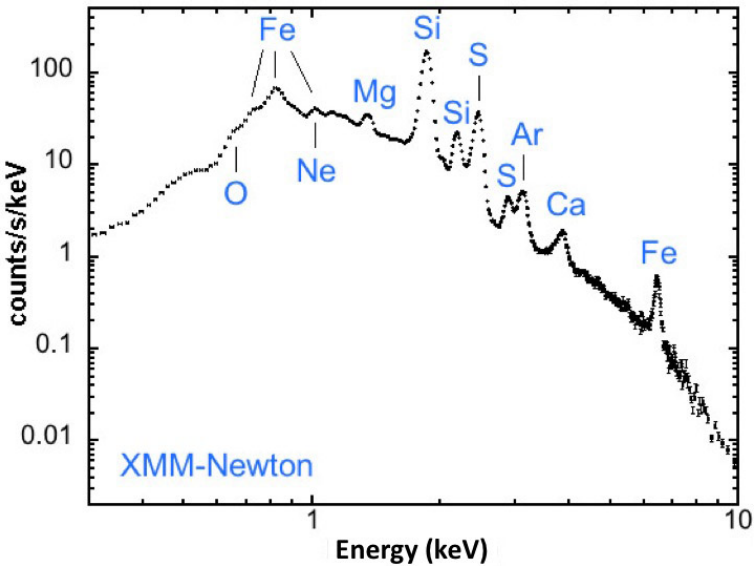

Figure 2.8: X-ray spectrum of the Tycho SNR as the type of Ia SNR obtained with XMM-Newton observatory (Decourchelle 2010).

We can determine the relative abundances of chemical elements in the shocked ejecta of SNRs from the line emission. In an ionized and optically thin thermal plasma which is collisionally excited by free electrons, the line intensity is proportional to $n_e n_i$ which describe the probability of collisions between electrons and ions. If we can obtain the relative abundances of chemical elements in the SNR ejecta, we can constrain the progenitor type by comparing with explosive nucleosynthesis models of SNe.

Recombining Plasma

A standard picture of thermal plasmas associated with supernova remnants (SNRs) is that the state of the gas appears to be either an ionizing plasma (IP) for young or intermediate aged SNRs (e.g., Kepler's SNR, Kinugasa & Tsunemi 1999), or plasma in collisional ionization equilibrium (CIE) for old SNRs (e.g., 30DorC, Yamaguchi et al. 2009a). Recent X-ray observations have revealed several SNRs that are in the recombination-dominated phase (e.g. Yamaguchi et al. 2009). These recombining plasmas (RPs) have ionization temperatures ($T_{\rm Z}$) that are higher than the electron temperature ($T_{\rm e} < T_{\rm Z}$).

The most important prove of RPs is radiation recombination continuum (RRC). RRC has the hump-like emission structure through the free-bound transitions as the recombination process due to the over-ionization (Smith & Brickhouse 2002). If the electron temperature is lower than the K-edge energy ($I >> kT_{\rm e}$), flux of RRC is approximated as

$$F(E) \propto \exp\left(-\frac{E-I}{kT_{\rm e}}\right), {\rm for} E \geq I, \tag{2.17}$$

where E is energy of X-ray photons. For example, over-ionized H-like Si shows RRC as hump-like emission with the edge around $I \sim 2.666$ keV which is the K-shell binding potential.

2.3 Cosmic rays

Cosmic rays (CRs) were first discovered in 1912 by HESS (HESS 1912), and it is well known that highest energy of CRs reaches up to 10^{20} eV. However, the origin and acceleration mechanism are still unknown and remain one of the biggest problems in the field of astrophysics.

The energy density of CRs (> 1 GeV) is about 1 eV cm^{-3} in our Galaxy. Assuming the total volume of our Galaxy, the estimated injection rate of CRs is $\sim 10^{40}$ erg s^{-1}. Using the supernova rate in spiral galaxies (1/30 yr^{-1}) and the energy of the supernova explosion ($\sim 10^{51}$ erg), we would agree with the energetics of CRs if 1–10% of the total energy converts into the CR acceleration. The efficiency of the CR acceleration in SNRs is still uncertain.

As shown in Figure 2.9, the CR spectrum up to $10^{15.5}$ eV is represented by a single power-law shape. Since the gyro radius of the CRs up to this energy is smaller than the size of the Galactic bulge, it is thought that they are produced within Our Galaxy. Since the first discovery of synchrotron X-rays from SN 1006 by Koyama et al. (1995), numerous SNRs are found to emit synchrotron X-rays (e.g., RX J1713.7−3946; Tanaka et al. 2008). These findings support the idea that Galactic CRs are accelerated by SNRs. Given this situation, here we describe the basic theory of diffusive shock acceleration and X-ray emission spectrum emitted by these accelerated electrons.

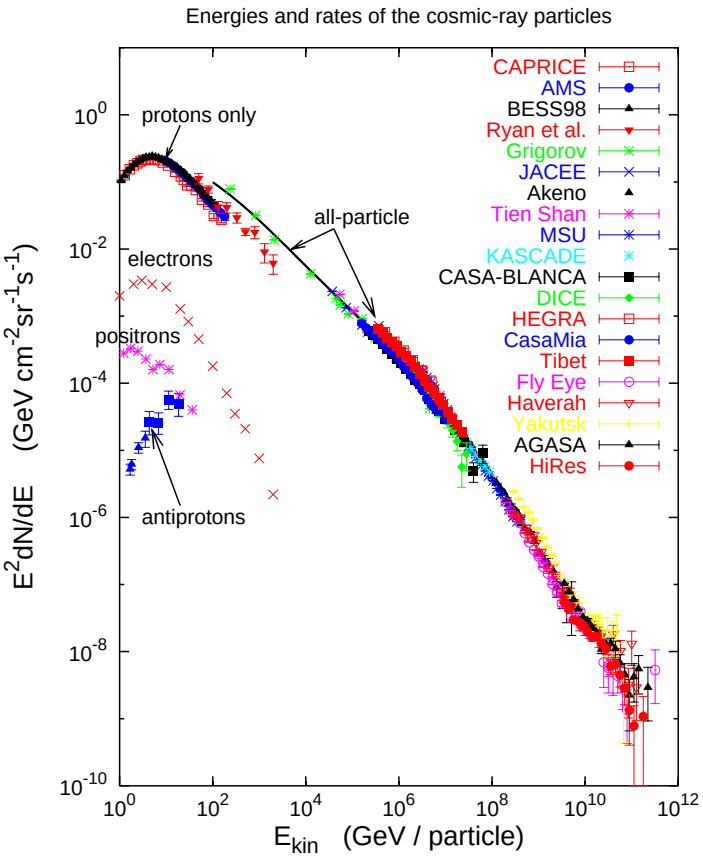

Figure 2.9: Cosmic-ray flux observed by various observatory (Hillas 2006).

2.3.1 Shock Wave

In the evolution of SNRs, supersonic flow causes the production of shock waves which compress and heat the gas. We consider a coordinate system in which the shock front is stationary. Figure 2.10 shows a schematic picture around the shock wave. We can describe conservation of mass, momentum and energy flux between upstream and downstream as follows (so-called Rankine-Hugoniot Equations):

$$\rho_1 v_1 = \rho_2 v_2 \tag{2.18}$$

$$\rho_1 v_1^2 + P_1 = \rho_2 v_2^2 + P_2 \tag{2.19}$$

$$\left\{\rho_1(u_1 + \frac{1}{2}v_1^2) + P_1\right\} v_1 = \left\{\rho_2(u_2 + \frac{1}{2}v_2^2) + P_2\right\} v_2, \tag{2.20}$$

where v_i, ρ_i and P_i are the velocity, density and pressure of upstream (subscript 1) and downstream (subscript 2), respectively. u is the internal energy per unit mass. Using the ratio of specific heat $\gamma(= C_p/C_v)$ and the Mach number $M_i = v_i/c_s$ where $c_s(= \sqrt{\gamma P_i/\rho_i})$ is the sound velocity, we can obtain

$$r \equiv \frac{\rho_2}{\rho_1} = \frac{v_1}{v_2} = \frac{(\gamma+1)M_1^2}{2+(\gamma-1)M_1^2} \tag{2.21}$$

$$\frac{P_2}{P_1} = \frac{2\gamma M_1^2 - (\gamma-1)}{\gamma+1}. \tag{2.22}$$

Assuming a strong shock ($p_2/p_1 \gg 1$ or $M_1 \gg 1$) as is usually the case for young SNRs, we can obtain the compression ratio r:

$$r = \frac{\gamma+1}{\gamma-1}. \tag{2.23}$$

For a non-relativistic monoatomic gas ($\gamma = 5/3$), the compression ratio r and M_2 becomes 4 and $1/\sqrt{5}$, respectively.

Using the relations above, we can go ahead to discuss shock heating of the swept-up gas.

Assuming the strong shock ($P_2/P_1 \gg 1$), the relation of temperature between upstream (T_1) and downstream (T_2), the upstream and downstream are defined in the shock rest frame, can be obtained as follows:

$$\frac{T_1}{T_2} = \frac{P_1}{P_2}\frac{\gamma-1}{\gamma+1}. \tag{2.24}$$

Since v_1 is equal to v_s, the temperature of the downstream gas kT_2 is obtained as

$$kT_2 = \frac{2(\gamma-1)\mu m_{\rm H} v_s^2}{(\gamma+1)^2}, \tag{2.25}$$

where k, μ, and $m_{\rm H}$ are the Boltzmann constant, the mean atomic weight and the hydrogen mass. Using $\gamma = 5/3$, we can calculate the post-shock temperature:

$$kT_2 = \frac{3}{16}\mu m_{\rm H} v_s^2. \tag{2.26}$$

Thus, the shock converts the bulk kinetic energy into the thermal energy of the post-shock gas.

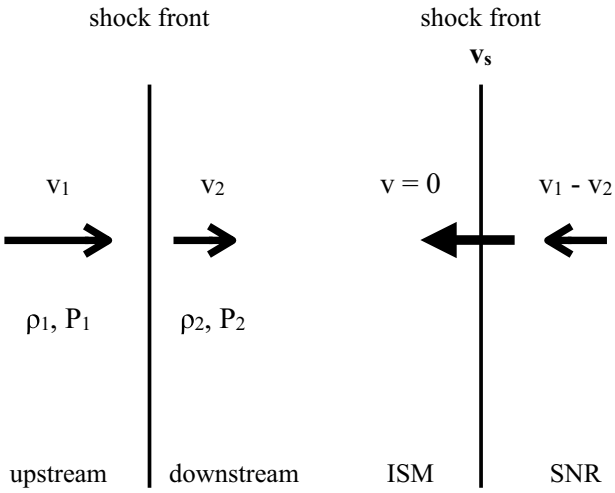

Figure 2.10: A schematic picture of the shock front and gas flow in the shock rest frame (left) and observer rest frame (right).

Thermal Non-Equilibrium

The plasma in a young SNR is usually far from the electron-ion equilibrium because the shock is propagating into a medium of an extremely low density (~ 1 cm^{-3}). Using Equation 2.26, the ion temperature in the downstream is

$$kT_{\rm i} = \frac{3}{16} m_{\rm i} v_s^2, \tag{2.27}$$

where $kT_{\rm i}$ and $m_{\rm i}$ are the temperature and mass of an atom, respectively. In a completely collisionless plasma, the temperature of Hydrogen, for example, is $m_{\rm H}/m_e \sim 1800$ times higher than that of the electrons. In a realistic case, Coulomb collisions occur between the shocked electrons and ions, and the temperature gradient can be described as

$$\frac{{\rm d}\Delta T}{{\rm d}n_{\rm e}t} \sim 0.13 \frac{Z^2}{A} \frac{\Delta T}{T_e^{3/2}}, \tag{2.28}$$

where A is atomic mass, and $\Delta T = T_{\rm i} - T_{\rm e}$ (e.g. Spitzer 1962). By integrating Equation 2.28, we can obtain

$$T_{\rm e} \sim \left(0.33 \frac{Z^2}{A} \frac{T_i n_{\rm e} t}{Z+1} \right)^{\frac{5}{2}}. \tag{2.29}$$

If we consider the Hydrogen dominant plasma, we can roughly estimate to

$$kT_{\rm H} \sim 2.4 \times 10^{11} \left(\frac{n_{\rm e} t}{1 \text{ cm}^{-3} \text{ s}} \right)^{-1} \left(\frac{kT_{\rm e}}{1\ keV} \right) [\text{keV}]. \tag{2.30}$$

Therefore, if the density $n_{\rm e}$ is $\sim$1 cm^{-3}, the time when the plasma reaches electron-ion equilibrium is about 10^{11} s ($\sim$ 3000 yr).

The shocked ejecta which is initially neutral are gradually losing their bound electrons through collisions with thermal free electrons. The typical timescale when plasma reaches collisional ionization equilibrium (CIE) can be calculated as $n_{\rm e}t \sim 10^{12}$ cm^{-3} s (Masai 1993). This "ionization parameter" $n_{\rm e}t$ is the key parameter which describes the ionization state of the plasma. Since the ages of most SNRs previously observed are less than $t \sim 10^{12}$ s, the plasma now is not in CIE but in a non-equilibrium ionization (NEI) state.

Following Equation 2.27, the temperature of electrons ($T_{\rm e}$) is much lower than that of heavier ions ($T_{\rm ion}$) behind the shock ($\propto m_{\rm i}$). They slowly reach equilibrium to a common temperature through Coulomb collisions. However, a number of theoretical models suggest that the collisionless shock in astrophysical environment rapidly heats up electron temperature at the shock front ($T_{\rm e}/T_{\rm ion} \sim 1$; e.g. Ghavamian et al. 2007). The recent observation has revealed that the rapid electron heating really occurs by the collisionless shock of the SNR (Tycho SNR; Yamaguchi et al. 2013).

2.3.2 Diffusive Shock Acceleration

It is now well accepted that CRs are accelerated by diffusive shock acceleration (DSA; Blandford & Eichler 1987; Bell 1978). DSA can efficiently accelerate CRs to relativistic energies and achieve a power-law energy distribution with an index of $\sim$2, which is almost consistent with the observed power-law index of CRs ($\sim$ 2.7; Cronin 1999). Note here that the difference between 2.0 and 2.7 is considered to be due to the escape of the CRs (e.g. Putze et al. 2009, Ohira et al. 2010). Here, we briefly summarize the DSA theory.

DSA applies to strong shock waves of SNRs propagating through plasmas in which physical condition is briefly discussed in Section 2.3.1. A schematic diagram is shown in Figure 2.11. The fluid velocities in the upstream and downstream of the shock is v_1 and v_2 ($v_2 < v_1$), respectively. We assume a plane-parallel, non-relativistic shock in steady state and use the test-particle approximation in which any reaction between the accelerating particles and the background fluid is ignored. A particle is elastically scattered by magnetic turbulence in downstream and changes the energy from E to E':

$$\begin{aligned} E' &= \gamma_2 \left[\gamma_2 (E - v_2 p_x) + v_2 \gamma_2 \{-(p_x - v_2 E)\}\right] \\ &\sim E - 2\beta_2 p_x, \end{aligned} \tag{2.31}$$

where $\beta_2 = v_2/c \ll 1$, $\gamma_2 = 1/\sqrt{1-\beta_2^2} \sim 1$ and $p_x (= E/c\ \cos\theta)$ is momentum of the particle perpendicular to the shock with an angle of θ. The particle crosses the shock front and is

scattered by upstream. Then the particle gains energy from E' to E'':

$$\begin{aligned} E'' &\sim (1 - 2\beta_2 \cos\theta)(1 + 2\beta_1 \cos\theta)E \\ &\sim \{1 + 2(\beta_1 - \beta_2)\cos\theta\}E. \end{aligned} \tag{2.32}$$

In one round trip across the shock, the particle gains the energy $\Delta E \sim 2E(\beta_1 - \beta_2)\cos\theta$. We calculate the average energy gain as

$$\left\langle \frac{\Delta E}{E} \right\rangle = 2\int_0^{\pi/2} \frac{\Delta E}{E}(2\sin\theta\cos\theta d\theta) = \frac{4}{3}(\beta_1 - \beta_2) \tag{2.33}$$

The mean energy after n-times round trips can be calculated below:

$$\begin{aligned} E_n &= E_0 \left\{1 + \frac{4}{3}(\beta_1 - \beta_2)\right\}^n \\ &\sim E_0 \exp\left\{\frac{4}{3}(\beta_1 - \beta_2)n\right\}, \end{aligned} \tag{2.34}$$

where E_0 is an initial energy of one particle.

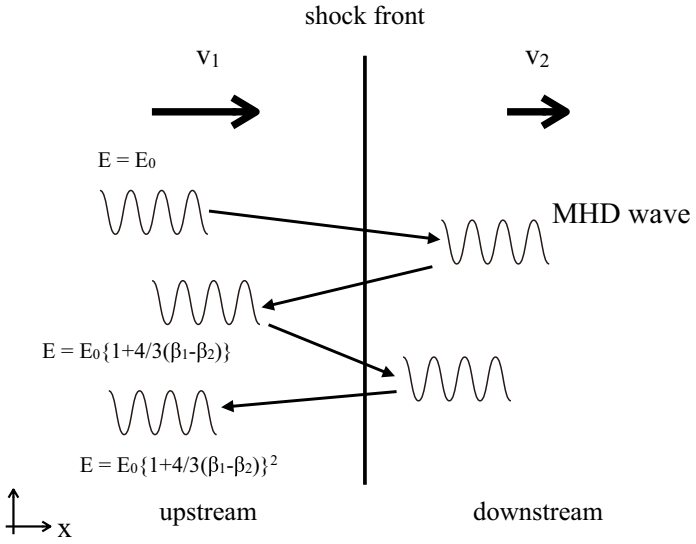

Figure 2.11: A schematic drawing of the scattering of a charged particle in DSA.

In order to determine the energy distribution of accelerated particles, we have to consider the probability of escaping from downstream. The flux of particle across the shock becomes

$$\frac{nc}{2}\int_0^{\pi/2} \cos\theta \sin\theta d\theta \sim \frac{nc}{4}, \tag{2.35}$$

where n is a number density of charged particles. nv_2 is the flux of escaping particles along the convective motion of the fluid in downstream. The probability of escape is $(nv_2)/(nc/4) = 4\beta_2$

per one round trip. We can calculate the probability P_n that charged particles reach E_n and escape from the system as

$$\begin{aligned} P_n &= 4\beta_2 (1 - 4\beta_2)^n \\ &\sim 4\beta_2 \exp(-4\beta_2 n). \end{aligned} \tag{2.36}$$

Using equation and , we obtain below:

$$P_n \propto E_n^{-\alpha}, \tag{2.37}$$

where $\alpha = 3\beta_2/(\beta_1 - \beta_2)$. Then, we can derive the differential energy distribution of accelerated particles as

$$\frac{dN(E)}{dE} \propto P_n \frac{dn}{dE} \propto E^{-\alpha-1}. \tag{2.38}$$

The index of $(-\alpha - 1)$ is $-(v_1/v_2 + 2)/(v_1/v_2 - 1) = -(\gamma + 2)/(\gamma - 1)$. Using equation ($\gamma = 5/3$ for strong shock), the spectral index of the accelerated particles becomes $\sim$2. This result agrees with the Galactic CR spectrum and the observed radio index in SNRs.

2.3.3 Non-thermal Radiation Process of Electrons

The X-ray emission from SNRs often shows a feature-less X-ray continuum as shown in Figure 2.12 (RX J1713.7-3946; Tanaka et al. 2008). This is reasonably understood as synchrotron emission by CR-electrons. Here a basic theory of synchrotron radiation as well as the photon spectrum by electrons of power-law distribution are explained.

Charged particles propagating in magnetic fields emit synchrotron radiation. Synchrotron emission is the dominant radiation-loss process of relativistic electrons. The emission power of synchrotron per angular frequency by a single electron in a magnetic field B is given as:

$$\frac{dP}{d\omega} = \frac{\sqrt{3}e^3}{2\pi mc^2} B \sin\alpha \; F\left(\frac{\omega}{\omega_c}\right) \tag{2.39}$$

where α and $\omega_c = (3\gamma^2 e/2mc)B\sin\alpha$ are the pitch angle between the electron and the magnetic field and the peak frequency, respectively. F is the function of ω/ω_c:

$$F\left(\frac{\omega}{\omega_c}\right) = \frac{\omega}{\omega_c} \int_{\omega/\omega_c}^{\infty} K_{5/3}(z) dz, \tag{2.40}$$

where $K_{5/3}$ is Bessel function of order 5/3. Integrating over all frequencies, we can obtain the total emission power:

$$P_{sync} = \frac{4}{3} \sigma_T c \beta^2 \gamma^2 U_B, \tag{2.41}$$

where σ_T and $U_B (= B^2/8\pi)$ are Thomson cross section and the magnetic field energy density, respectively.

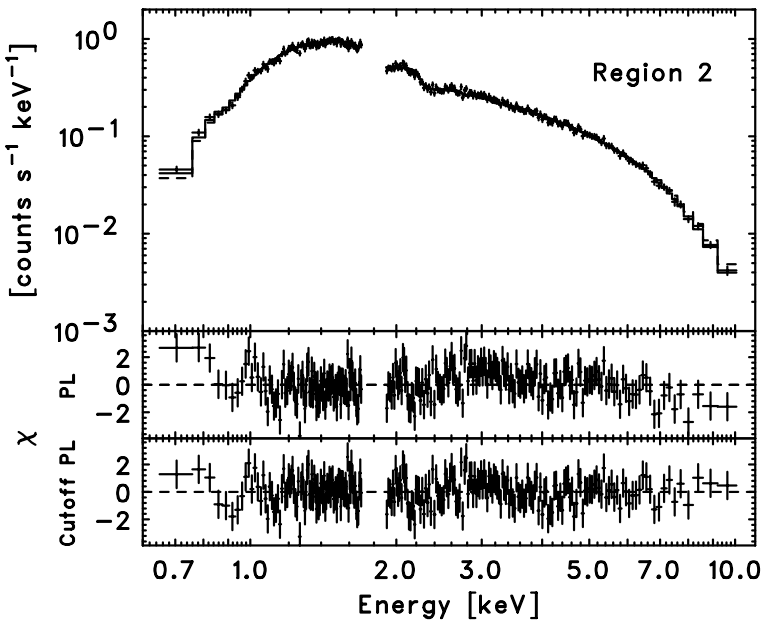

Figure 2.12: X-ray spectrum of SNR RX J1713.7-3946 observed with Suzaku observatory. The lower panels show the residual fitted with two different models.

We can calculate the synchrotron radiation from electrons with a power-law energy distribution whose spectral index is p ($N(E) = CE^{-p}$). The total power per unit volume by integrating over all energies is

$$P_{tot}(\omega) = C \int P(\omega) E^{-p} dE \propto \int F\left(\frac{\omega}{E^2}\right) E^{-p} dE. \tag{2.42}$$

Using $\omega_c \propto E^2$, this relation can be written by $x = \omega/E^2$:

$$P_{tot}(\omega) \propto \int F(x) \left(\frac{\omega}{x}\right)^{-p/2} \frac{(\omega/x)^{3/2}}{\omega} dx \tag{2.43}$$

$$\propto E_\gamma^{-(p-1)/2} \tag{2.44}$$

where E_γ is photon energy. In the case of DSA ($p \sim 2$), the spectral index of photons becomes $(p-1)/2 \sim 0.5$. While P represents the energy flux (erg cm^{-2} s^{-1}), the photon flux (photons cm^{-2} s^{-1}) is useful in the X-ray band. Therefore, the photon flux can be expressed as $E^{-\Gamma}$ where $\Gamma(= (p+1)/2)$ is the photon index (~ 1.5 from DSA a strong shocks).

2.4 Fe Kα emission induced by Cosmic-rays

The important radiation process of this dissertation is irradiation of Kα lines through the interaction between molecular clouds and low energy CRs. The most probable emission to be obsererved is the neutral iron (Fe I) Kα line ($\sim$6.4 keV) because of its fluorescence yield.

The photon flux of Fe I Kα line induced by low energy CRs can be written as follows (e.g. Yusef-Zadeh 2007; Ballantyne & Fabian 2003):

$$F_{6.4\mathrm{keV}} = nz\omega\beta\frac{1}{4\pi D^2}\int_0^\infty N(p)\sigma(K(p))v(p)\ \mathrm{d}p, \tag{2.45}$$

where n, z, ω and β are the number density of the molecular cloud, the iron abundance, Fe K fluorescence yield and branching ratio to Kα ($\omega\beta \sim 0.28$), respectively. D is distance to an SNR, $N(p)$ is the momentum distribution of CRs, and v is the velocity of CRs. The cross section of protons obtained by the experiment can be written as a polynomial (Romo-Kröger 1998),

$$\sigma(K(p)) = I_{\mathrm{keV}}^{-2}\ \exp(0.006x^5 + 0.0285x^4 + 0.0091x^3 - 0.5981x^2 + 0.6564x + 11.122)\ 10^{-24}\ \mathrm{cm}^2, \tag{2.46}$$

where I_{keV} is the binding energy of the K-shell electron and $x = \ln(K(p)/I_{\mathrm{keV}})$. On the other hand, the cross section for electrons is phenomenologically evaluated below (Quarles 1976):

$$\sigma(E_\mathrm{e}) \sim 1.16 \times R(E_\mathrm{e})\ (E_\mathrm{e}/1\ \mathrm{keV})^{-1}\ \ln(E_\mathrm{e}/I)\ 10^{-20}\ \mathrm{cm}^2, \tag{2.47}$$

where $R(E_\mathrm{e})$ is the relativistic factor (Gryzinski 1965). Figure 2.13 shows the cross sections of Fe Kα excitation by both of protons and electrons.

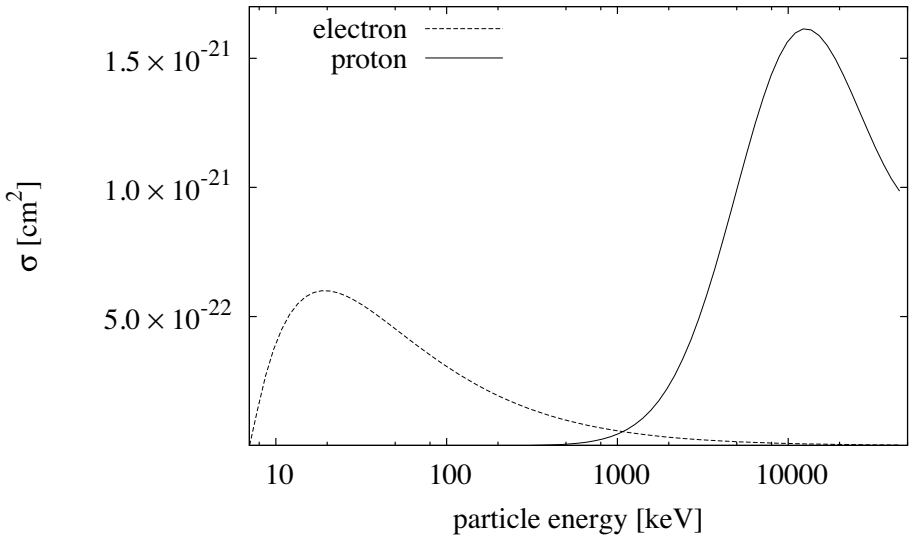

Figure 2.13: The cross sections of the Fe Kα excitation by proton (solid line) and electron (dashed line).

2.4.1 Non-thermal Bremsstrahlung

CRs interacting with molecular clouds also emit Bremsstrahlung. We can calculate this "non-thermal" Bremsstrahlung emission of powerlaw distribution of particle (index s) using number

distribution of $N(p) = Ap^{-s}$. We can calculate non-thermal Bremsstrahlung flux ($F_{br}(E_\gamma)$):

$$F_{br}(E_\gamma) = n \int \frac{\mathrm{d}\sigma_{br}(p, E_\gamma)}{\mathrm{d}E_\gamma}\ v(p)\ Ap^{-s}\ \mathrm{d}p, \tag{2.48}$$

where p, E_γ are the momentum of CRs and the energy of Bremsstrahlung photons, respectively. $\mathrm{d}\sigma_{br}(p, E_\gamma)/\mathrm{d}E_\gamma$ is the cross section of Bremsstrahlung and we use the non-relativistic approximation formula below:

$$\frac{\mathrm{d}\sigma_{br}(p, E_\gamma)}{\mathrm{d}E_\gamma} = \frac{8}{3}\mu\alpha r_0^2 \frac{m_\mathrm{e}c^2}{E_\gamma E'} \ln \frac{\left(\sqrt{E'} + \sqrt{E' - E_\gamma}\right)^2}{E_\gamma}, \tag{2.49}$$

where α is the fine structure constant, r_0 is the classical electron radius, m_e is mass of electron, c is speed of light and μ is ~ 1.4. E' is $E(p)$ or $(m_\mathrm{e}/m_\mathrm{p})E(p)$ in the case of CR electrons or protons, respectively. We can assume $E(p)$ as $p^2/2m$ for low energy CRs (non-relativistic). In Figure 2.14, we plot the relation between particle index and photon index according to Equation 2.48.

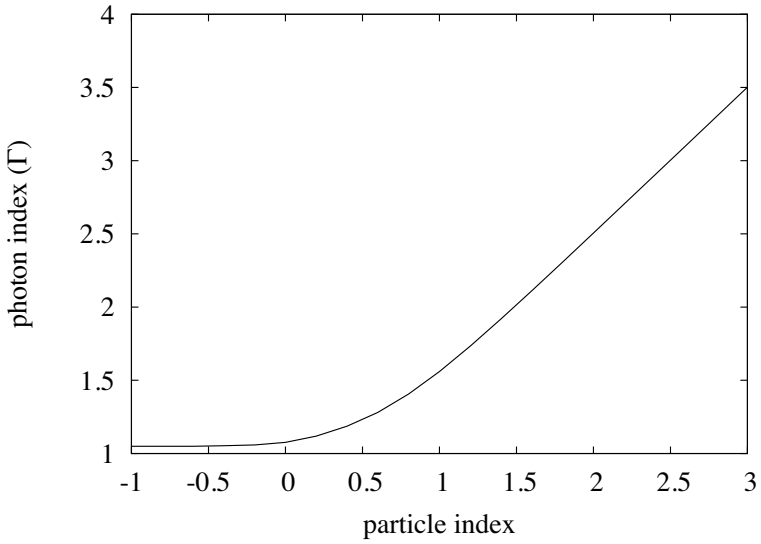

Figure 2.14: The relation between particle index and photon index on non-thermal Bremsstrahlung emission .

The ratio of the Fe Kα emission (6.4 keV) to Bremsstrahlung around 6.4 keV shows another behavior between electron and proton. The ratio called the equivalent width is defined as $EW_{6.4\ \mathrm{keV}} = F_{6.4\ \mathrm{keV}}/F_{br}(6.4\ keV)$. The equivalent width $EW_{6.4}$ does not depend on n:

$$EW_{6.4\ \mathrm{keV}} = \frac{F_{6.4\ \mathrm{keV}}}{F_{br}(E_\gamma = 6.4\ \mathrm{keV})} = \frac{z\omega\beta \int_I^\infty (\mathrm{d}N/\mathrm{d}E)\ \sigma(E_\mathrm{e})\ v(E_\mathrm{e})\ \mathrm{d}E_e}{\int (\mathrm{d}N/\mathrm{d}E)(\mathrm{d}\sigma_{br}(E_\mathrm{e}, E_\gamma)/\mathrm{d}E_\gamma)\ v(E_\mathrm{e})\ \mathrm{d}E_\mathrm{e}}. \tag{2.50}$$

Figure. 2.15 shows the equivalent width of electron and proton. We can determine the particle origin and its index by measuring the equivalent width of Fe Kα emission.

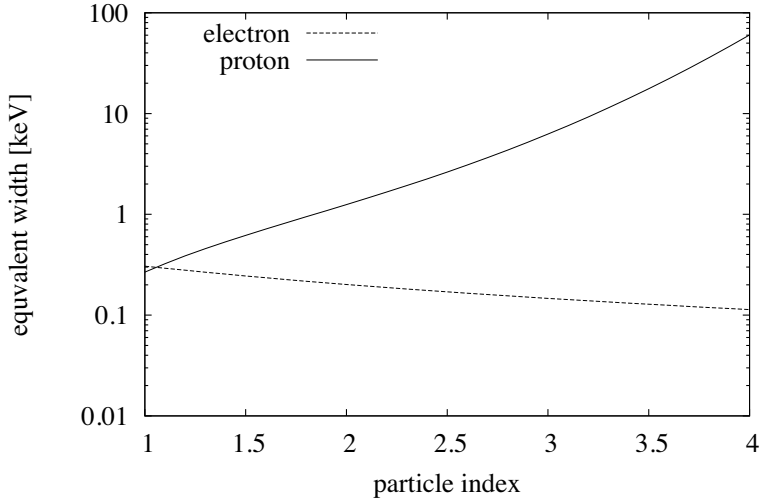

Figure 2.15: The equivalent width of 6.4 keV to Bremsstrahlung.

Chapter 3

Instruments

3.1 Suzaku

Suzaku is the 5th Japanese X-ray space observatory developed by Japanese-US collaboration with JAXA, NASA and many other institutions (Mitsuda et al. 2007). It was launched on 10 July, 2005 from Uchinoura Space Center into a near-circular orbit at an altitude of $\simeq$ 568 km (a low Earth orbit) and an inclination of 31 degrees. The orbital period of Suzaku is about 96 minutes. After the extensible optical bench (EOB) was successfully extended in orbit, a spacecraft length of Suzaku became 6.5 m. A schematic view of Suzaku is shown in Figure 3.1.

Three types of scientific instruments are onboard Suzaku: X-ray Imaging Spectrometer (XIS; Koyama et al. 2007), Hard X-ray Detector (HXD; Takahashi et al. 2007, Kokubun et al. 2007) and X-ray micro-calorimeter (XRS). While the XIS and XRS are located in the focal plane of the X-ray telescopes (XRTs; Serlemitsos et al. 2007), the HXD is a non-imaging and collimated sensor instrument. Unfortunately, the XRS is not operational due to liquid helium loss just after the launch. Figure 3.2 shows the configuration of these instruments on Suzaku. The capabilities of the instruments are listed in Table 3.1 adopted from Suzaku Technical Description[1].

3.1.1 XRT

The XRTs are the Walter-I grazing-incidence reflective optics consisting of tightly nested, thin-foil conical mirror shells. X-rays are reflected twice by a parabolic and hyperbolic surface, and focused on the detectors (see Figure 3.3[2]). The XRTs are equipped with the pre-collimators to

[1] https://heasarc.gsfc.nasa.gov/docs/suzaku/prop_tools/suzaku_td/

[2] http://www.u.phys.nagoya-u.ac.jp/uxge/r_e/r_e2.html

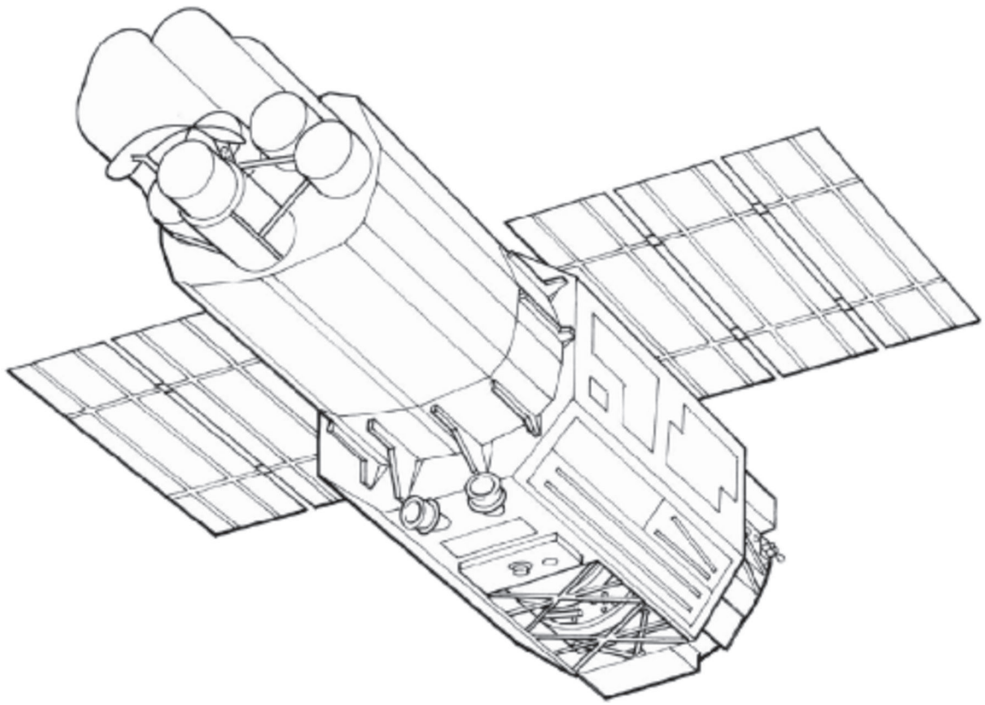

Figure 3.1: A schematic view of Suzaku in orbit (Mitsuda et al. 2007).

reduce the stray light and the contamination of the cosmic X-ray background (CXB). There are two types of the XRTs; XRT-S for the XRS and 4 XRT-I for the XISs.

In the energy range of 0.2–1.2 keV, the XRTs demonstrate a large aperture efficiency with a moderate imaging capability. Figure 3.4 shows the on-axis effective area of the XRTs including the detector efficiency, compared with those of other X-ray satellites. The effective area of Suzaku (XRT/XIS) is larger than that of Chandra and comparable to that of XMM-Newton above $\sim$6 keV. The focal length of XRT-I is 4.75 m and the half power diameter (HPD), which is the diameter within which 50% of the focused X-ray is enclosed, is $\simeq 2'.0$. Since the angular resolution of the XRT is low, the image of a point-like source becomes more diffuse than the other X-ray satellites (Figure 3.5 left). This point spread function (PSF) and the encircled energy fraction (EEF) which shows the fractional energy within a given radius are also shown in Figure 3.5.

3.1.2 XIS

The main instrument of the Suzaku X-ray observatory is the XIS, X-ray silicon charge coupled devices (CCD) camera (Koyama et al. 2007). The XIS consists of four CCDs; XIS 0, 2 and 3 are front-illuminated (FI) CCDs and XIS 1 is a back-illuminated (BI) CCD. However, the XIS 2 camera has been out of operation since November 2006 because of anomaly probably

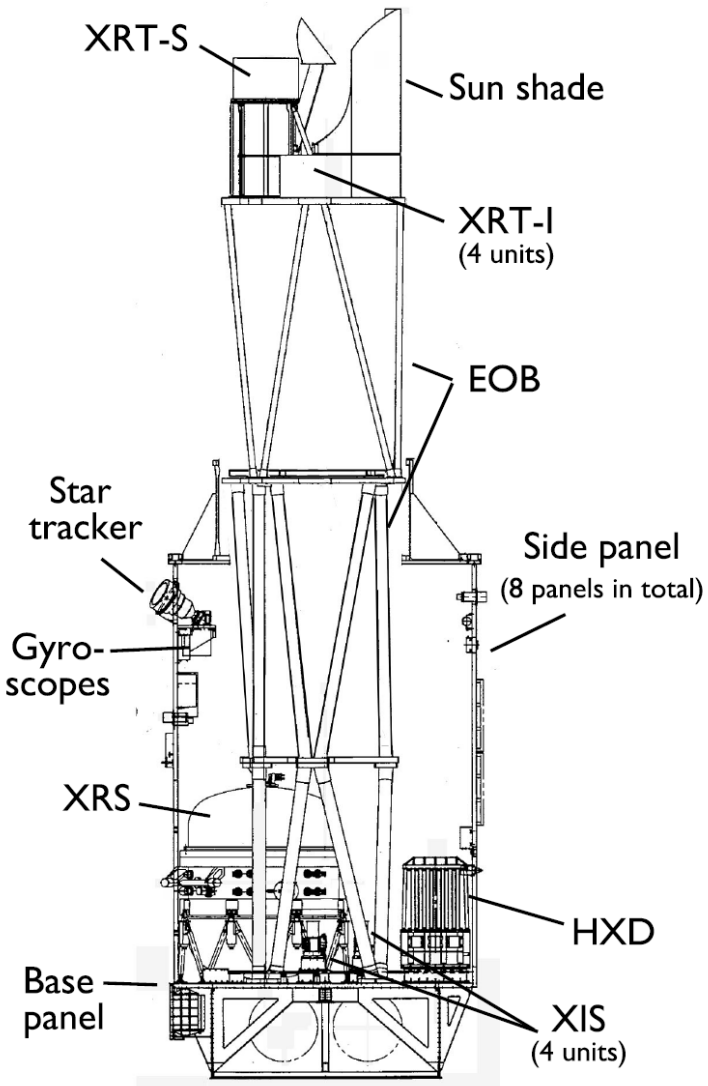

Figure 3.2: A schematic side view of Suzaku with the internal structures (Mitsuda et al. 2007).

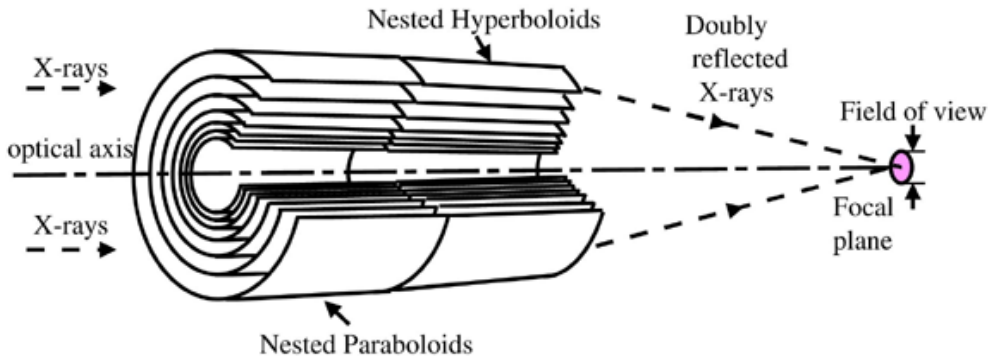

Figure 3.3: [A schematic picture of Walter type I optics which consist of an parabolic mirror followed by a hyperbolic mirror. X-ray photons are focused through the reflection by the two quadric surfaces.

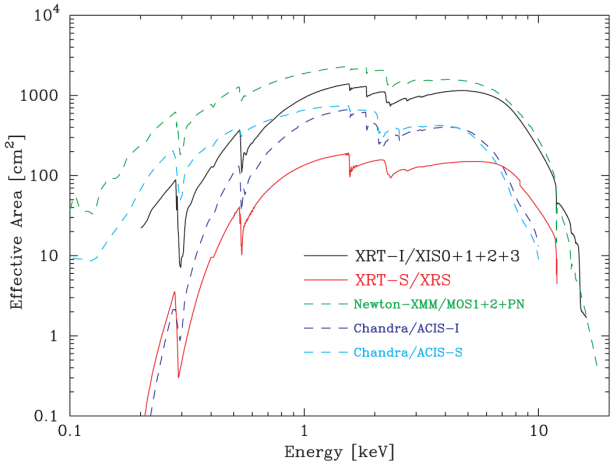

Figure 3.4: The total on-axis effective area of Suzaku, XMM-Newton and Chandra (Serlemitsos et al. 2007).

Table 3.1: Overview of Suzaku capabilities.

XRT	Focal Length	4.75 m
	Field of View	$17'$ at 1.5 keV
		$13'$ at 8 keV
	Geometrical Area/telescope	873 cm^2
	Weight/telescope	19.3 kg
	Effective Area/telescope	440 cm^2 at 1.5 keV
		250 cm^2 at 8.0 keV
	Angular Resolution	$2'.0$ (Half Power Diameter)
XIS	Field of View	$17'.8 \times 17'.8$
	Bandpass	0.2–12 keV
	Number of Pixels/CCD	1024×1024
	Pixel Size	24 μm $\times$ 24 μm
	Energy Resolution	$\sim$130 eV at 6 keV
	Effective Area	340 cm^2 (FI), 390 cm^2 (BI) at 1.5 keV
		150 cm^2 (FI), 100 cm^2 (BI) at 8 keV
	Time Resolution	8 s (Normal mode), 7.8 ms (P-Sum mode)
HXD	Field of View	$4^\circ.5 \times 4^\circ.5$ ($\geq$ 100 keV)
		$34' \times 34'$ ($\leq$ 100 keV)
	Bandpass	10–600 keV
		(PIN) 10–70 keV
		(GSO) 40–600 keV
	Energy Resolution	(PIN) $\simeq$ 4.0 keV (FWHM)
		(GSO) $7.6/\sqrt{E_{\rm MeV}}$ % (FWHM)
	Effective Area	$\simeq$ 160 cm^2 at 20 keV
		$\simeq$ 260 cm^2 at 100 keV
	Time Resolution	61 μs

caused by the micro-meteoroid hit. A part of XIS 0 also has not been used due to the excess dark current since July 2009. The XIS on the focal plane of the XRT has capability of the imaging spectroscopy in the energy range of 0.2–12 keV. A picture and schematic view of the XIS (CCD+camera body) are shown in Figure 3.6.

Each of the CCD chips has an imaging area of 1024×1024 pixels (24 $\mu m \times 24$ μm) and two frame-store regions of 512×1024 pixels (21 $\mu m \times 13.5$ μm), as shown in Figure 3.7. The CCD

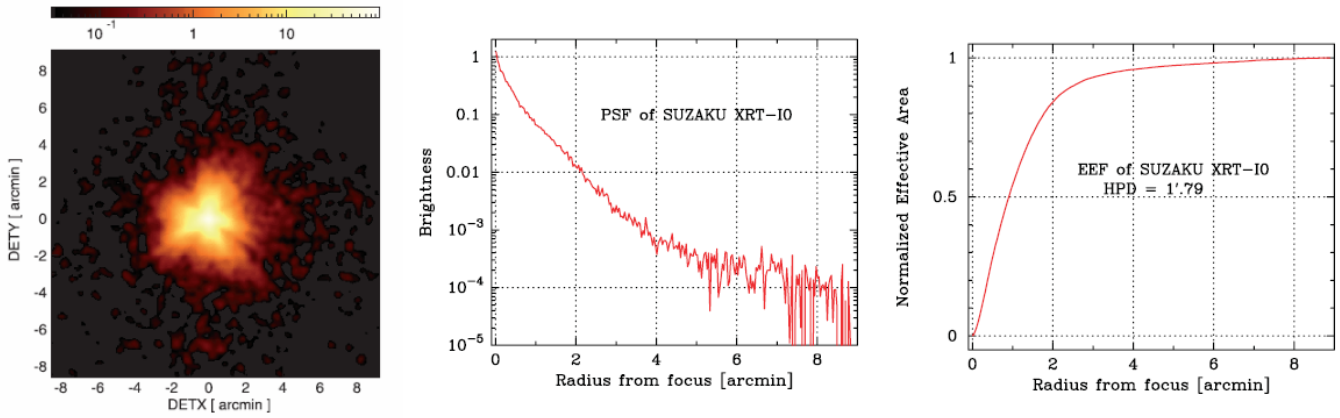

Figure 3.5: An image of a point-like source (left) with the PSF (middle) and EEF (right) of the XRT-I (Serlemitsos et al. 2007).

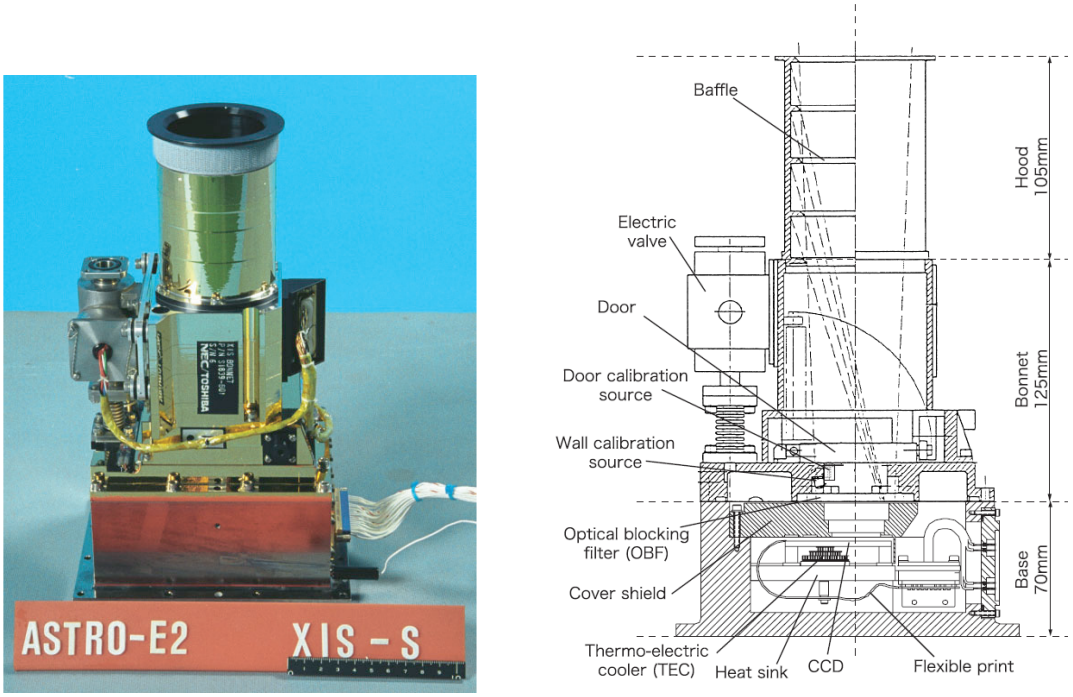

Figure 3.6: A picture of the XIS and its schematic view (Koyama et al. 2007).

is divided to four segments which has four readout nodes and each node reads the signals from 256 columns of the chip. Incident X-rays generate photoelectrons in the imaging area. They are simultaneously transferred to the frame-store regions and read by the nodes in order. Two corners of the imaging area are illuminated by two ^{55}Fe calibration sources located on the side wall of the housing for on-orbit calibration. The XIS is covered by the optical blocking filter (OBF) made of an aluminum and polyimide film because the CCD is sensitive to optical and UV light. The transparency of the OBF for X-ray is $\geq$80% above 0.7 keV while that for optical light is $\leq 5 \times 10^{-5}$.

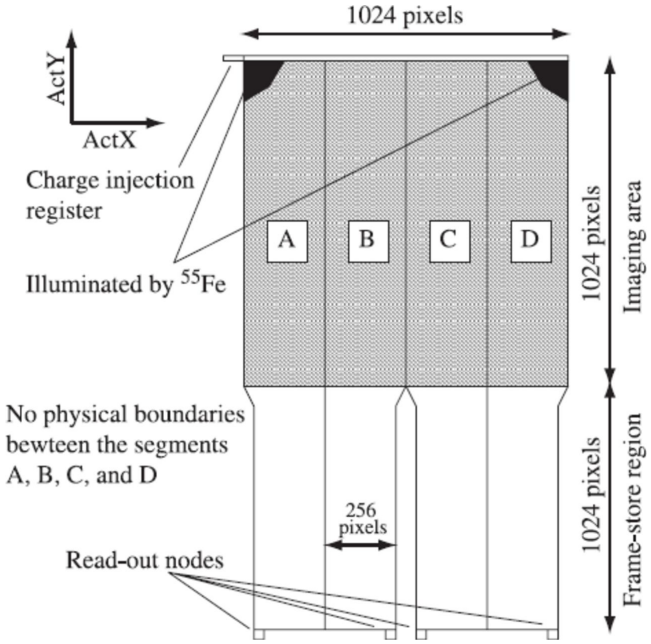

Figure 3.7: A schematic view of a CCD chip (Koyama et al. 2007).

The quantum efficiency (QE) is slightly different between the FIs and BI. Figure 3.8 shows the QE model curve based on the results of a ground calibration. The QE of the FIs above $\sim$4 keV are higher than that of BI since the depletion layer of the FIs ($\sim 75\mu m$) are thicker than that of the BI ($\sim 45\mu m$). On the other hand, the QE of the BI below $\sim$4 keV is higher than that of the FIs because of no gate structure on an X-ray incident surface. The spectral shape is not a simple Gaussian but more complicated as shown in Figure 3.9, even if incident X-rays have monochromatic energy. The energy resolution of the both CCDs achieves $\sim$130 eV at 5.9 keV (FWHM on the main peak) based on the ground calibration.

We use the Grade method to distinguish incident X-ray events from charged particle events. When an incident X-ray is absorbed in a depletion layer of the CCD, it excites a charge cloud typically smaller than a pixel size of the CCD. While the charge excited by X-ray does not occupy more than 2×2 pixels, a charged particle often produces a larger charge cloud along

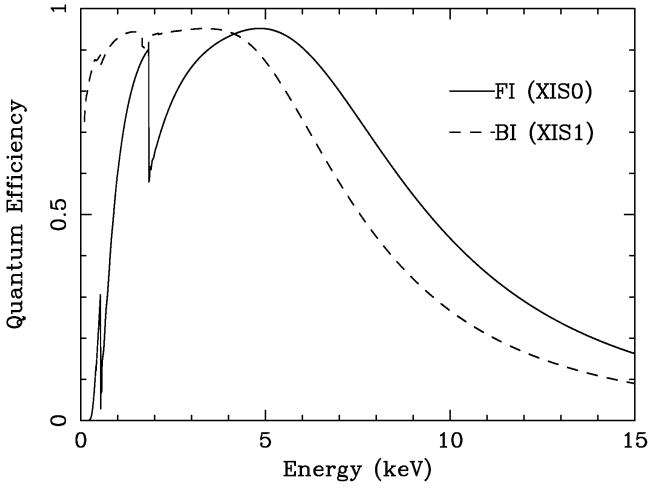

Figure 3.8: The QE curves of the XIS (Koyama et al. 2007). The solid and dashed lines show the QE of the FIs and BI, respectively.

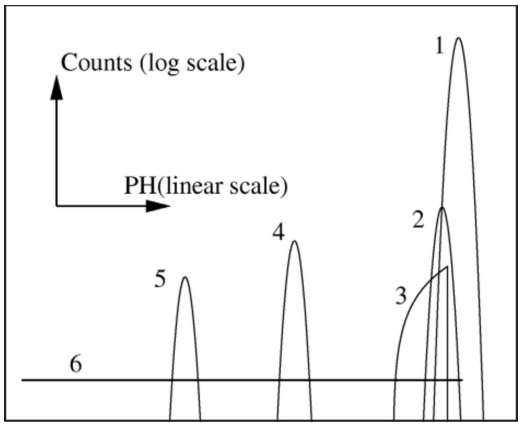

Figure 3.9: A schematic drawing of the XIS response to X-rays with monochromatic energy (Matsumoto et al. 2006). Each subscript indicates the main peak (1), sub peak (2) triangle component (3), escape peak (4), fluorescent peak (5) and continuum (6).

its track. When a pixel has a pulse-height (PH) between the lower and upper thresholds, we recognize an event and decide a local maximum PH among adjacent pixels. The surrounding 3×3 or 5×5 pixels are compared to the split threshold, then the event is classified into the each Grade. We can flexibly choose an operating mode of the XIS. The XIS has two clocking modes: the normal mode and parallel-sum (P-sum) mode. While the normal mode has a time resolution of 8 s, P-sum mode has good time resolution of 7.8 ms without any imaging capability. When we observe a bright X-ray source, this long exposure time of 8 s causes a photon pile-up. To avoid this situation, we can use two types of an window option (1/4 or 1/8) with a small area and frequent read-out. The 1/4 and 1/8 window of the CCD (256×1024 pixels and 128×1024 pixels) can be read out every 2 s and 1 s, respectively. When we observe a bright extended source to which we can not apply the window option, we can choose a burst option. The burst mode shuts out X-rays and reduce an real exposure time with keeping the original image. We can simultaneously apply the both of the window option and burst option for a extremely bright source.

The performance of the XIS is gradually degrading by radiation damage in the space environment. The degradation of the energy resolution is mostly caused by the charge transfer inefficiency. Figure 3.10 shows the time histories of the energy resolution at 5.9 keV. Since some photo-electrons are lost in the charge traps which are defects of the lattice produced by the impact of high energy particles, all of them can not be completely transferred to the read out gate. The more the charge transfer efficiency degrades, The more the uncertainty of the electron number increases. In order to restore the charge transfer efficiency, the spaced-row charge injection (SCI: Uchiyama et al. 2009) technique has been adopted since September 2006. In the SCI operation, artificial charge is injected in the imaging region during the frame-store transfer to fill the traps produced by the radiation damage. The calibration results of the degradation are reflected to the response generator (Ishisaki et al. 2007).

The XIS has the low and stable in-orbit background. Figure 3.11 shows the non X-ray background (NXB) compared with other satellite missions. They are normalized by solid angles of the FOV and their effective areas, and hence represents surface brightness of the background level. It is evident that the XIS provides the lowest background level. Furthermore, the EPIC NXB frequently shows "background flare", and the NXB count rate varies by a factor of about 100. Since the orbit altitude of other satellites is much higher than Suzaku, their instruments frequently suffer from the background spike caused by solar energetic particles. Therefore the XIS has very stable NXB.

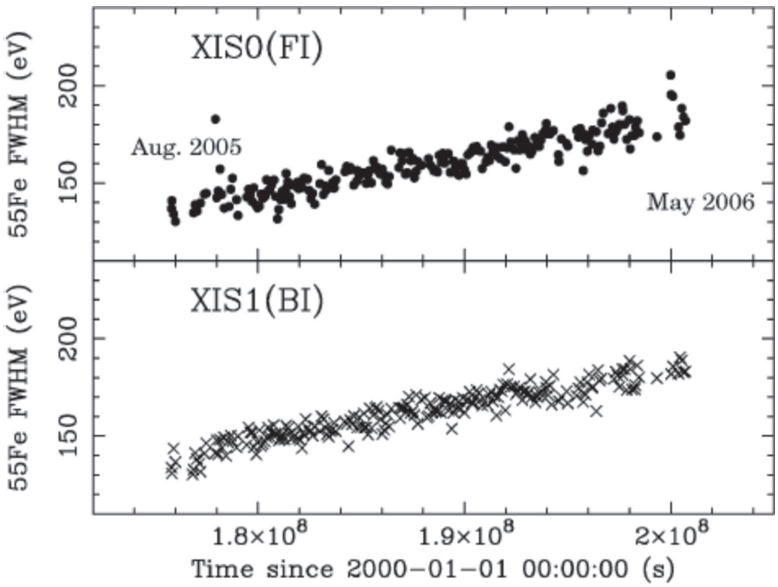

Figure 3.10: Time degradation of the energy resolution (FWHM) measured with Mn-Kα line (5.9 keV) from ^{55}Fe calibration sources (Koyama et a. 2007). The top and bottom panel show the XIS 0 and 1, respectively.

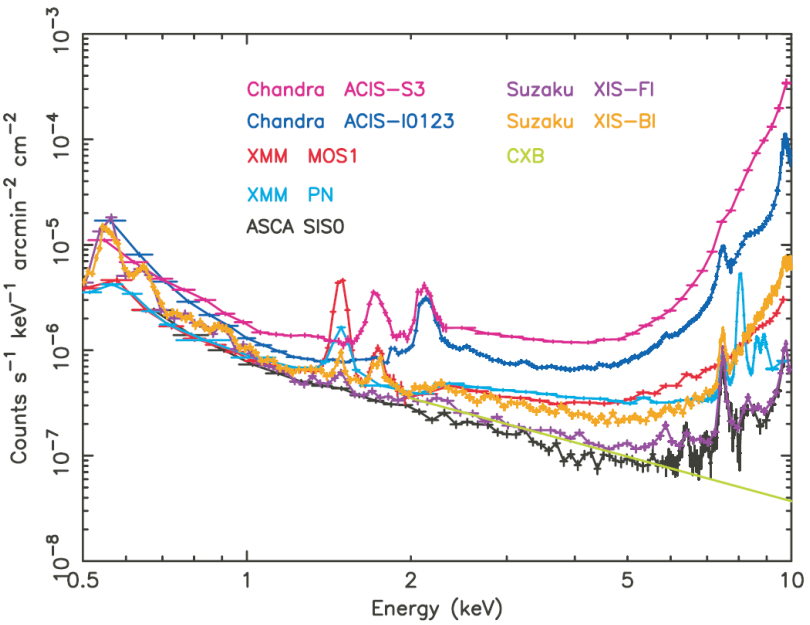

Figure 3.11: The NXB of the XIS compared with other X-ray satellite missions (Mitsuda et al. 2007). The spectra are normalized with the FOV and effective area.

3.1.3 HXD

The HXD is a non-imaging and collimated X-ray detector units covering the observation of hard X-ray in the energy range of 10–600 keV (Takahashi et al. 2007). Figure 3.12 shows a schematic view of the HXD. The HXD is consisting of 16 main detectors arranged as a 4×4 array and the surrounding 20 scintillators for active shielding. Each main detector consists of two types of detectors: 2 mm-thick PIN silicon diodes and GSO/BGO phoswich counters. The silicon PIN diodes can detect below ∼60 keV, while the GSO/BGO just located beneath the PIN covers the energy range above ∼30 keV.

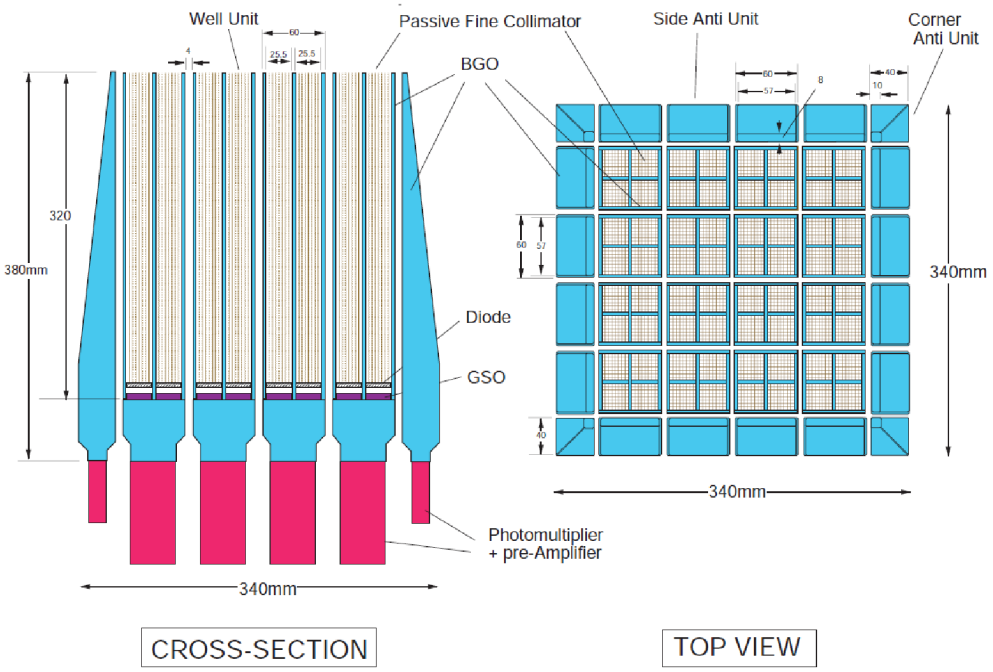

Figure 3.12: A schematic view of HXD (Takahashi et al. 2007).

The HXD is designed to achieve high sensitivity in the hard X-ray band by technique to reduce detector background. There are three steps to realize the low background level by the active shields. The first step is a well structure in which PIN and GSO are placed. They are efficiently shielded from background particles at the bottom of the deep well. The second step is the 4×4 configuration of the unit counters which work as an active shield of adjacent units. The last step is the aligned thick active shields surrounding the main detectors. The outer BGO active shields are also used as a wide-field monitoring system which is named as the Wide-band All-sky Monitor. Figure 3.13 shows the detector background of the HXD compared with instruments operated before Suzaku.

The field of view (FOV) of the HXD is collimated by two types of instruments. First, well-type BGO units collimate the FOV of the HXD to 4°.5 in full-width at half maximum (FWHM).

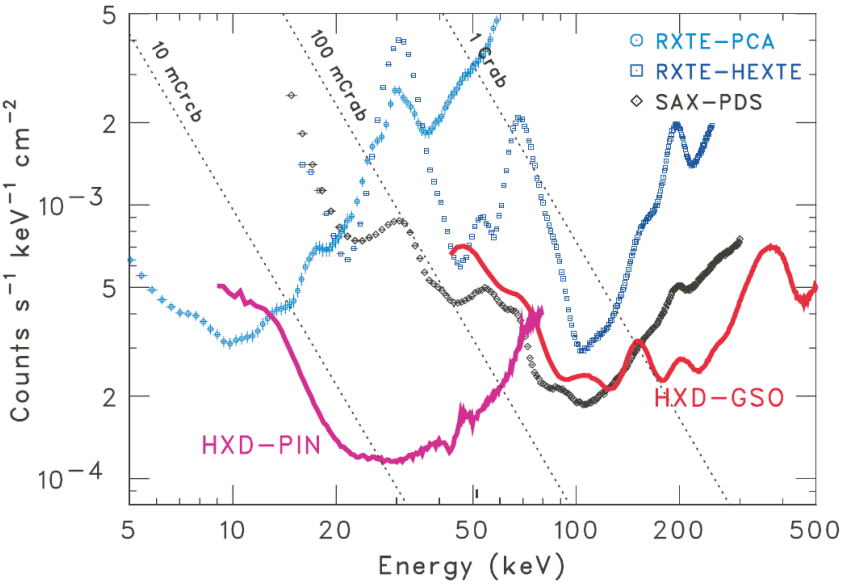

Figure 3.13: HXD background rate as a function of energy (Mitsuda et al. 2007). Background spectra of RXTE and Beppo-SAX are also plotted. The background rate is normalized with the effective area.

Second, fine collimators are tightly placed inside the BGO well. They are made of thin phosphor bronze sheets to form 300 mm length, 3 mm width square collimator (see Figure 3.12). The FOV of the HXD becomes $\sim 34'$ below 100 keV by fine collimators. However, we can not use the data obtained with the HXD because there are a lot of hard X-ray sources contaminated by one another on the Scutum Arm.

Chapter 4

SNR 3C 391

We observed and analyze four SNRs in the Scutum Arm ($l = 32°$–$35°$, $b = 0°$; see Figure 1.1). All of these SNRs are middle-aged ($\sim 10^3$–10^4 yr) SNRs interacting with molecular clouds and spatially associate with GeV gamma-ray sources. These ambient environment possibly triggers an enhancement of Fe Kα line excited by low energy CRs. All errors in this paper are 90% confidence levels, unless otherwise specified.

4.1 Overview of 3C 391

3C 391 (G31.9+0.0) is a bright Galactic SNR displaying diffuse X-ray emissions close the center of its radio shell and is classified as a mixed-morphology SNR (MM-SNR) (Reynolds & Moffett 1993). The radio shell with a radius of $5'$ has the shape of a partial circle in the north-west (NW) part and there is a faint extended structure in the south-east (SE) region. This suggests a break-out morphology into a lower density region from the main SNR shell. The detection of two OH maser spots at 1720 MHz from 3C 391 by Frail et al. (1996) indicates an interaction with molecular clouds. Frail et al. (1996) also reported a possibly extended OH emission at the edge of the NW shell. The velocity of two maser spots (105 and 110 km s^{-1}) agrees with a previous study of H I absorption velocity (Radhakrishnan et al. 1972). The H I observations show the distance to 3C 391 was determined to be between 7.2 and 11.4 kpc, assuming the Galactic center distance of 8.5 kpc. The surrounding molecular gas of 3C 391 was traced by CO ($J = 1 \rightarrow 0$) emission at velocities from 90 to 110 km s^{-1} (Wilner et al. 1998). The results of the CO observation support the theory that the early expansion of 3C 391 took place inside the dense molecular cloud and the blast wave broke out to the SE region.

The knowledge of the astrophysical environment around the SNRs is of great importance in order to consider the origin of the RPs in the context of the SNR evolution. Interestingly, most of the RP SNRs are MM-SNRs that interact with molecular clouds and are associated

with bright GeV gamma-ray emissions (IC 443, Abdo et al. 2010a; W 28, Abdo et al. 2010b; W 49 B, Abdo et al. 2010c; W 44, Abdo et al. 2010d). While young SNRs show bright TeV gamma-rays (RX J1713.7-3946, Aharonian et al. 2004), the GeV gamma-rays are thought to be radiated by middle-aged SNRs ($\sim 10^4$ yr). A significant excess (13σ) of GeV gamma rays at the position of 3C 391 with Fermi-LAT was reported by Castro and Slane (2010). The radio rim of the NW region and the closer OH maser spot are $4'$ apart from the GeV emission peak in the test statistic map. The GeV emission associated with 3C 391 probably arises from accelerated CRs in the shock-heated molecular clouds. The interaction with the molecular gas and the association of the gamma-ray emission would be the keys to understanding the morphology and the spectrum of the thermal plasmas in RP SNRs.

4.2 Observation

The observational dataset observed with Suzaku is summarized in Table 4.1. Some data are obtained from the Suzaku Key Project observations for the systematic X-ray study of MM-SNRs.

Table 4.1: The dataset of Suzaku observations.

Sequence No.	observation coordinate $(l, b)^*$	observation date	exposure (ksec)
505007010	(31.880386, 0.005569)	2010 October 22–24	99.5
507036010	(32.682518, −0.083418)	2012 April 21–22	52.2
505007010	(32.869636, −0.010021)	2012 April 20–21	55.1
506059010	(33.697806, 0.009809)	2011 April 23–25	50.9
508003010	(34.560689, −0.511922)	2013 October 22–24	66.7
508003020	(34.560689, −0.511922)	2014 April 9–10	32.4
508002010	(34.604118, −0.352247)	2013 October 24–25	61.1
508004010	(34.678643, −0.544690)	2013 October 18–19	58.3
505004010	(34.695049, −0.419993)	2010 April 10–12	61.2
508005010	(34.766164, −0.291740)	2013 October 19–21	55.7
508021010	(35.578049, −0.580142)	2013 October 27–28	51.7
508022010	(35.612266, −0.389488)	2013 October 28–30	52.6

*l and b indicate the galactic longitude and latitude, respectively.

4.2.1 Data Reduction

We reprocess the XIS data with the latest calibration results instead of using the cleaned events. We have used the HEADAS software of version 6.16 (Suzaku software of version 20). The calibration database released on 2014 July is used for data processing. In the all dataset, the XIS was operated with the normal-clocking, full-frame mode. The spaced-row charge injection technique is applied to compensate the degradation of energy resolution due to the charge transfer efficiency (Uchiyama et al. 2009). We adopt standard event selection criteria for Suzaku XIS data processing. We exclude flickering and hot pixels, events collected during the South Atlantic Anomaly, as well as data with day and night-time earth elevation angles of less than 20° and 5° respectively. Data in the two editing modes (3×3 and 5×5 pixel events) are combined.

We use standard softwares for the Suzaku analysis. The response function of the XIS and XRT is generated by *xisrmfgen* and *xissimarfgen* as the Redistribution Matrix File (RMF) and Ancillary Response File (ARF), respectively (Ishisaki et al. 2007). The detector background called as the Non X-ray Background (NXB) is estimated by *xisnxbgen* tool based on non-observational time (Tawa et al. 2008). We also use the spectral analysis software XSPEC version 12.8.1 (Arnaud 1996).

4.2.2 Background Modeling

The SNRs which we analyze are located on the Galactic plane, and hence the major background component is the Galactic ridge X-ray emission (GRXE), whose X-ray flux strongly depends on the position (e.g. Uchiyama et al. 2011, 2013). The radiation sources of the GRXE are supposed to be located at around the Galactic Center. Since the photon statistics of the background region (blank sky) is not good enough due to the limited exposure time and the effective area, subtracting the background data from the source data results in large statistical errors in the SNR spectrum. We therefore constructed a background model for the GRXE. We extracted the background spectrum from the region around Kes 78 (BG1), and fitted the GRXE model compiled by Uchiyama et al. (2013) to the spectrum. In another fields, since a photon contamination from SNRs, which is due to the leakage of the XRT point spread function into the background region, cannot be neglected, it is difficult to precisely estimate the background level of the GRXE.

Galactic Ridge X-ray Emission

To make the GRXE model, we fitted a composite model consisting of the GRXE, the cosmic X-ray background (CXB). The CXB is proposed as an assembly of unresolved point-like

sources in the extragalactic origin (e.g. Hickox & Markevitch 2006, 2007). For the CXB, we used a power-law function with a photon index 1.4, which has a flux of 8.2×10^{-7} photons cm^{-2} s^{-1} arcmin^{-2} keV^{-1} at 1 keV (Kushino et al. 2002). Uchiyama et al. (2013) composed the GRXE with a foreground plasma (FG), a low temperature plasma (LP) and a high temperature plasma (HP). All these models are thin thermal plasmas in collisional ionization equilibrium (CIE), whose temperatures are designated as $kT_{\rm FG}$, $kT_{\rm LP}$ and $kT_{\rm HP}$, respectively. We use the XSPEC APEC model by Smith 2001 to represent the CIE plasma emisssion. Metal abundances were taken relative to the solar values (Anders and Grevesse 1989). The GRXE also includes a cold matter (CM) emission with neutral iron line (6.4 keV). The CM emits the continuum radiation described as a powerlaw with index of 2.13 which is decided by the fit around the Galactic center. Thus the GRXE model is given by;

$$A_{\rm FG} \times {\rm FG} + A_{\rm GRXE} \times ({\rm LP} + {\rm HP} + {\rm CM}) + A_{\rm CXB} \times {\rm CXB}, \tag{4.1}$$

where $A_{\rm FG}$ and $A_{\rm GRXE}$ are absorptions by the Galactic H I with column densities $N_{\rm H}$ for the foreground plasma and GRXE components, respectively. An interstellar absorption of CXB ($A_{\rm CXB}$) was taken to be twice of $A_{\rm GRXE}$ because of the interstellar absorption by the front and back sides of the GRXE. The temperatures (kT_{FG}) and abundances of Ne and Mg are treated as free parameters. Although the foreground plasma has another CIE component with a temperature of $kT \sim 0.09$ keV (Uchiyama et al. 2013), we neglected this component because no significant contribution was expected in our energy range. Figure 4.2 shows the background spectrum with the best-fit background model including contamination spectrum. The best-fit parameters of the GRXE are given in Table 4.2.

4.3 Analysis and Results

4.3.1 X-ray Image

X-ray diffuse emission is clearly detected in the central region of the radio rim of 3C 391. Figure 4.3 shows an X-ray image of 3C 391, after correcting the vignetting effect and subtracting the NXB.

The north-west (NW) region associated with the radio rim has harder X-rays than the south-east (SE) region. This indicates the difference in the thermal plasma or circumstellar matters between those regions. We thus simply divided the image into two regions: the NW and SE regions.

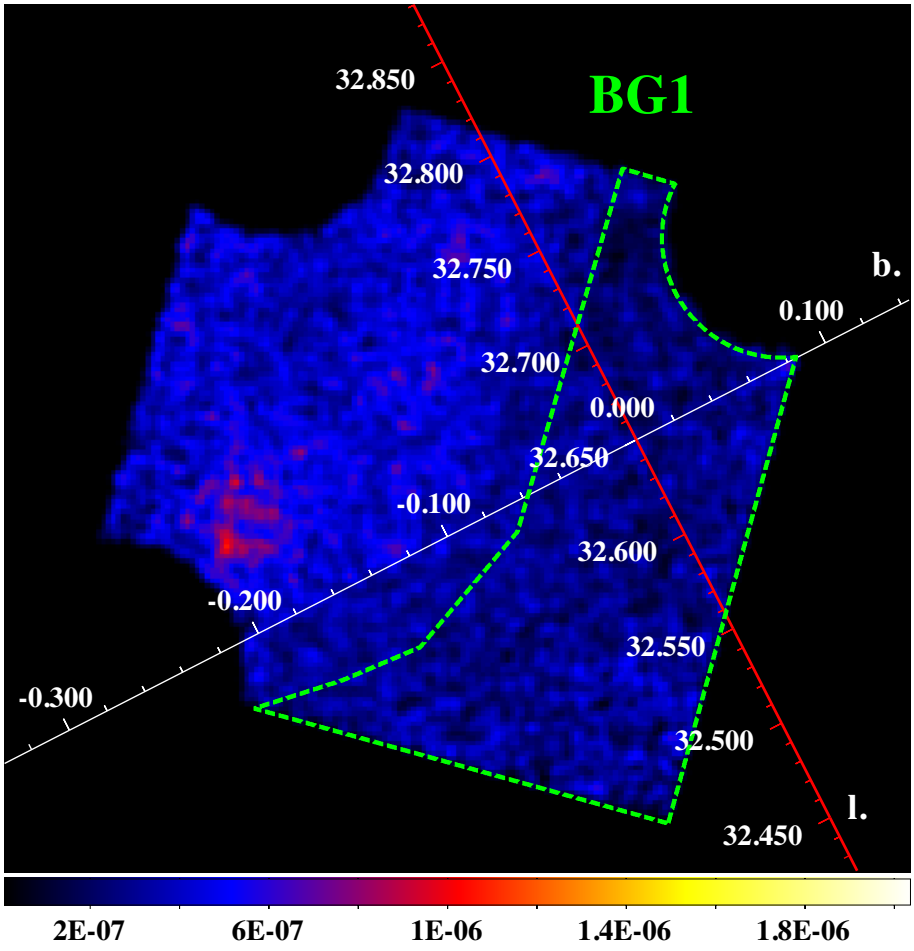

Figure 4.1: NXB-subtracted image (0.8–3.0 keV) of blank sky (BG1) after correcting for vignetting and exposure time in units of photons s^{-1} keV^{-1} cm^{-2}. The dashed line indicates the background region. The red line denotes the galactic latitude $b = 0.0°$.

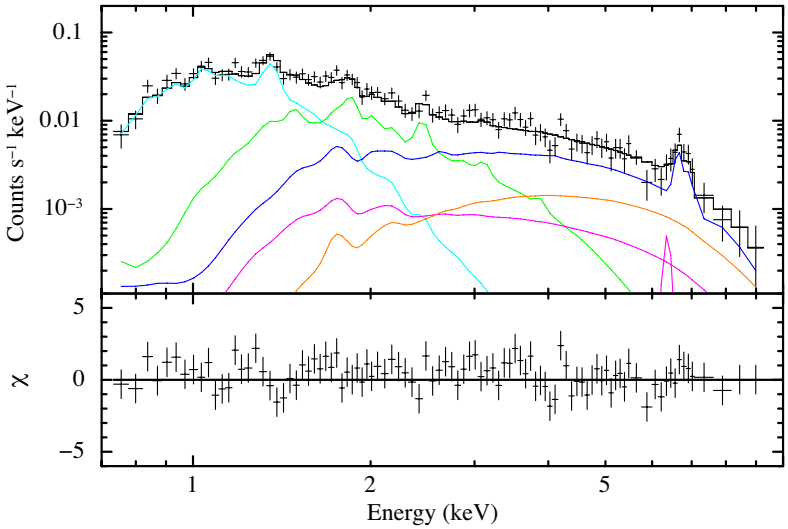

Figure 4.2: NXB-subtracted spectrum extracted from the BG1 region (see Figure 4.1). The best-fit model is shown with the black line. For visibility, only merged FI data are displayed. The solid lines show the background components of FG (cyan), LP (green), and HP (blue). The magenta and orange lines shows Fe I Kα and CXB, respectively.

Table 4.2: Fitting parameters of the background region*.

foreground		
$A_{\rm FG}$ ($N_{\rm H;FE}$ 10^{22} cm^{-2})	0.69 ± 0.13	
kT (keV)	0.39 ± 0.04	
Ne (solar)	$0.13^{+0.07}_{-0.04}$	
Mg (solar)	$0.15^{+0.06}_{-0.03}$	
others (solar)	$0.05^{+0.05}_{-0.02}$	
Flux (10^{-6} s^{-1} cm^{-2} arcmin^{-2})	$1.4^{+0.5}_{-0.6}$ (0.7–1.2 keV)	
GRXE	LP	HP
$A_{\rm GRXE}$ ($N_{\rm H;GRXE}$ 10^{22} cm^{-2})	2.5 ± 0.4	
kT (keV)	$0.90^{+0.08}_{-0.10}$	$8.4^{+1.8}_{-1.6}$
Abundance (solar)	$0.44^{+0.24}_{-0.15}$	$1.1^{+0.7}_{-0.4}$
Flux (10^{-6} cm^{-2} s^{-1} arcmin^{-2})	$1.2^{+0.7}_{-0.4}$ (2.3–5 keV), 0.42 ± 0.13 (5–8 keV)	
Fe I Kα (10^{-8} cm^{-2} s^{-1} arcmin^{-2})	$0.8^{+1.1}_{-0.8}$	
χ^2/ d.o.f	673.80/567	

* The uncertainties are the 90% confidence range.

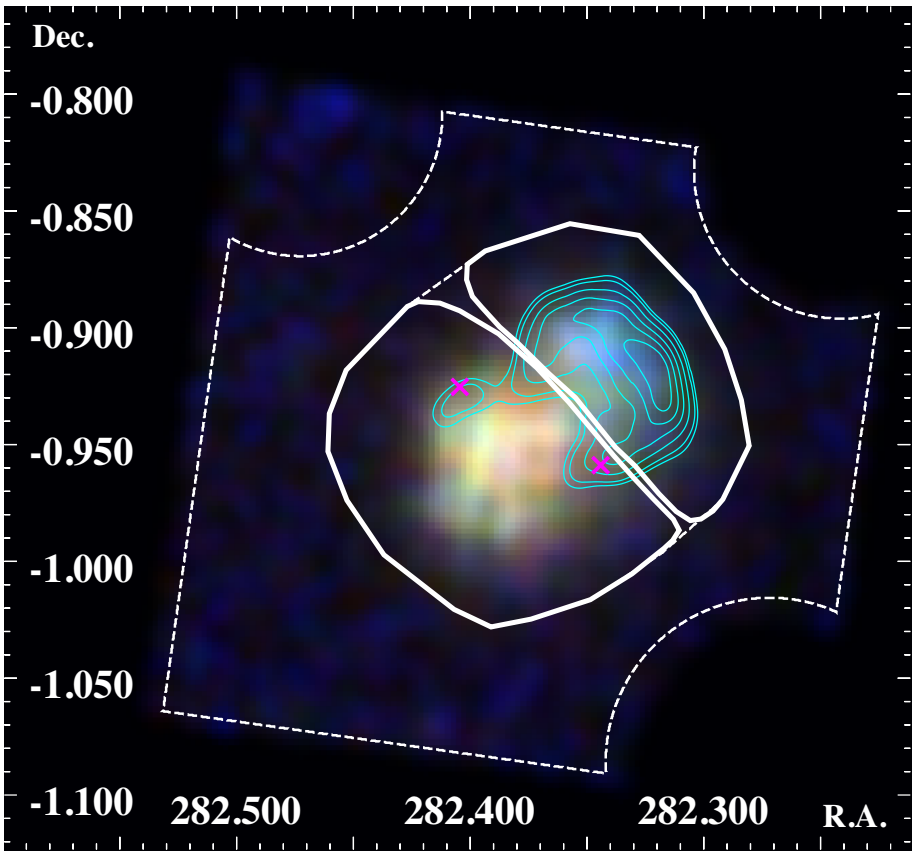

Figure 4.3: NXB-subtracted XIS image of 3C 391 after the correction of vignetting effect. The energy bands are 0.8–1.7 keV (red), 1.8–3.0 keV (green), and 3.0–5.0 keV (blue). The solid and dashed lines indicate the source regions (NW and SE) and background region, respectively. Contours show a flux map of 1.4 GHz by Very Large Array (Condon et al. 1998). Locations of OH masers are plotted with the magenta crosses (Frail et al. 1996). Photons in 8×8 pixels ($8'.32 \times 8'.32$) were summed and smoothed with a Gaussian kernel of $\sigma = 2'.6$.

4.3.2 Background Estimation

We extracted the background spectrum from the region excluding 3C 391 in the same field of view, and use the GRXE model estimated in Section 4.2.2. In this background region, photon contamination from 3C 391 at the level of a few per cent, which is due to the leakage of the XRT PSF into the background region, cannot be neglected.

In order to construct the background model, we need to make a phenomenological model both for the source and for the background regions. We extracted spectra from the whole 3C 391 region and the background region after subtracting the NXB. After the vignetting correction, we subtracted the background spectrum from the 3C 391 spectrum. We simultaneously fitted all the XIS 0, 1, and 3 data with a model. The energy band from 1.7 to 1.8 keV were ignored because of the calibration uncertainty around the Si K edge. We then modeled the spectra by using a phenomenological model: the continuum X-ray emission is described by bremsstrahlung with temperature kT_b, and line emissions from various ionized atoms are given by Gaussian lines. This phenomenological model successfully reproduces the data (χ^2/ d.o.f = 404.01/307). Figure 4.4 and Table 4.3 show the best-fitting spectrum and parameters, respectively.

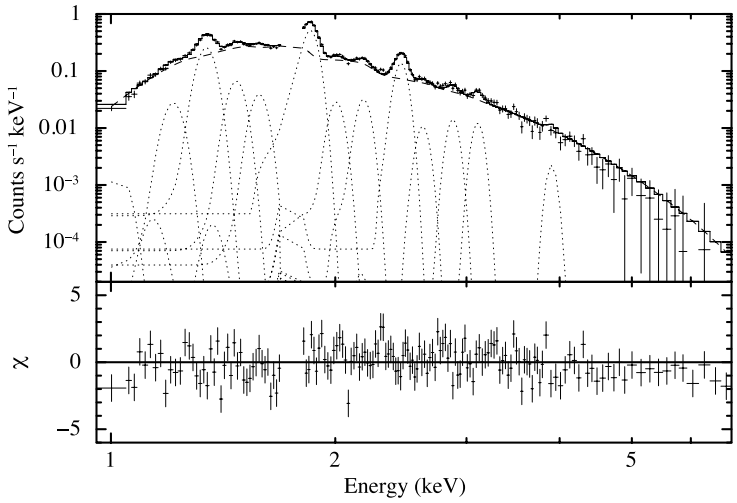

Figure 4.4: X-ray spectrum of 3C 391 with the best-fitting phenomenological model (solid line). Only a merged spectrum of FI CCDs are shown for visibility. The dashed line shows bremsstrahlung emission and the dotted lines correspond to atomic line emissions.

The BG1 and background spectra are simultaneously fitted with the GRXE model, where the background spectrum is added by the best-fit phenomenological spectrum whose contamination level is estimated by ray tracing (Ishisaki et al. 2007). The simultaneous fit gives a

Table 4.3: Parameters of the phenomenological model*.

Parameter	bremsstrahlung	
$N_{\rm H}$ (10^{22} cm^{-2})	1.90±0.05	
$kT_{\rm b}$ (keV)	0.671±0.014	
Emission line	energy (keV)†	intensity‡
Ne X Lyα	1.022	11±10
Ne X Lyβ	1.211	23±8
Mg XI Kα	1.341±0.001	103±9
Mg XII Lyα	1.472	14.7±2.6
Mg XI Kβ	1.579	7.1±1.9
Si XIII Kα	1.850±0.002	90±3
Si XIV Lyα	2.006	3.6±0.8
Si XIII Kβ	2.183	3.2±0.5
S XV Kα	2.451±0.002	15.9±0.6
S XVI Lyα	2.621	1.1±0.4
S XV Kβ	2.877	1.3±0.3
Ar XVII Kα	3.107	1.02±0.24
Ca XIX Kα	3.903	0.16±0.13
χ^2/ d.o.f	404.01/307	

* The uncertainties are the 90% confidence range.

† The centroid energies of strong Kα lines are free because they are fundamentally shifted by the contribution of another faint emission lines.

‡ The units are 10^{-5} photons cm^{-2} s^{-1}.

reduced χ^2 value of 458.73/312. Figure 4.5 shows the background spectrum with the best-fitting background model including the contamination spectrum.

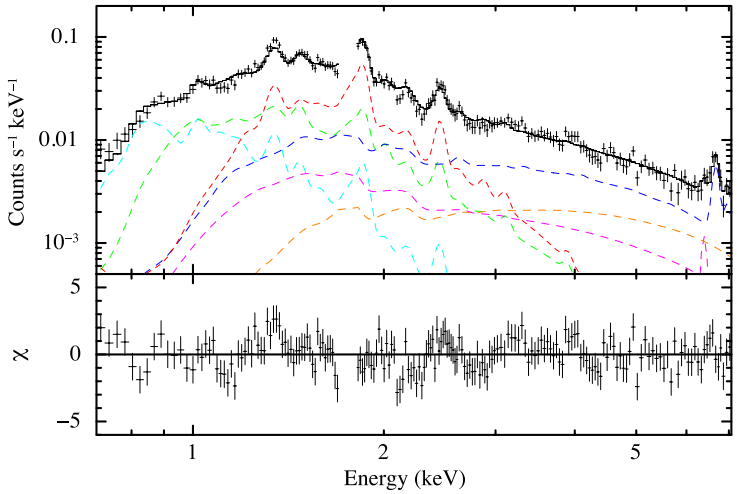

Figure 4.5: NXB-subtracted spectrum extracted from the background region (black crosses). The best-fitting model is shown with the solid line. For visibility, only merged FI data are displayed. The dashed lines show the background components of FG (cyan), LP (green), and HP (blue). The magenta and orange lines shows Fe I K α and CXB, respectively. The contamination spectrum from 3C 391 is shown by the red line.

4.3.3 The Plasma Model Fit to the Overall Spectrum of 3C 391

We fitted several plasma models to the NXB-subtracted spectrum in the entire region of 3C 391. The GRXE model function determined in the previous section was included in the model fitting. The abundances of Ne, Mg, Al, Si, S, Ar, Ca, and Fe were free parameters. We first tried the APEC model, a single-temperature (kT), optically thin thermal plasma model in the CIE state. This model is rejected with a large χ^2/ d.o.f value (565.83/315).

One of the most prominent residuals is a data excess below ∼1.5 keV. We therefore added another APEC model with free parameters of metal abundances. The best-fitting metal abundances were all consistent with 1 solar. We hence fixed all the abundances to be 1 solar. Then the fit is improved to χ^2/ d.o.f = 397.51/313 (~ 1.27).

In the atomic database of the current plasma codes, the higher Rydberg series of Fe-L lines (~ 1.2 keV) are incomplete (Brickhouse et al. 2000). If we add a ~ 1.2 keV Gaussian line, χ^2/ d.o.f is well improved from ~ 1.27 to ~ 1.25. The best-fitting spectrum and parameters are given in Figure 4.6 and Table 4.4 (left column).

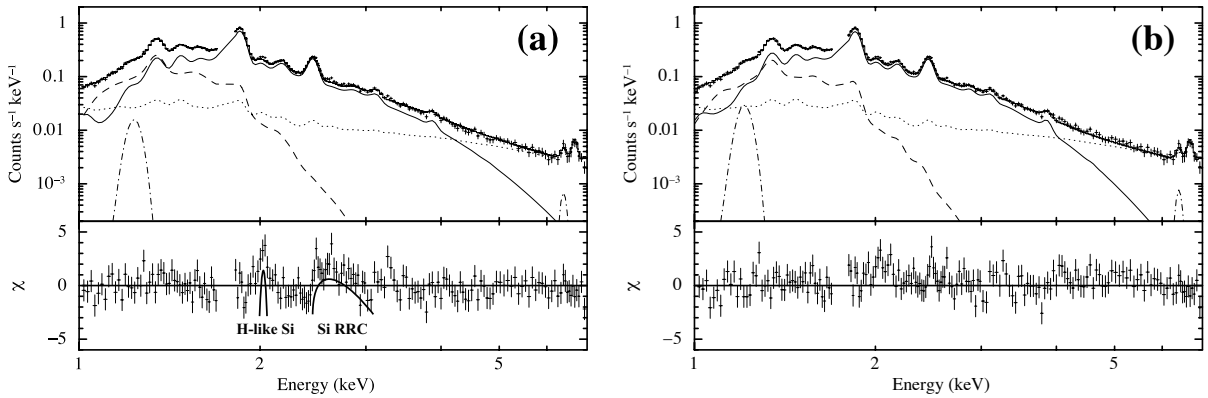

Figure 4.6: NXB subtracted spectra of 3C 391 with the best-fitting models and the residuals (lower panel) of the APEC + APEC model (a) and CIE+NEIJ model (b). For visibility, only the merged FI spectrum is displayed. The solid and dashed lines correspond to the high- and low-temperature plasma models. The background model and the Gaussian functions are shown with the dotted and dash-dotted lines, respectively.

This two-temperature CIE model still leaves significant residuals at the Si XIV Ly α line (2.006 keV), a hump-like feature at∼2.5 keV and a hint of excess at 6.4 keV. The data excess at the 2.5 keV bump above the applied model is $(2.6 \pm 0.7) \times 10^{-3}$ counts s^{-1} (2.4–2.8 keV). In the background spectrum, the data excess in the 2.4–2.8 keV band is negative and is as small as $(0.32 \pm 0.19) \times 10^{-3}$ counts s^{-1}. Thus the excess at 2.5 keV in the SNR spectrum, after the background subtraction, is not an artifact due to the background subtraction, but is a real structure. Since the bump energy of ∼2.5 keV corresponds to the S XVI Lyα line (2.623 keV) and the edge of the radiative recombination continuum (RRC) of He-like Si (2.666 keV, Yamaguchi et al. 2009b), this is likely due to a recombining plasma (e.g., Sawada & Koyama 2012). We thus applied an NEIJ model in SPEX, version 2.03.03 (Kaastra et al. 1996), for the high temperature component. This model describes a transition plasma that is initially in the CIE state with temperature kT_1, then only the electron temperature drops to kT. The recombination phase is given by the parameter $n_{\rm e}t$, where $n_{\rm e}$ and t are the number density of electrons and the elapsed time after the electron cooling, respectively.

The fit is largely improved from the two-temperature CIE model. As is shown in figure 4, the Si XIV Lyα line (2.006 keV) and hump-like feature at∼2.5 keV have disappeared, even though a hint of excess at 6.4 keV remains. The χ^2/ d.o.f becomes almost acceptable level of 355.14/315 $\sim$ 1.13. The best-fitting parameters are summarized in table 4.4 (right-hand column).

Table 4.4: Best-fit parameters of the whole region*.

	CIE Plasma		Recombining Plasma	
Parameter	CIE	CIE	CIE	NEIJ
$N_{\rm H}$ (10^{22} cm^{-2})	2.88±0.08		$3.13^{+0.14}_{-0.12}$	
$VEM^{\dagger}$ (10^{60} cm^{-3})	$3.2^{+2.3}_{-0.8}$	$0.092^{+0.011}_{-0.015}$	$2.8^{+1.4}_{-0.9}$	$0.18^{+0.03}_{-0.05}$
kT_1 (keV)	–	–	–	$1.8^{+1.6}_{-0.6}$
kT (keV)	$0.172^{+0.006}_{-0.017}$	$0.597^{+0.011}_{-0.008}$	$0.170^{+0.009}_{-0.008}$	0.495±0.015
$n_{\rm e}t$ (10^{11} cm^{-3} s)	–	–	–	$14.0^{+1.5}_{-2.2}$
Abundance (solar)				
Ne		$1.9^{+1.0}_{-0.7}$		$0.7^{+1.1}_{-0.4}$
Mg		$0.80^{+0.18}_{-0.13}$		$0.66^{+0.30}_{-0.12}$
Al		0.8±0.3		0.4±0.3
Si		$0.96^{+0.17}_{-0.11}$		$0.82^{+0.30}_{-0.12}$
S	1(fix)	$0.85^{+0.16}_{-0.10}$	1(fix)	$0.81^{+0.31}_{-0.11}$
Ar		$0.61^{+0.17}_{-0.14}$		$0.65^{+0.25}_{-0.16}$
Ca		1.0±0.5		$1.6^{+0.8}_{-0.5}$
Fe		<0.13		<0.05
others		1(fix)		1(fix)
χ^2/ d.o.f	389.68/311		355.14/315	

* The uncertainties are the 90% confidence range.

† Volume emission measure $\int n_{\rm e} n_{\rm p} {\rm d}V$ at the distance of 8 kpc, where $n_{\rm e}$, $n_{\rm p}$ and V are the electron and proton number densities (cm^{-3}) and the emitting volume (cm^3), respectively.

Since the Chandra observation shows that the spectra of 3C 391 has spatial variations with many NEI plasmas (Chen et al. 2004), we examined the excess at around 2.5 keV under the composite plasmas. We made a composite model including all NEI plasmas resolved by Chen et al. (2004). Their emission measures were fixed to their individual values. The ionization timescales determined by Chen et al. (2004) were fixed, and other timescales were free. $N_{\rm H}$ and abundances were free parameters. We also added the CIE plasma model with a low temperature (< 0.2 keV). This composite model gives the best-fitting reduced χ^2/ d.o.f of 1.47, leaving the excess of $\sim$ 2.5 keV of (2.1 ± 0.7) $\times 10^{-3}$ counts s^{-1} (2.4–2.8 keV). Also, the excess of the 6.4 keV line does not disappear. According to the spatial resolved analysis, X-ray emission of 3C 391 is mostly determined by two-temperature plasmas (kT $\sim$0.54 and 0.55 keV) with high emission measures. If we apply 1-RP model to these two plasmas, the reduced χ^2/ d.o.f value improves to 1.15. Since the best-fitting reduced χ^2/ d.o.f for the multi-NEI+CIE+RP model is not smaller than that of the CIE+RP model, we use the CIE+RP model as the best approximation for the SNR spectra, and proceed with the following analysis and discussion.

4.3.4 Spatial Distribution of the Recombining Plasma

In Figure 4.3, we can see significant difference between the NW and SE regions. We therefore analyzed the NW and SE spectra separately using the same model as was applied to the spectrum of the entire region of 3C 391.

The fit for the NW and SE regions are marginally acceptable with χ^2/ d.o.f of $333/275 \sim 1.21$ and $306/266 \sim 1.15$, respectively. However, we find no significant spectral differences except the possible presence of the 6.4 keV line in the NW region and slightly larger $N_{\rm H}$ in the SE region. The best-fit Gaussian line at $\sim$ 6.4 keV has a flux of 2.0×10^{-6} cm^{-2} s^{-1}, while that of the BG1 spectrum is 5.6×10^{-7} cm^{-2} s^{-1}. The maximum uncertainty from background subtraction is less than $\sim 10\%$ or 0.56×10^{-7} cm^{-2} s^{-1}. This value is only $\sim 3\%$ of the 6.4 keV line flux. Thus, we obtain the p-value of 0.8% through the F-test (2.4σ). Figures 4.7(a) and 4.7(b) show the results of the NW and SE regions, respectively. The best-fitting parameters of each region are shown in Table 4.5.

4.4 Discussion

The X-ray spectrum of 3C 391 is represented by two plasma models: a low-temperature CIE and a high-temperature RP. The CIE plasma is probably emitted by interstellar media heated by blast waves, because it has 1 solar abundance. The abundances of the RP are given in Figure 4.8, together with some theoretical models of Ia (Iwamoto et al. 1999) and core-collapse supernova (CC SN: Woosely & Weaver 1995). Although the error is large, the abundance

Table 4.5: Best-fitting parameters of each regions*.

	SE		NW	
Parameter	CIE	NEIJ	CIE	NEIJ
$N_{\rm H}$ (10^{22} cm^{-2})	$3.05^{+0.12}_{-0.14}$		$3.45^{+0.15}_{-0.16}$	
$VEM^{\dagger}$ (10^{60} cm^{-3})	$1.5^{+0.7}_{-0.5}$	$0.09^{+0.02}_{-0.03}$	$2.3^{+0.4}_{-1.0}$	0.08±0.02
kT_1 (keV)	–	$1.6^{+1.9}_{-0.5}$	–	$2.7^{+\infty}_{-2.0}$
kT (keV)	$0.184^{+0.012}_{-0.010}$	0.50±0.02	$0.159^{+0.014}_{-0.005}$	0.55±0.02
$n_{\rm e}t$ (10^{11} cm^{-3} s)	–	14^{+2}_{-3}	–	15±2
Abundance (solar)				
Ne		$1.3^{+1.9}_{-0.8}$		$0.5^{+1.3}_{-0.4}$
Mg		$0.85^{+0.51}_{-0.22}$		$0.56^{+0.31}_{-0.17}$
Al		$0.6^{+0.4}_{-0.5}$		$0.2^{+0.4}_{-0.1}$
Si		$1.1^{+0.6}_{-0.2}$		$0.62^{+0.24}_{-0.10}$
S	1(fix)	$1.1^{+0.6}_{-0.2}$	1(fix)	$0.59^{+0.24}_{-0.12}$
Ar		$0.9^{+0.5}_{-0.3}$		$0.32^{+0.23}_{-0.18}$
Ca		$2.2^{+1.3}_{-0.8}$		$0.5^{+0.6}_{-0.4}$
Fe		<0.08		<0.5
others		1(fix)		1(fix)
$f_{6.4}{}^{\ddagger}$	2.1±0.9		<0.5	
χ^2 / d.o.f	332.72/275		306.32/266	

* The uncertainties are the 90% confidence range.

† Volume emission measure $\int n_{\rm e} n_{\rm p} {\rm d}V$ at the distance of 8 kpc, where $n_{\rm e}$, $n_{\rm p}$ and V are the electron and proton number densities (cm^{-3}) and the emitting volume (cm^3), respectively.

‡ The units are 10^{-6} photons cm^{-2} s^{-1}.

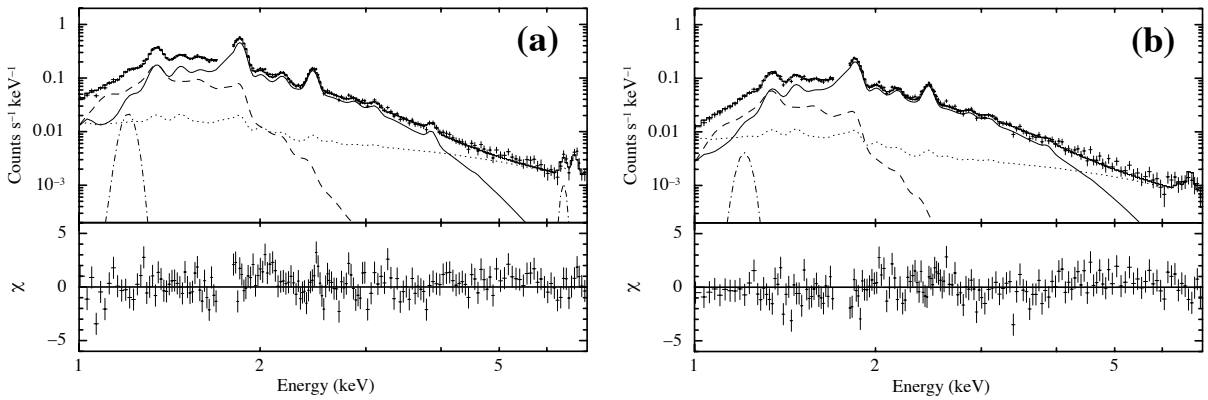

Figure 4.7: NXB subtracted spectra of the SE region (a) and the NW region (b) with the best-fitting models and these residuals. For visibility, only the merged FI spectrum is displayed. Solid and dashed lines correspond with the NEIJ and CIE models, respectively. The background model and Gaussian functions are shown with the dotted and dash-dotted lines, respectively.

pattern excluding Fe is similar to a CC SN of progenitor mass of about 15 $M_{\odot}$. Thus we regard that the RP is the ejecta origin from CC SN of an about 15 $M_{\odot}$ progenitor. In Section 4.4.1, we discuss the consistency of the observed data with this assumption.

The abundance of Fe in ejecta largely depends on the mass cut of the CC SN. If a major fraction of Fe was captured into a collapsed object (neutron star or black hole) in the case of 3C 391, a small abundance of Fe in the ejecta would be reasonable, unless the explosion is highly asymmetric (as is demonstrated by Yasumi et al. 2014). Another possibility is that only a small fraction of the Fe-rich ejecta has been shocked by the reverse shock (Fe-rich ejecta are expected to be located at the very inner part of the remnant). Since the Fe abundance estimated by only Fe-L lines has a large uncertainty due to their incompleteness, we cannot conclude why the abundance of Fe is lower than expected.

The recombination parameter ($n_{\rm e}t \sim 1.4 \times 10^{12}$ cm^{-3} s) is the largest among any RP discovered so far in MM-SNRs (Yamaguchi et al. 2009b, 2012; Ozawa et al. 2009; Ohnishi et al. 2011; Sawada & Koyama 2012; Uchida et al. 2012; Yamauchi et al. 2013).The spectra of the SE and NW regions also show the RP. Since the extended OH emission reported in the NW region suggests the interaction with molecular clouds, slightly higher $N_{\rm H}$ than SE would be reasonable. On the other hand, $n_{\rm e}t$ and kT show no significant difference between the two regions.

We found a hint of line emission at 6.4 keV, Fe I Kα line from the SE region. In the NW region, we obtained only an upper limit. Since the SE region is coincident with OH masers,

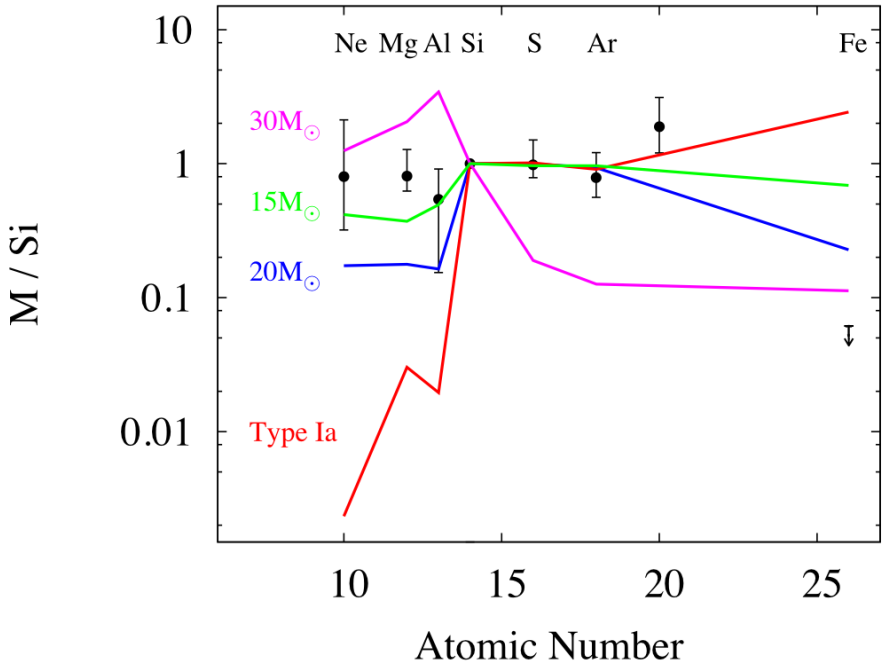

Figure 4.8: Best-fitting metal abundances of 3C 391 relative to Si abundance as a function of atomic number. The red line shows the Type Ia SN model (CDD1: Iwamoto et al. 1999). The green, blue and magenta lines represent CC-SN models with progenitor masses of 15 $M_{\odot}$, 20 $M_{\odot}$ and 30 $M_{\odot}$, respectively (Woosley & Weaver 1995).

one possibility is that the Fe I Kα line is due to low-energy CRs, which are preferentially made in the SE region. The gyro radius of the lower energy CRs is small, and hence the diffusion length is far smaller than the SNR size. No Fe I Kα line at the NW, where cool gas is denser than the SE, would be due to this limited diffusion length.

4.4.1 The Abundances and Mass of the Recombining Plasma

The abundances and emission measure of RP given in Table 4.4 are based on the H-dominant plasma. We assume that the RP is due to an ejecta of $\sim 15\ M_\odot$ progenitor, which indicate super-solar abundances even for the light elements such as He, O, and Ne. The estimations of emission measure and abundances of heavy elements largely depend on the abundances of He, O, and Ne; large abundances of these light elements enhance the continuum (mainly bremsstrahlung) flux, although the relative spectral shape is not affected because emission lines of He–Ne are absent in the relevant energy band of 1.2–7.0 keV. We thus re-estimate the emission measure and abundances of heavy elements assuming the light element mass distribution is the same as the progenitor mass of 15 $M_\odot$. The abundances of Mg–Ca relative to Si in the RP component do not change from the original H-dominant plasma but the averaged abundance of Si-Fe relative to hydrogen become $\sim$15 $M_\odot$, confirming the ejecta origin. The emission measure becomes $n_{\rm e} n_{\rm H} V f \sim (2.1^{+0.2}_{-1.7}) \times 10^{58}\ d_8^2$ cm^{-3}, where f and d8 are a filling factor and the SNR distance in the unit of 8 kpc, respectively. The ratio of the electron to the atomic hydrogen densities is $n_{\rm e}/n_{\rm H} = 1.5$ and the number ratio of all the elements to hydrogen is 2.0. Adopting the source radii of $7 d_8$ pc, the ejecta mass is estimated to be $\sim 40 f^{1/2} d_8^{5/2}\ M_\odot$. The filling factor would be very small, hence we assume f is in the range of 0.3–0.1. Then the ejecta mass is $\sim$10–25 $M_\odot$. This value is consistent with the initial assumption that 3C 391 is a remnant of a CC-SN with the progenitor mass of $\sim 15\ M_\odot$.

The age of the RP is estimated using $n_{\rm e} t$. The electron density $n_{\rm e}$ is $0.9 f^{-1/2} d_8^{-1/2}$ cm^{-3}. Then the elapsed time t is $6.5 \times 10^3 f^{-1/2}\ (n_{\rm e}/0.9\ {\rm cm}^{-3})$ yr, which places this SNR as a rather old SNR. If we assume a small filling factor, the age of 1.7×10^4 yr estimated by Chen and Slane (2001) has a very similar value.

4.4.2 Origin of the Recombining Plasma

Several scenarios are proposed to explain the formation of RPs in SNRs. One is rapid electron cooling by the thermal conduction from cold matter around SNRs (Kawasaki et al. 2002) or adiabatic rarefaction (Itoh & Masai 1989; Shimizu et al. 2012). Another is the ionization by the supra-thermal or non-thermal particles (Masai et al. 2002; Ohnishi et al. 2011) or the high-energy photons (Kawasaki et al. 2002). Therefore, the presence of RP in 3C 391 means

that the plasma experienced the rapid electron cooling or extra-ionization.

We first discuss the electron cooling scenario. If the electron cooling is due to thermal conduction, a timescale of the thermal conduction derived from the Spitzer thermal conductivity (Spitzer 1962) is

$$t_{\rm cond} \sim 1.5 \times 10^5 \left(\frac{n_e}{0.9\ {\rm cm}^{-3}}\right) \left(\frac{l}{7\ {\rm pc}}\right)^2 \left(\frac{kT}{0.50\ {\rm keV}}\right)^{-\frac{5}{2}} d_8\ {\rm yr}, \tag{4.2}$$

where l is the temperature gradient scale length. This timescale is more than twice as long as the estimated age of 3C 391, therefore the thermal conductivity is unlikely to produce the whole RP in 3C 391, the radius of which is about 7 pc.

Next we consider the scenario of rarefaction, which is the possible origin of W28 (Sawada & Koyama 2012). If the progenitor of 3C 391 was a massive star with a strong stellar wind activity, there would have been dense circumstellar media (CSM). A blast wave reached to the end of the CSM, then the IP or near CIE plasma was rarified. Thereafter only the electron temperature rapidly dropped, due to adiabatic expansion. This scenario is supported by the fact that the recombination timescale is close to the putative age of 3C 391. While Reynolds and Moffett (1993) estimated that the shell "break-out" occurred at about 1600 yr after the supernova, the blast wave breaks out of the CSM at only ∼100 yr (Itoh & Masai 1989; Shimizu et al. 2012). Since there are no significant spectral differences except the possible presence of the 6.4 keV line in NW and and slightly larger $N_{\rm H}$ value in SE, we regarded that the rarefaction of ejecta plasma was roughly symmetrical, unlike the model of W49B (Miceli et al. 2010). Our results show that the RP of 3C 391 was produced by the "break-out" from the CSM and evolved independently from the interstellar environment. For 3C 391, we apply a model of an early phase break-out (Shimizu et al. 2012), while Zhou et al. (2011) proposed a later phase break-out for W49B. This difference is due to different circumstellar environments; 3C 391 would have a more dense and compact CSM compared to that of W49B. Although the extra-ionization process could be another alternative, it is still impossible to identify the origin of RP with the present data alone.

Chapter 5

SNR Kes 79

5.1 Overview of Kes 79

Kesteven 79 (or G33.6+0.1, hereafter Kes 79) is a Galactic supernova remnant (SNR) first discovered by Caswell et al. (1975) from analysis of radio sky surveys. Kes 79 is classified as a possible MM-SNR (Rho and Petre 1998). In the radio continuum, Very Large Array (VLA) observations have revealed a peculiar double-shell morphology of the SNR with two incomplete concentric rings of apparently different radii (Velusamy et al. 1991) whose origin is still under debate. The detections of a 1667 MHz OH absorption feature along the line-of-sight with $v_{\rm LSR}$ = +95 to +115 km s^{-1} (Green 1989) and spatially coincident with a nearby molecular cloud: the CO and HCO^+ emission at velocities in the same range (e.g., Scoville et al. 1987, Green and Dewdney 1992), suggest that the SNR shockwave is interacting with the dense molecular clouds. The distance to the SNR has been estimated to be around 6.5 to 7.5 kpc through H I absorption (Case and Bhattacharya 1998) and 7.5 kpc by H I velocity measurements (Giacani et al. 2009). The apparent angular size thus implies a diameter of about 20 pc.

Kes 79 is also known to be a GeV gamma-ray emitter from recent observations by Fermi (Auchettl et al. 2014). Considering the observed spectral shape and brightness of the GeV emission, the SNR is interacting with molecular clouds; the gamma-rays are most naturally interpreted as having the proton origin.

Tsunemi and Enoguchi (2002) reported that the X-ray spectrum of Kes 79 has a thermal origin and can be described by a NEI plasma with nearly uniform temperature and abundances (sub-solar). Seward et al. (2003) discovered a central compact object (CCO) using Chandra, and suggested that the SNR originated from a CC-SNR. This SNR shows filamentary structures and faint emission near the southwest (SW) of the outer radio shell (Sun et al. 2004).

X-ray spectra with better statistics were obtained by XMM-Newton observations (Giacani

et al. 2009). The global spectrum can be fitted with a single NEI plasma, where the abundances are near solar, except for Ar which shows an unusually large abundance of $5.0^{+0.8}_{-1.6}$ solar. However, all the previous observations lack sufficient photon statistics to separate the ejecta from the circumstellar components of the X-ray emission, which obviously makes it difficult to extract the mass and nature of the progenitor star. Recently, Auchettl et al. (2014) compiled the accumulated data from XMM-Newton observations of Kes 79 and performed a spatially resolved spectral analysis. They found that X-ray spectra from about half of the region require two plasma components: a 0.24 keV PSHOCK model with solar abundances, and a $\sim$0.8 keV VPSHOCK with super solar abundances. They inferred that the former is emitted by the shocked ambient material (ISM), while the latter is due to shocked ejecta. Although the spectral parameters of the VPSHOCK plasma component (i.e., temperatures, abundances and ionization parameters) are found to be roughly homogeneous in space, they claimed there is a hint of higher chemical abundances near the SNR center. These previous spectral studies were performed for energies below 3–4 keV mainly due to the high background in higher energy bands. We report a new X-ray study of Kes 79 using Suzaku data in the 0.7–7.5 keV band.

5.2 Analysis and Results

5.2.1 X-ray Image

Figure 5.1 shows the XIS images in the energy bands of 0.7–1.5 keV and 2.0–4.0 keV. Here the X-ray events of XIS 0, 1 and 3 are combined, with corrections for the vignetting effect and subtraction of the non-X-ray background (NXB).

The soft (0.7–1.5 keV) and hard (2–4 keV) band images clearly show contrasting morphologies; emission in the hard band (right) is more spatially concentrated around the CCO, while the softer emission (left) is more extended toward the SW of the outer radio shell (e.g. Giacani et al. 2009). This morphological contrast strongly suggests that the X-ray emission of Kes 79 has at least two distinct plasma components.

5.2.2 Background Estimation

To estimate the precise local GRXE, we use both the BG1 and the background region of Kes79 (BG2) spectra. Figure 5.2 shows the X-ray image of BG2 in the 0.8 to 3.0 keV band, where the dashed line defines the BG2 region. For simplicity, we use the notation that the "BG1-spectrum" is the NXB-subtracted spectrum from the region BG1, and similarly for BG2, Kes 79 (source), and so on. Since the BG1 and BG2 regions are close to each other, their GRXE plasmas have nearly the same parameters. However, the BG2-spectrum is contaminated by the

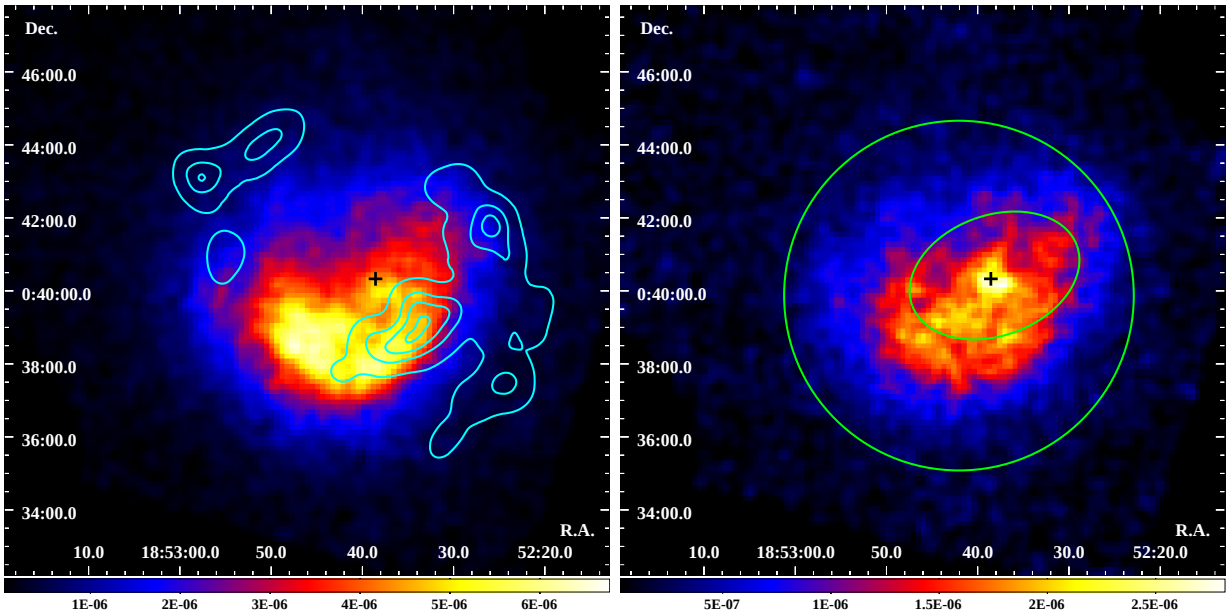

Figure 5.1: NXB-subtracted XIS images of Kes 79 after correcting for the vignetting effect in units of photons s^{-1} keV^{-1} cm^{-2}. The energy bands are 0.7–1.5 keV (left) and 2.0–4.0 keV (right). The location of the CCO is indicated by the black cross (Seward et al. 2003), and the cyan contours delineate the flux map of the 1.4 GHz emission (Condon et al. 1998). The green circles define the borders of the inner-ring and central regions of Kes 79.

pile-over flux from Kes 79. In fact, the BG2-spectrum does show strong emission lines such as Mg XI Heα and Si XII Heα (Figure 5.3), which are attributable to contamination from Kes 79. The contamination of BG1 by Kes 78, on the other hand, can be ignored because the Kes 78 flux is far lower than that of Kes 79. Since BG2 is in the same XIS field as Kes 79, it provides us a more accurate background flux and absorption than those of BG1. To obtain the spectrum of the Kes 79 contamination, we determined phenomenological Kes79-spectra by subtracting the BG2-spectrum from the Kes79-spectrum (here Pheno-Kes79-spectrum). We fit the Pheno-Kes79-spectrum with a 2-temperature bremsstrahlung model with Gaussian lines at K-shell energies of Ne, Mg, Si, S, Ar and Fe, then obtained reasonable fit with a χ^2 value of $674.1/437 \sim 1.54$. The best-fit temperatures are 0.45 ± 0.05 and 1.28 ± 0.11 keV.

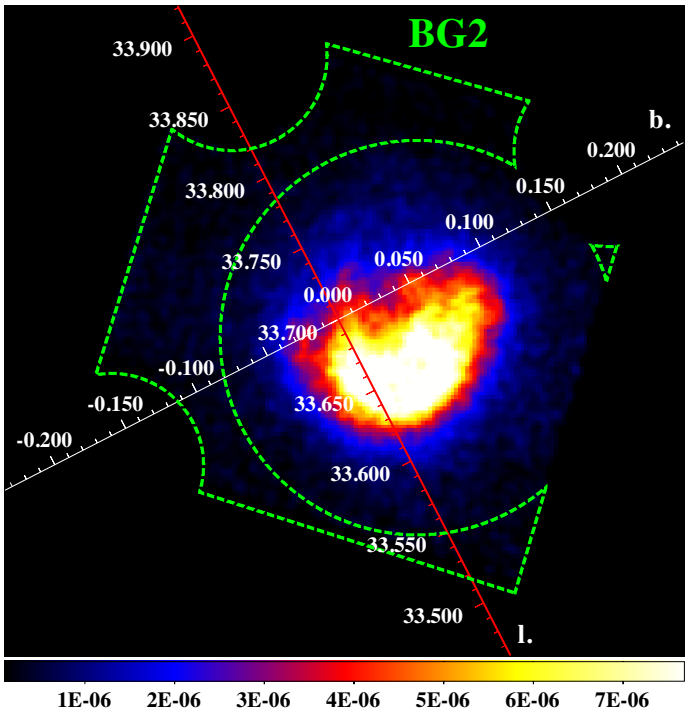

Figure 5.2: NXB-subtracted image (0.8–3.0 keV) of blank sky BG2 after correcting for vignetting and exposure time in units of photons s^{-1} keV^{-1} cm^{-2}. The dashed line indicates the background region. The red line denotes the galactic latitude $b = 0.0$.

The BG1 and BG2-spectra are simultaneously fitted with the GRXE model, where the BG2-spectrum is added by $\sim$1.1% of the flux from the best-fit Pheno-Kes79-spectrum. This contamination flux is estimated by using ray tracing (Ishisaki et al. 2007). The temperatures ($kT_{\mathrm{H}P}$) and abundances of Ne and Mg are treated as free parameters. The GRXE fluxes and absorption columns N_{H} for BG1 and BG2 are slightly different because of their different Galactic coordinates. The scale length and height ratios of BG2 and BG1 are calculated as $\sim$0.99 and

∼0.98, respectively. Then the flux ratio of the GRXE (BG1/BG2) is estimated to be 0.97 (Uchiyama et al. 2011). The simultaneous fit gives a reduced χ^2 value of 673.80/567 ∼ 1.19. The best-fit spectrum is shown in Figure 5.3. We use the GRXE parameters of BG2 around Kes 79 in the following spectral analysis.

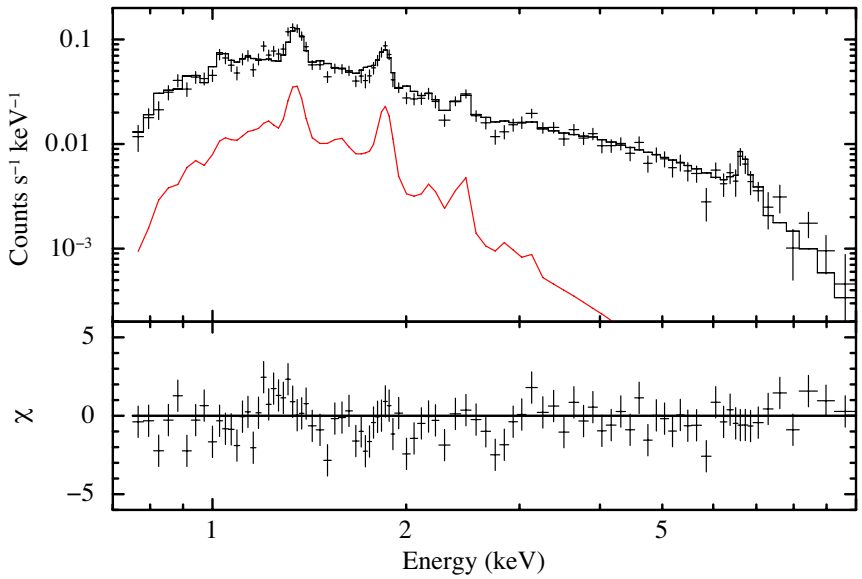

Figure 5.3: Spectrum extracted from the BG2 blank sky. The best-fit model is shown by the solid black line. For clarity, only the merged FI data are plotted. The red line shows the 'leaked' flux from Kes 79 which we denote as the Pheno-Kes79-spectrum (see text).

5.2.3 The Plasma Model Fit to the Overall Spectrum of Kes 79

The overall spectrum of Kes 79 (Kes79-spectrum) is extracted from the outer green circle in Figure 1 (right panel), after subtracting the NXB. We fit the Kes79-spectrum with a thermal plasma model adding the BG2-spectrum and the spectral model of the CCO from Seward (2003). We use the plasma code VVNEI in the XSPEC package to represent a non-equilibrium ionization (NEI) plasma. The electron temperature (kT) and ionization parameter ($n_{\rm e}t$) are free parameters, where $n_{\rm e}$ and t are the electron density and elapsed time following shock-heating. The abundances of Ne, Mg, Al, Si, S, Ar, Ca and Fe are free parameters, and those of the other elements are fixed to 1 in units of solar abundance. This model, however, leaves a line-like residual at 1.2 keV, which corresponds to the higher Rydberg series of Fe-L. In fact, the atomic data for the Fe-L line complex around 1.2 keV are incomplete in the current plasma codes. We therefore add a Gaussian line with a free center energy and flux.

Since this model is still unacceptable with a reduced χ^2/ d.o.f ∼ 1.38 with a clear excess at low energies, we add a low-temperature CIE plasma component (APEC). The best-fit abun-

dances of the APEC plasma are nearly solar. We therefore fix all the abundances to solar. The fit of the two-temperature NEIs plus CIE model is poor with a reduced χ^2/ d.o.f of ∼1.18. Significant residuals are still seen at 6.4 keV and around 2–3 keV (Figure 5.4, middle panel).

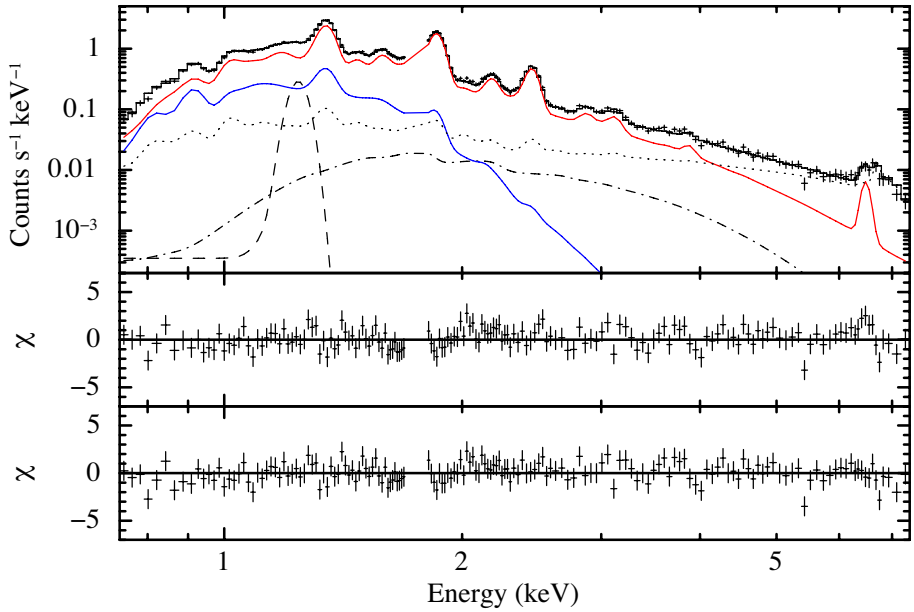

Figure 5.4: Top panel: The best-fit spectral model (solid line) for Kes 79. The multi-temperature NEI and CIE components are shown by the red and blue lines. The 1.2 keV Gaussian line, BG and CCO components are shown by the dotted, dashed and dash-dotted lines. For clarity, only the merged FI spectrum is plotted. Middle panel: residuals from the NEI+CIE+1.2 keV Gaussian line model. Bottom panel: residuals from the multi-temperature NEI+CIE+1.2 keV line model.

The residual at 6.4 keV is due to the K-shell line of nearly neutral Fe. Figure 5.5 is an expanded version of the Kes 79 and BG1+BG2 spectra around 6.4 keV. The solid lines are the best-fit model of bremsstrahlung emission plus Gaussian lines. The best-fit Gaussian line of the Kes79-spectrum at $\sim$ 6.4 keV has a flux of 4.1×10^{-6} cm^{-2} s^{-1}, while that of the BG1+BG2 spectrum is 5.6×10^{-7} cm^{-2} s^{-1}. The maximum uncertainty from background subtraction is less than $\sim$ 10% or 5.6×10^{-8} cm^{-2} s^{-1}. This value is only $\sim$ 2% of the 6.4 keV line flux detected in the Kes79-spectrum. Hence, we conclude that the detection of the 6.4 keV line feature is robust. We obtain the p-value of 0.02% through the F-test (3.5σ).

The excess at round 2–3 keV is due to an underestimation of the K-shell line complexes from Si and S. For further improvement, we fit the temperatures of the H–Mg, Si–Ca and Fe–Ni elemental groups in the NEI plasma as independent free parameters, while the normalizations are linked to each other. The best-fit χ^2/ d.o.f. is improved to $\sim$ 1.09 (Figure 5.4, lower panel). This improvement is significant with a F-test null probability better than ∼4 %.

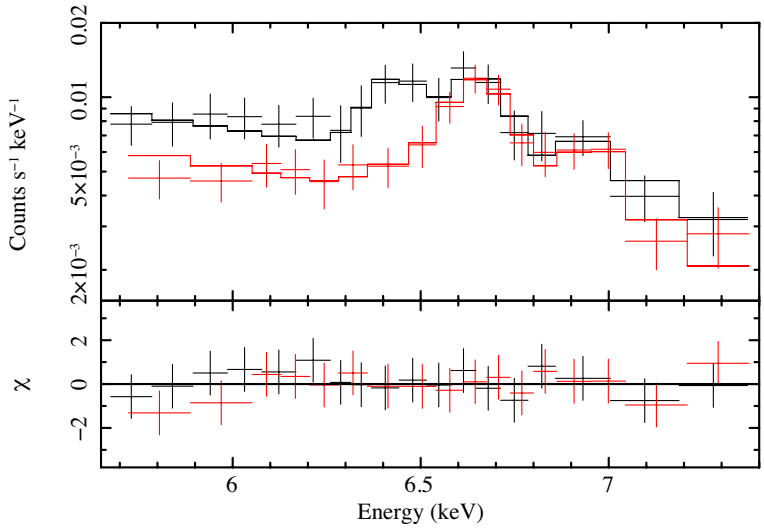

Figure 5.5: The Kes79-spectrum (black), and the BG1+BG2 spectrum (red) used for background subtraction, zoomed in around 6.4 keV. The solid lines represent our best-fit models which include a bremsstrahlung component plus Gaussian lines.

Statistically, this model is still unacceptable in the χ^2 test, possibly due to some systematic errors. In fact, we can obtain no further improvement by adding more components and/or changing to other trial models. We therefore adopt this model as the best approximation for the overall spectrum from Kes 79. The best-fit model and spectral parameters are given in Figure 5.4 and Table 5.1 (Model A), respectively. In this model (Model A), the 6.4 keV line is regarded as the ejecta plasma with low ionization of Fe.

The observed centroid energy of the 6.4 keV line does not exclude an origin from neutral irons, thus it is probable that the line is not emerging from a hot plasma in an extremely low ionization state. We therefore attempt to fit this line by a Gaussian line (Model B). In Model B, the plasma component is essentially the same as Model A, but the NEI plasma now consists of two temperature components for the H–Al and Si–Fe elemental groups respectively. Model B yields an equally good fit as Model A, with a χ^2_ν/ d.o.f of $\sim$1.10. The best-fit parameters are given in Table 5.1 (Model B).

5.2.4 Spatially Resolved Spectra

Auchettl et al. (2014) reported that the spatial distribution of temperature and abundances in Kes 79 is roughly uniform, but show a hint of small enhancement in the central region. We therefore divide the whole region into two parts: the central region around the CCO with a size of 5×3 arcmin^2 (i.e., the region bounded by the inner green ellipse in the right panel of Figure 5.1), and the inner radio shell region (the remaining region of Kes 79 in the right panel

Table 5.1: Best-fit parameters of multi-kT+ CIE + Gaussian line model*.

	Overall	
	model A	model B
$N_{\rm H}(10^{22}{\rm cm}^{-2})$	$1.44^{+0.03}_{-0.04}$	1.49 ± 0.03
NEI		
kT_1 (keV)	$0.81^{+0.06}_{-0.05}$	0.84 ± 0.05
$n_{\rm e}t_1$ ($10^{10}{\rm cm}^{-3}$ s)	6.8 ± 0.8	$6.3^{+1.1}_{-0.9}$
Ne	0.92 ± 0.13	$1.02^{+0.13}_{-0.12}$
Mg	$1.12^{+0.08}_{-0.10}$	$1.19^{+0.10}_{-0.05}$
Al	$0.84^{+0.15}_{-0.18}$	0.8 ± 0.2
kT_2 (keV)	$0.96^{+0.11}_{-0.10}$	$0.95^{+0.16}_{-0.12}$
$n_{\rm e}t_2$ ($10^{10}{\rm cm}^{-3}$ s)	$6.0^{+1.7}_{-1.3}$	$4.7^{+1.3}_{-1.1}$
Si	$0.82^{+0.15}_{-0.12}$	$0.88^{+0.19}_{-0.16}$
S	$0.93^{+0.20}_{-0.15}$	$1.09^{+0.26}_{-0.22}$
Ar	$0.7^{+0.3}_{-0.2}$	$1.0^{+0.4}_{-0.3}$
Ca	$1.7^{+1.6}_{-1.0}$	$2.8^{+2.3}_{-1.6}$
kT_3 (keV)	$2.5^{+0.3}_{-0.2}$	$= kT_2$
$n_{\rm e}t_3$ (10^{10} ${\rm cm}^{-3}$ s)	1.5 ± 0.2	$= n_{\rm e}t_2$
Fe = Ni	0.35 ± 0.05	$0.66^{+0.16}_{-0.13}$
$EM^{\dagger}$ ($10^{12}{\rm cm}^{-5}$)	3.8 ± 0.6	3.6±0.5
Fe Kα energy	-	6.39–6.48 keV
flux (10^{-6} ${\rm cm}^{-2}$ ${\rm s}^{-1}$)	-	3.0 ± 1.1
APEC		
$kT_{\rm e}$ (keV)	$0.22^{+0.02}_{-0.03}$	$0.22^{+0.02}_{-0.03}$
Abundances	1 (fixed)	1 (fixed)
$EM^{\dagger}$ ($10^{12}{\rm cm}^{-5}$)	20^{+9}_{-7}	21^{+11}_{-3}
χ^2_{ν}/d.o.f.	493.15/451	497.43/451

* The uncertainties are the 90% confidence range.

$^{\dagger}n_{\rm e}n_{\rm p}V/4\pi D^2$,where $n_{\rm e}$, $n_{\rm p}$, D and V are the electron and proton number densities (${\rm cm}^{-3}$),the distance (cm) and the emission volume (${\rm cm}^3$), respectively.

of Figure 5.1). We perform spectral analyses for the spectra from each regions with the same procedures and the same model (Model A and Model B) as are given in Section 5.2.3. In the center region spectrum, the abundances of Ca and Fe cannot be constrained. We therefore re-fit this spectrum by linking the abundance of Ca to that of Ar. For the same reason, the temperature and ionization parameter of the Fe–Ni plasma are linked to those of the Si–Ca plasma. We obtained reasonable fits with both Model A and B. The best-fit spectra and parameters for Model B are summarized in Figure 5.6 and Table 5.2. Since Model A gives essentially the same parameters value of Model B, we list only the Model B results.

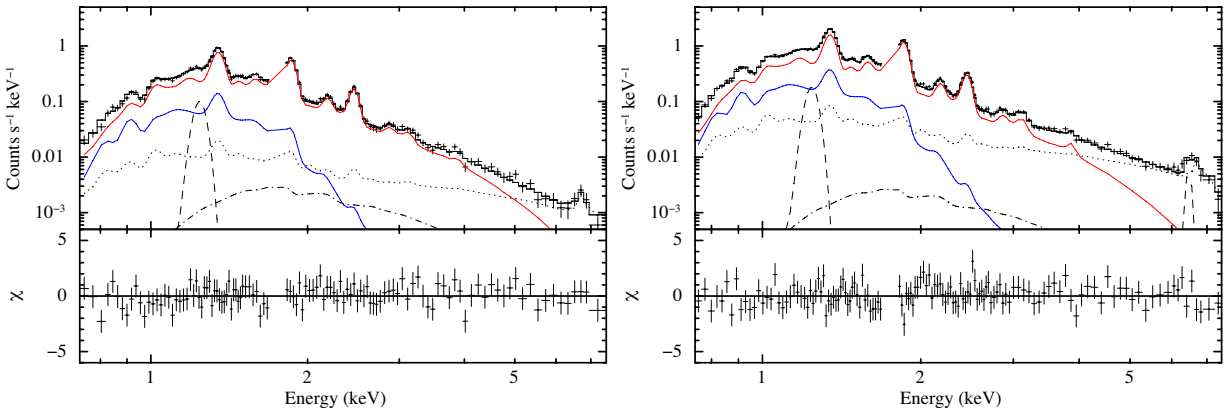

Figure 5.6: Spectra extracted from the center region (left) and the inner-ring region (right). The best fit models are shown as the solid lines (model B). The multi-temperature NEI and CIE components are shown by the red and blue lines. The 1.2 keV and 6.4 keV Gaussian lines, BG and CCO components are shown by the dotted, dashed and dash-dotted lines. For clarity, only the merged FI spectrum is plotted.

In Table 5.2, we see no significant difference in temperatures and ionization timescales between the two regions for the H–Ca plasma. We can see small enhancements of the metal abundances in the inner-ring region compared the center region. The normalization ratio between the CIE and NEI components (CIE/NEI) of the inner-ring region (~ 6) is about twice as large as that of the center region (~ 3).

Our analysis of spatially resolved spectra unveils a remarkable contrast in the distribution of the 6.4 keV iron line. The 6.4 keV line is found in the inner-ring region, but not in the center region around the CCO (Table 5.2). The spatial distribution of the 6.4 keV line is examined by constructing a narrow band image over the 6.2–6.5 keV energy band, shown in Figure 5.7. In the image the XIS 1 data are not included, because the BI CCD has much poorer signal-to-noise ratios at high energies around 6.4 keV. The CCO and the outline of the inner radio shell are shown by the red cross and cyan circle, respectively. The magenta contours show the ^{13}CO $J = 1 \rightarrow 0$ emission integrated between +99.0 and +109.0 km s^{-1} (Giacani et al. 2009). This

Table 5.2: Best-fit parameters of spatially resolved spectra*.

	Center	Inner-Ring
$N_{\rm H}(10^{22}{\rm cm}^{-2})$	$1.54^{+0.06}_{-0.07}$	1.47 ± 0.04
	NEI	
kT_1 (keV)	$0.82^{+0.06}_{-0.05}$	0.83 ± 0.06
$n_{\rm e}t_1$ ($10^{10}{\rm cm}^{-3}$ s)	6.9 ± 1.4	6.3 ± 1.2
Ne	$0.86^{+0.20}_{-0.08}$	$1.01^{+0.17}_{-0.15}$
Mg	$0.91^{+0.11}_{-0.10}$	$1.25^{+0.13}_{-0.11}$
Al	0.4 ± 0.3	1.0 ± 0.3
kT_2 (keV)	$1.0^{+0.3}_{-0.2}$	$0.99^{+0.19}_{-0.13}$
$n_{\rm e}t_2$ ($10^{10}{\rm cm}^{-3}$ s)	5^{+4}_{-2}	$4.4^{+1.7}_{-1.4}$
Si	0.6 ± 0.2	$0.9^{+0.3}_{-0.2}$
S	$0.8^{+0.4}_{-0.3}$	1.0 ± 0.3
Ar	$0.5^{+0.4}_{-0.3}$	$1.0^{+0.4}_{-0.3}$
Ca	=Ar	$3.0^{+1.9}_{1.7}$
kT_3 (keV)	$= kT_2$	$= kT_2$
$n_{\rm e}t_3$ (10^{10} cm^{-3} s)	$= n_{\rm e}t_2$	$= n_{\rm e}t_2$
Fe = Ni	0.4 ± 0.2	0.8 ± 0.2
$EM^{\dagger}$ ($10^{12}{\rm cm}^{-5}$)	1.5 ± 0.3	2.3 ± 0.4
Fe Kα energy	6.4 keV (fix)	6.39–6.50 keV
flux (10^{-6} cm^{-2} s^{-1})	< 0.5	2.8 ± 1.0
	APEC	
$kT_{\rm e}$ (keV)	0.22 ± 0.05	$0.22^{+0.02}_{-0.03}$
Abundances	1 (fixed)	1 (fixed)
$EM^{\dagger}$ ($10^{12}{\rm cm}^{-5}$)	5^{+8}_{-3}	14^{+9}_{-5}
χ^2_ν/d.o.f.	278.30/349	415.60/362

* The uncertainties are the 90% confidence range.

$^{\dagger}n_{\rm e}n_{\rm p}V/4\pi D^2$,where $n_{\rm e}$, $n_{\rm p}$, D and V are the electron and proton number densities (cm^{-3}),the distance (cm) and the emission volume (cm^3), respectively.

figure clearly show that the 6.4 keV line is concentrated at the dense molecular region.

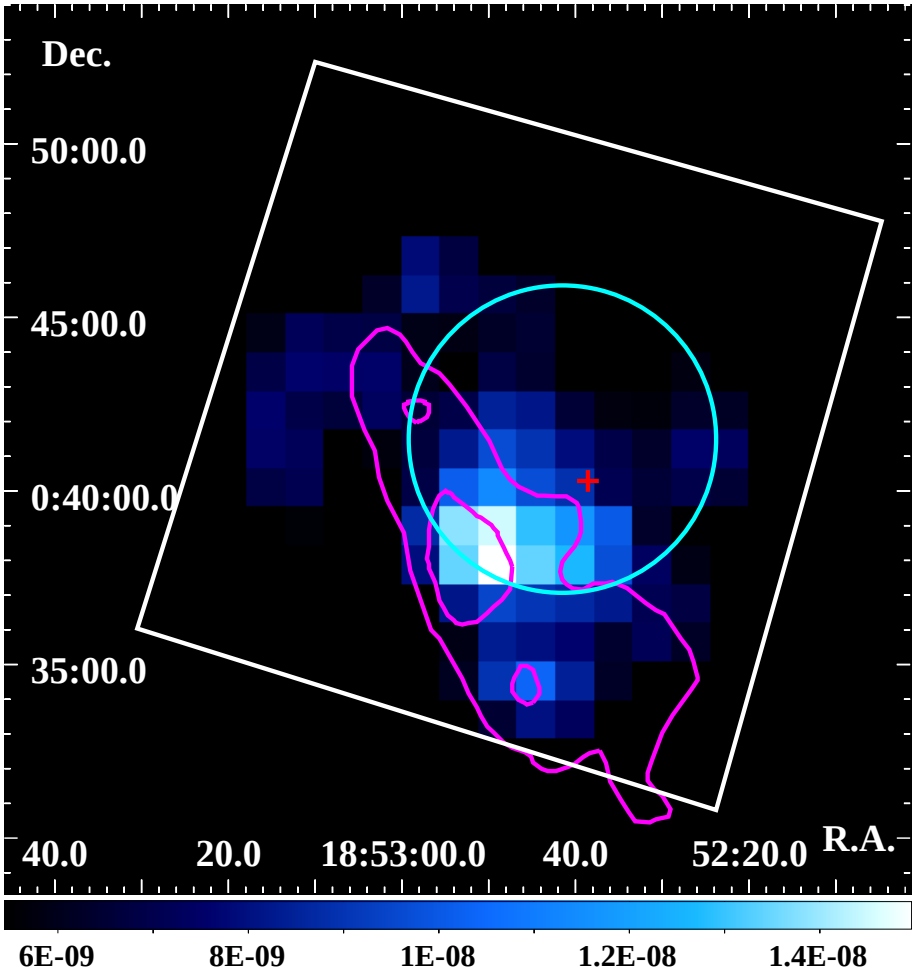

Figure 5.7: The NXB-subtracted XIS 0+3 image of Kes 79 in the energy band of 6.2–6.5 keV after correction for vignetting in units of photons s^{-1} keV^{-1} cm^{-2}. The white square shows the FOV of the XIS. The CCO and the inner radio shell are indicated by the red cross and cyan circle (Seward et al. 2003, Sun et al. 2004). The magenta contours indicate the ^{13}CO $J = 1 \rightarrow 0$ line emission integrated between +99.0 and +109.0 km s^{-1} (Giacani et al. 2009).

5.2.5 X-ray Emission from the Outer Radio Ring

Sun et al. (2004) found that Kes 79 has extended X-ray emission in the southwest (SW) of the outer radio shell. We examined more extended X-ray emission around the whole outer radio shell. The surface brightness is very low and a hint of Ne Heα line at $\sim$0.9 keV is found from the outer radio ring. We therefore extract and display a 0.86–0.96 keV band image in Figure 5.8. Then we divided the outer ring into 4 azimuthal segments (NE: red, NW: magenta, SE: green and SW: orange) and made radial profiles as shown in Figure 5.9 (top panel). To

illustrate the results more clearly, the radial profiles from all segments are summed together for the Ne IX Heα band (0.86–0.96 keV) and the Si XIII Heα (1.76–1.92 keV) band respectively, and their ratios are plotted in Figure 5.9 (bottom panel).

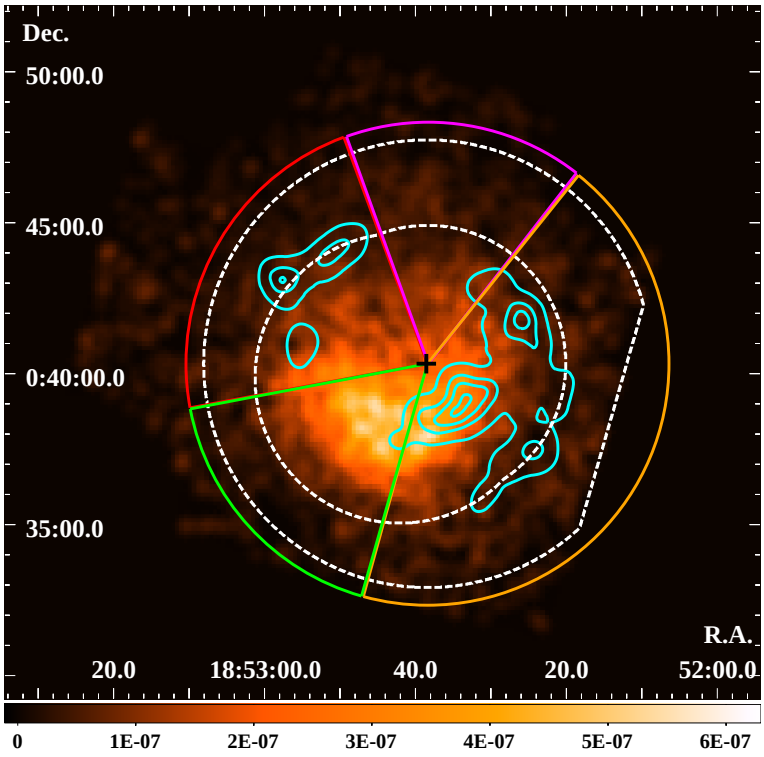

Figure 5.8: NXB-subtracted X-ray image (0.86–0.96 keV) of Kes 79 after correction for vignetting in units of photons s^{-1} keV^{-1} cm^{-2}. The location of the CCO is shown by the black cross (Seward et al. 2003). The image is smoothed by a Gaussian kernel with $\sigma = 1.3'$. The colored sections correspond to our 4 azimuthal segments. The outer-ring region is bounded between the two white dashed lines.

Figure 5.8 and 5.9 clearly show that the Ne IX Heα emission extends to a radius of $\sim$8 arcmin (the outer radio shell), which is outside the main X-ray region of Kes 79 ($\sim$5 arcmin). The X-ray spectrum is extracted from a donut-shape region defined by the two circles of radii $\sim$5 and 8 arcmin (white dashed lines in Figure 5.8). The spectrum is fitted by the same model as that given in Subsection 5.2.3 and 5.2.4. Since statistics are limited, we fixed the NEI model to that of the whole region (Table 5.1). The fit is acceptable with a χ^2/ d.o.f value of 324.69/304.

The best-fit spectrum and parameters are shown in Figure 5.10 and Table 5.3. Since the normalization ratio between the CIE and NEI components (CIE/NEI) is $\sim$100, the CIE fraction gradually increases with distance from the CCO. Thus the outer radio ring shows relative concentration of APEC, the CIE plasma. We see no 6.4 keV line from the outer radio shell

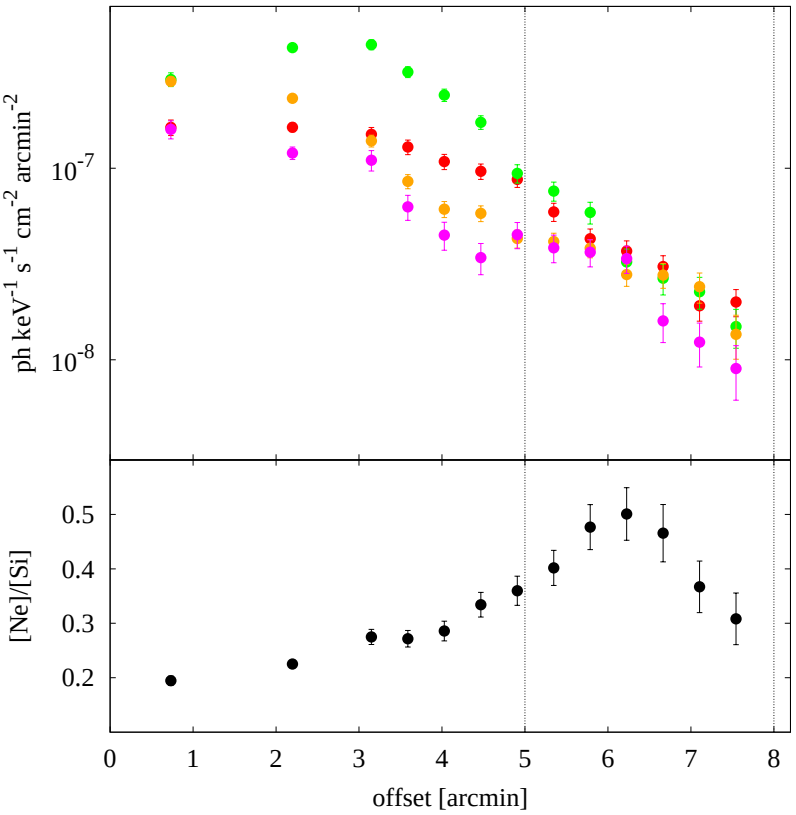

Figure 5.9: Top : Ne IX Heα (0.86–0.96 keV) radial profiles from the 4 segments, with the angular distance (offset) from the CCO position. Bottom: Radial profile of the flux ratio between Ne IX Heα (0.86–0.96 keV) and Si XIII Heα (1.76–1.92 keV) emission. All segments are summed here.

region.

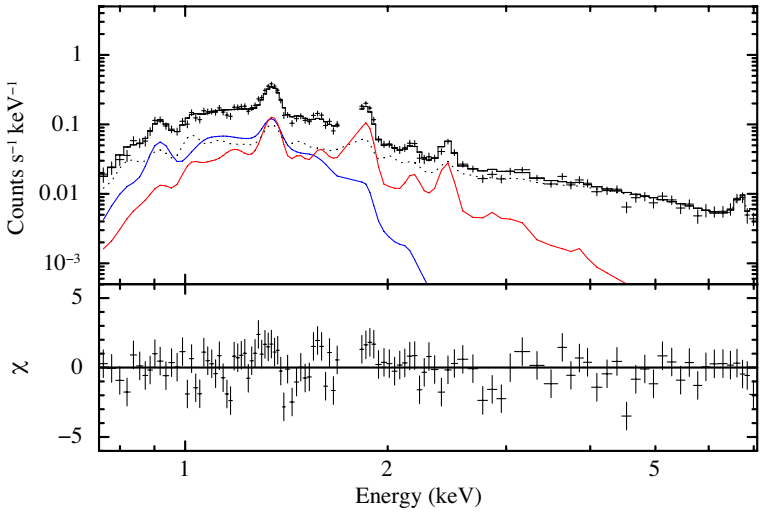

Figure 5.10: Spectrum of the outer ring of Kes 79 (black crosses) with the best-fit models (solid lines) and the residuals (lower panel). For clarity, only the merged FI spectrum is displayed. The dotted line shows the background model. The dashed line is the NEI plasma. The red line indicates the best-fit additional CIE plasma model.

5.3 Discussion

5.3.1 Abundances and Typing of the SNR

We have shown that the X-ray spectrum of Kes 79 is best described by two components: a CIE plasma and a multi-temperature NEI plasma. Since the CIE plasma has solar abundance, while the NEI counterpart is non-solar, the former is most naturally interpreted as interstellar medium (ISM) shocked by the SNR blast wave. The larger extension of the CIE plasma toward the outer radio shell also supports that the CIE plasma is blast wave shocked ISM plasma. The latter (NEI) would be then an ejecta heated up by the reverse shock. Figure 5.11 shows the comparison of the overall ejecta abundance pattern of Kes 79 with available explosive nucleosynthesis models of Type Ia (CDD1: Iwamoto et al. 1999) and CC supernovae (CC-SN) (Woosley & Weaver 1995). The measured abundance pattern broadly agrees with the ∼30–40 $M_\odot$ CC-SN models. Assuming that the ejecta of Kes 79 has a roughly spherical shape with a 5 arcmin radius and distance (D) of 7 kpc, the X-ray emitting volume (V) is $1.3 \times 10^{59}\ d_7^3 f^{0.5}$ cm^3, where f is the filling factor. From the normalization of the NEI emission component ($n_e n_H V/4\pi D^2 = 3.8 \pm 0.6 \times 10^{12}$ cm^{-5}), the total ejecta mass is estimated to be $\sim 60\ f^{0.5}\ d_7^{5/2}\ M_\odot$. This mass estimation is based on a H-dominated plasma. Using He, C

Table 5.3: Fitting parameters of low temperature plasma*.

Component	Parameter	
Absorption	$N_{\rm H}$ (10^{22} cm^{-2})	$1.66^{+0.08}_{-0.06}$
CIE	kT (keV)	0.17 ± 0.02
	Abundance (solar)	1 (fix)
	$EM^{\dagger}$ (10^{12} cm^{-5})	30^{+40}_{-10}
NEI	$EM^{\dagger}$ (10^{12} cm^{-5})	0.31±0.02
	χ^2 / d.o.f	324.69/304

* The uncertainties are the 90% confidence range.
*$\int n_{\rm e} n_{\rm p} {\rm d}V/4\pi D^2$, where $n_{\rm e}$, $n_{\rm p}$, D and V are the electron and proton number densities (cm^{-3}), the distance to the SNR (cm) and emission volume (cm^3), respectively.

and O abundances from ejecta models of ∼30–40 M$_\odot$ progenitor stars, the total ejecta mass is re-estimated to be $\sim 30\ f^{0.5}\ d_7^{5/2}\ M_\odot$. These are reasonably consistent with a ∼30–40 M$_\odot$ progenitor star, taking account of the distance ambiguity.

The NEI (ejecta) plasma has a temperature structure such that lighter elements are colder than the heavier elements. This trend is found in young Ia SNRs with onion-like structure, where the heavier elements are concentrated in the inner regions, while lighter elements are in the outer layers. As is shown in Section 5.2.4, Kes 79 has no onion-like structure; heavier elements are rather depleted in the central core. Therefore the observed temperature structure of this CC-SNR may be indicative of some mechanism other than that of onion-like Type Ia structure origin. One possibility is that the heavier elements attained higher ion temperature just after shock heating. If the time scale of energy transfer from ion to electron is comparable or longer than the ejecta plasma age, the electrons around the heavier elements can be at higher temperature than those around the lighter elements. To justify this idea, we need detail simulations of shock heating and preceding energy transfer process from ions to electrons, which is beyond the scope of this paper.

5.3.2 X-ray Emission from the Outer Radio Ring

Our work reveals that X-rays are extended to the outer ring of 5′–8′ to beyond what was previously known. The X-ray radial profile indicates the outer X-rays are associated with the outer radio shell. In the outer ring, the surface brightness of the CIE (ISM) relative to NEI(ejecta) is larger than that of the inner ring and center core. Assuming the emitting

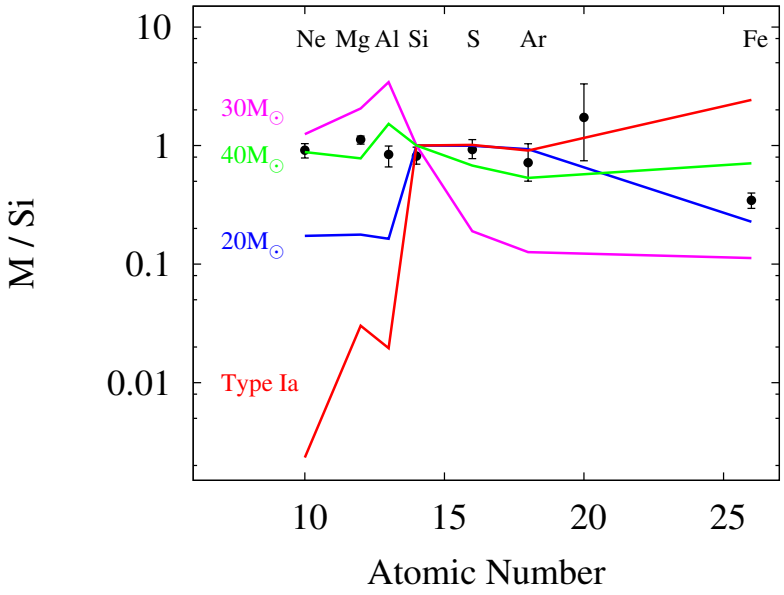

Figure 5.11: The best-fit metal abundance pattern of the Kes 79 ejecta relative to Si as a function of atomic number. The red line shows the pattern of a Type Ia SN model (CDD1: Iwamoto et al. 1999). The blue, magenta and green lines are Type II CC-SN models with progenitor masses of 20 $M_\odot$, 30 $M_\odot$ and 40 $M_\odot$ (S40C), respectively (Woosley & Weaver 1995).

volume of CIE to be a sphere, the inner and outer regions have a similar density $n_{\rm H}(\sim 1.0\ {\rm cm}^{-3})$ according to projection effect. The temperature of the CIE is also the same as that in the main X-ray emitting regions. Thus the ISM plasma is uniformly distributed in the whole SNR in terms of density and temperature.

For the angular size of $R = 8$ arcmin, the radius of the outer ring is 16 pc, and the volume of the plasma is 5.4×10^{59} cm^3. The best-fit ISM temperature of $kT_{\rm e} \sim 0.2$ keV gives the expansion speed of $V_{\rm s} = 3 \times 10^7$ cm s^{-1} from the strong shock relation assuming electron-ion temperature equilibration, $kT_{\rm e} = 3/16 \mu m_{\rm H} V_s^2$, where μ and $m_{\rm H}$ are the mean atomic mass and the mass of a hydrogen atom, respectively. Taking into account the velocity decrease in time (t) of $t^{-0.6}$, the dynamical age is estimated to be $\sim 2.7 \times 10^4$ years from the Sedov self-similar solution (Sedov 1959). Thus Kes79 is an old-intermediate aged SNR.

Chapter 6

SNR Kes 78 and W44

6.1 Overview of Kes 78

Kesteven 78 (or G32.8−0.1, hereafter Kes 78) is a Galactic SNR discovered by Caswell et al. (1975) based on the analysis of 408 MHz and 5000 MHz radio continuum surveys. Kes 78 has a partially brightened radio shell with a spectral index of −0.5 (Kassim 1992). The size of the radio shell is $20' \times 10'$ in diameter. The filamentary optical emission which possibly arises from a shock heated gas is also detected (Boumis et al. 2009). The distance of Kes 78 is estimated as ∼4.8 kpc by an H I absorption and association of molecular clouds and the age is calculated as $\sim 1.2 \times 10^5$ yr by using H I observation (Gosachinskii and Khersonskii 1985).

The shock wave of Kes 78 is strongly interacting with surrounding molecular clouds. An 1720 MHz OH maser is detected by the VLA observation at the eastern edge of the shell (Koralesky et al. 1998) . Since the ^{12}CO observation reveals that Kes 78 is expanding in the CO cavity (Zhou and Chen 2011), a progenitor star of Kes 78 possibly blew off its mass through the stellar winds. GeV counterpart of Kes 78 was detected by Fermi and also TeV gamma-rays were observed from the eastern edge (HESS J1852−000; Kosack et al. 2011).

X-ray emission is detected at the north-eastern edge (Zhou and Chen 2011). The X-ray spectrum was fitted by the ionizing plasma model with the temperature of ∼1.5 keV. However, an observation of the overall shell was not performed so far and a thermal emission feature has not been unveiled due to severe contamination of the GRXE. Suzaku observed the overall shell of Kes 78 to determine the detailed plasma parameters taking advantage of the low background for a diffuse source. We analyze spectra by using the background model compiled in Section 4.2.2 (BG1).

6.2 Analysis and Results of Kes 78

6.2.1 X-ray Image

Figure 6.1 shows XIS images in the energy bands of 0.7–1.5 keV and 2.0–3.0 keV. Here the X-ray events of XIS 0, 1 and 3 are combined, with corrections for the vignetting effect and subtraction of the NXB.

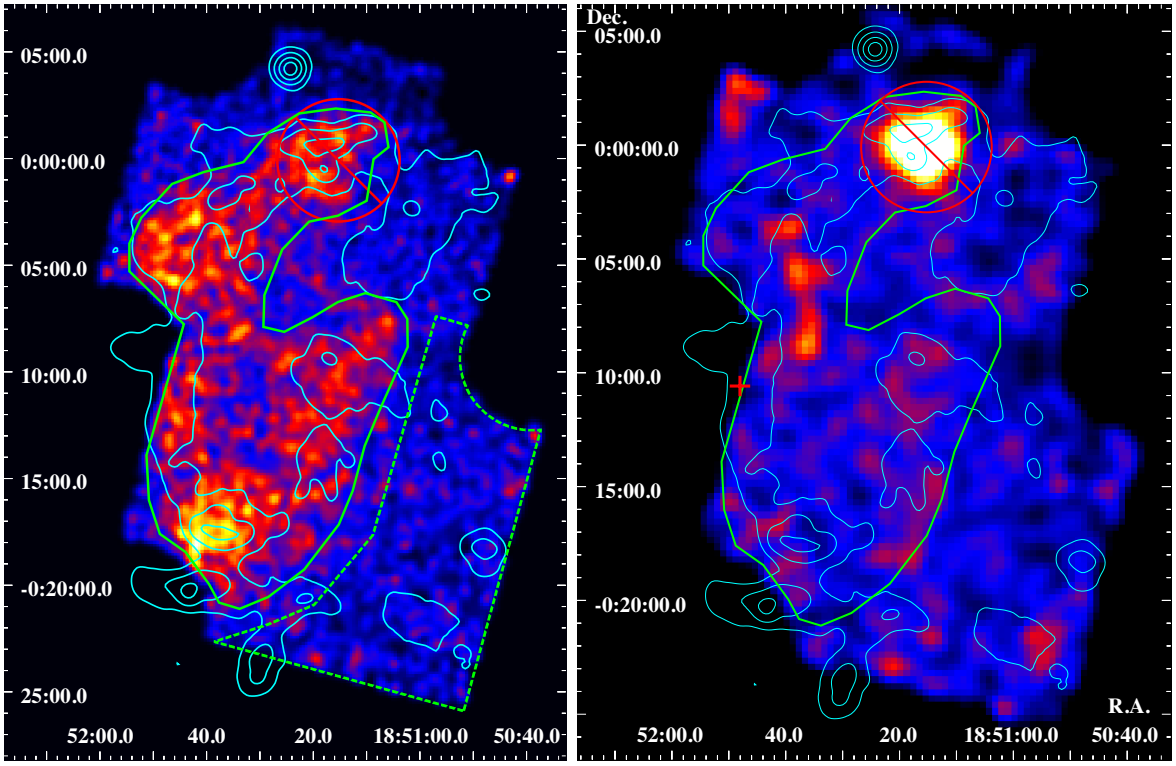

Figure 6.1: NXB-subtracted XIS images of Kes 78 after correcting for the vignetting effect in units of photons keV^{-1} cm^{-2} s^{-1}. The energy bands are 0.7–1.5 keV (left) and 2.0–3.0 keV (right). The cyan contours indicate the flux map of the 1.4 GHz emission (Condon et al. 1998). The green solid and dashed lines show a source and background region. The red cross is a position of the 1720 MHz OH maser (Koralesky et al. 1998). The red circle is a region of the irrelevant X-ray burster which is excluded from an analysis of the SNR.

An X-ray shell-like structure which has never been reported before clearly appears on benefit of the low background of the XIS. The X-ray shell roughly associates with the incomplete radio shell. On the other hand, the hard band image indicates a very hard point-like source at the north edge of the SNR. Since we can also see hard X-ray diffuse emission near the OH maser spot as the red cross in Figure 6.1 right, an additional emission component seems present in an X-ray spectrum of Kes 78 together with the thermal emission from the shell.

6.2.2 X-ray Feature of the Hard X-ray Point Source

We analyze the hard X-ray point source on the north edge to investigate an X-ray feature. Firstly, we take the time variability of the point source. We show time profiles of photon count rate in the energy range of 0.8–1.5 keV and 2.0–6.0 keV in Figure 6.2.

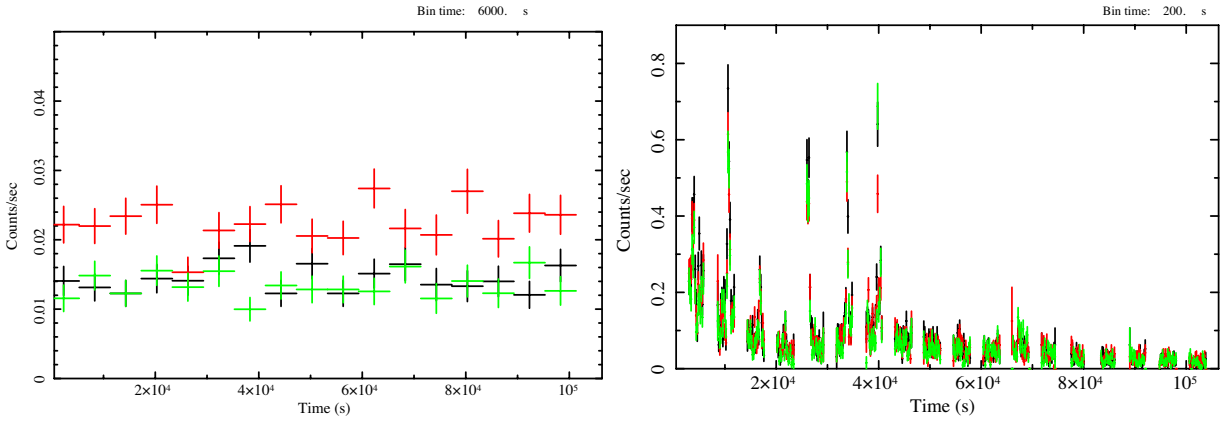

Figure 6.2: The photon count rate of the point source in the energy range of 0.8–1.5 keV (left) and 2.0–6.0 keV (right). The black, red and green crosses show the photon count rate of XIS 0, 1 and 3, respectively.

The hard energy band (2.0–6.0 keV) shows the drastic time variability compared to the soft energy band (0.8–1.5 keV). Since the soft energy band is stable, it probably indicates soft X-rays mostly emitted from the SNR. Figure. 6.3 shows the expanded version of the first peak in the hard band. It clearly shows a triple peak which is often observed from an X-ray burster (4U 1636−53; Van Paradijs et al. 1986) and hence we speculate that this object belongs to a class of X-ray binary system.

Secondly, we analyze a spectrum of the point source. The spectrum of the point source shows a feature-less very hard emission and soft plasma emission as shown in Figure 6.4. We use a compound model consisting of the phenomenological plasma model (the thermal bremsstrahlung and multi-Gaussian lines) and absorbed powerlaw. We obtain the acceptable fit with χ^2/ d.o.f of 372.08/387 $\sim$ 0.99. The best-fit spectrum and parameters are shown in Figure 6.4 and Table 6.1, respectively. Since the absorption of the powerlaw component is very high, this result also favors that the point source is the X-ray burster whose companion is a massive star surrounded by dense materials.

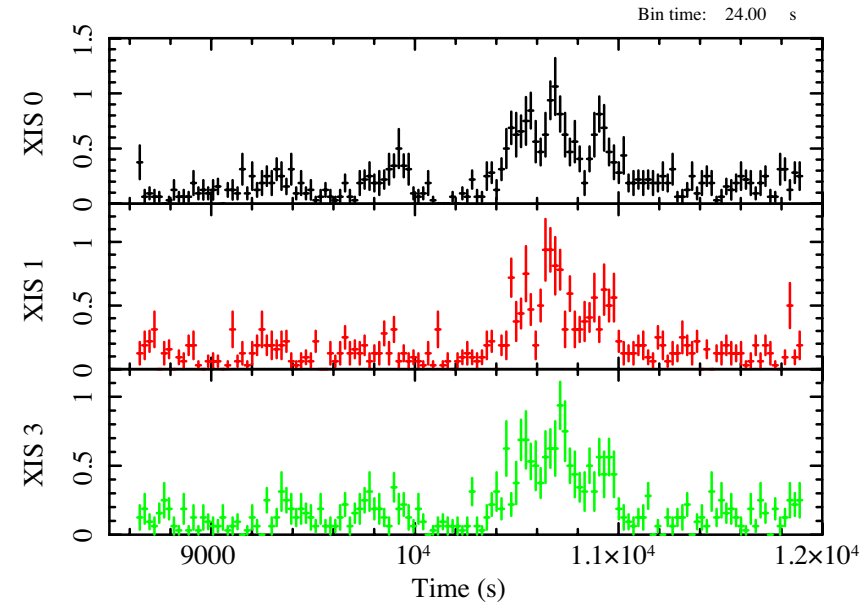

Figure 6.3: The 2.0–6.0 keV photon count rate of the first peak seen in Figure 6.2 in the finer time resolution (24 s). The black, red and green crosses show the photon count rate of XIS 0, 1 and 3, respectively.

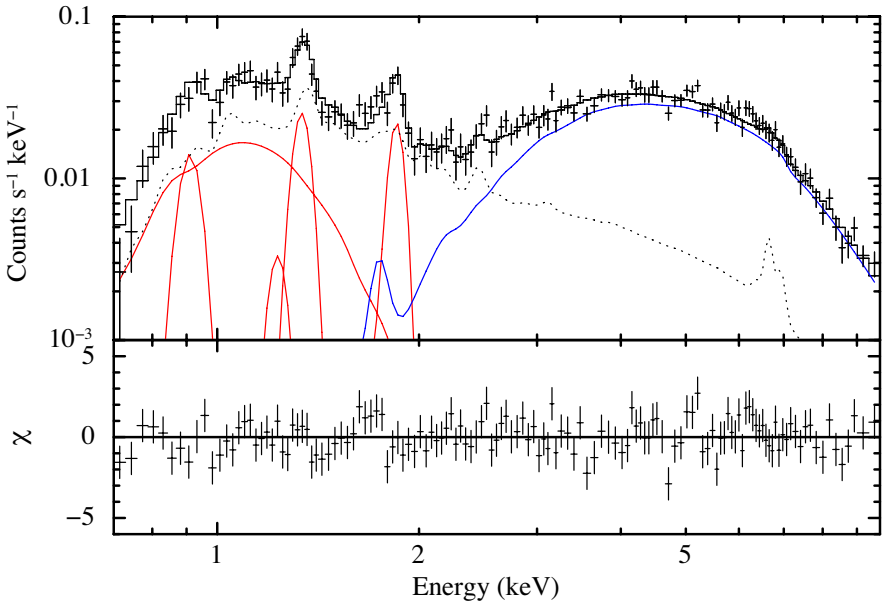

Figure 6.4: The best-fit spectrum and its residuals for the X-ray burster. The phenomenological plasma and powerlaw components are shown by the red and blue lines, respectively. The dotted line indicates the background model. For clarity, only the merged FI spectrum is plotted.

Table 6.1: Best-fit parameters of the X-ray burster*.

Parameter	bremsstrahlung	
$N_{\rm H;pheno}$ (10^{22} cm^{-2})	$0.9^{+0.2}_{-0.4}$	
$kT_{\rm b}$ (keV)	$0.18^{+0.11}_{-0.06}$	
$EM^{\dagger}$ (10^{12}cm^{-5})	8^{+30}_{-7}	
Emission line	energy (keV)	intensity‡
Ne IV Kα	0.889±0.013	15^{+57}_{-11}
Ne X Lyβ	1.211	$0.3^{+0.6}_{-0.3}$
Mg XI Kα	1.32±0.01	$1.8^{+1.3}_{-0.4}$
Si XIII Kα	$1.840^{+0.006}_{-0.003}$	$1.0^{+0.3}_{-0.2}$
	powerlaw	
$N_{\rm H;PL}$ (10^{22} cm^{-2})	$10.1^{+0.9}_{-0.7}$	
photon index	1.81±0.13	
flux (photons 10^{-4} cm^{-2} s^{-1})	$1.3^{+0.4}_{-0.3}$ (5–8 keV)	
χ^2/d.o.f	372.08/387	

* The uncertainties are the 90% confidence range.

$^{\dagger}n_{\rm e}n_{\rm p}V/4\pi D^2$,where $n_{\rm e}$, $n_{\rm p}$, D and V are the electron and proton number densities (cm^{-3}),the distance (cm) and the emission volume (cm^3), respectively.

‡ The units are 10^{-5} photons cm^{-2} s^{-1}.

6.2.3 The Model Fit to the Overall Spectrum of Kes 78

The spectrum of Kes 78 is extracted from the X-ray shell shown as the green line in Figure 6.1 after excluding the point source. After subtracting the NXB, we fit the overall spectrum to a thermal plasma model adding the GRXE model estimated in Section 4.2.2. Since we can not neglect the contamination events from the point source, we add the absorbed powerlaw model obtained in subsection 6.2.2 with the simulated leakage flux (Ishisaki et al. 2007). To fit the overall spectrum, we use the APEC model as a plasma in CIE. The abundances of Ne, Mg, Si and Fe are free parameters while those of other elements are fixed to 1 in units of solar value. Since this model dose not include the Fe-L complex, we add a Gaussian line with energy of $\sim$ 1.2 keV. However, this model is rejected with a large χ^2/d.o.f = 646.84/418 $\sim$ 1.55.

The residuals show hard X-ray excess emission above $\sim$3 keV. This is consistent with the hard X-ray image (Figure. 6.1 right). Therefore, we add a powerlaw model to represent the hard X-ray emission. Then the fit is improved as χ^2/ d.o.f value of 473.21/416 $\sim$ 1.14. Since we can not obtain significant improvement by adding another component, we adopt this 'APEC+powerlaw' model as the best approximation for the overall spectrum of Kes 78. The best-fit spectrum and parameters are shown in Figure 6.5 and Table 6.2.

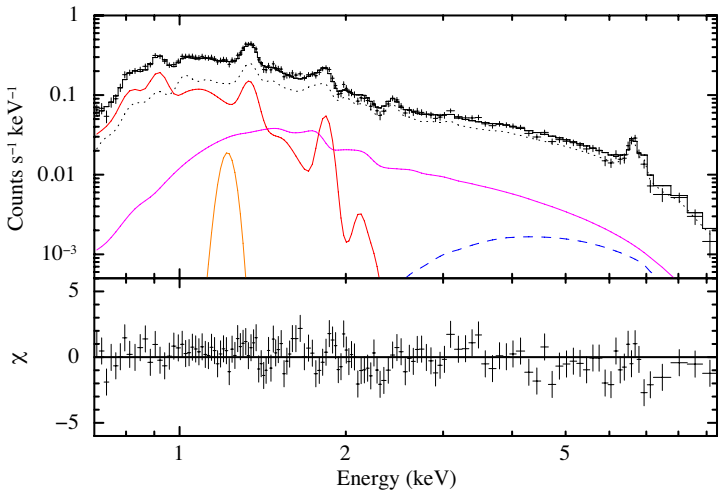

Figure 6.5: The best-fit spectrum extracted from the X-ray shell region of Kes 78. The APEC, powerlaw and $\sim$1.2 keV Gaussian components are shown by the red, magenta and orange lines. The dotted line is the GRXE component. The blue dashed line shows the contamination from the X-ray burster. For clarity, only the merged FI spectrum is plotted.

Table 6.2: Best-fit parameters of Kes 78*.

	APEC	APEC+powerlaw
$N_{\rm H}(10^{22}{\rm cm}^{-2})$	0.63 ± 0.09	$0.94^{+0.09}_{-0.05}$
	APEC	
kT (keV)	0.28 ± 0.02	$0.16^{+0.08}_{-0.02}$
Ne	$0.42^{+0.13}_{-0.09}$	$1.0^{+0.4}_{-0.3}$
Mg	$0.5^{+0.2}_{-0.5}$	$2.1^{+1.7}_{-0.6}$
Si	$2.0^{+0.8}_{-0.5}$	22^{+45}_{-15}
Fe	$0.06^{+0.14}_{-0.06}$	5^{+17}_{-3}
$EM^{\dagger}$ (10^{12} cm^{-5})	$1.2^{+0.4}_{-0.3}$	10 ± 9
	powerlaw	
photon index	–	$2.6^{+0.3}_{-0.2}$
flux (10^{-4} photons cm^{-2} s^{-1})	–	$1.0^{+0.3}_{-0.2}$ (2.3–5 keV)
χ^2/d.o.f.	646.84/418	473.21/416

* The uncertainties are the 90% confidence range.

$^{\dagger}n_{\rm e}n_{\rm p}V/4\pi D^2$,where $n_{\rm e}$, $n_{\rm p}$, D and V are the electron and proton number densities (cm^{-3}),the distance (cm) and the emission volume (cm^3), respectively.

6.2.4 Spatial and Spectral Analysis of the 6.4 keV Line

In order to investigate the 6.4 keV excess emission, we make an X-ray image in the energy range of 6.2–6.5 keV. Figure 6.6 shows the 6.2–6.5 keV image after subtracting the NXB. The XIS 1 image is not included because of the poor signal-to-noise ratio around the 6.4 keV.

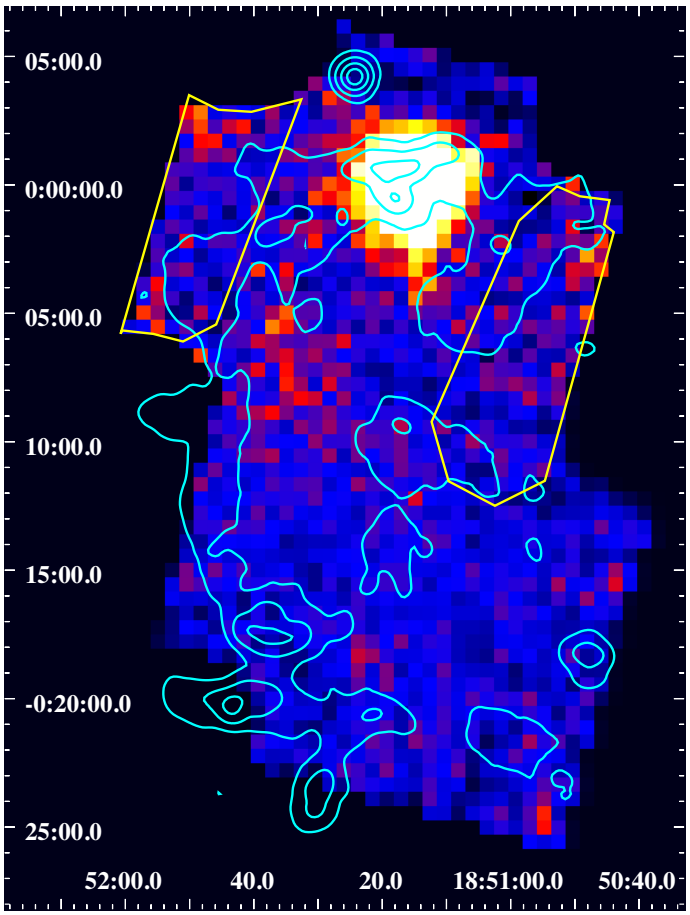

Figure 6.6: The NXB-subtracted XIS 0+3 image of Kes 78 in the energy band of 6.2–6.5 keV after correction for vignetting in units of photons keV^{-1} cm^{-2} s^{-1}. The cyan contours indicate the flux map of the 1.4 GHz emission (Condon et al. 1998). The yellow line shows the extracted region.

We can see the possible excess emission at $\sim$ 6.4 keV around the north shell in Figure 6.6. The diffuse hard X-ray emission seen in Figure 6.1 is associated with the excess emission inside the shell at the point of (18:51:40.0, -0:0.5:00.0). Since we can not detect any significant emission of 6.4 keV inside the shell, we extract an X-ray spectrum from the outside region excluding the hard X-ray diffuse emission. Then, we extracted the data from both the outside and BG1 region in the energy range 5.0–10 keV. Since the SNR thermal emission can be completely neglected above 5.0 keV, we can easily handle with the spectra to search the enhancement of

the 6.4 keV emission. We apply the phenomenological GRXE model (Uchiyama et al. 2013) which consists of a powerlaw and three Gaussian lines; Fe I Kα (6.4 keV), Fe (6.68 keV) and Fe (6.97 keV). Then the outside and BG1 spectra are simultaneously fit with the phenomenological model, where the fitting model of the outside spectrum adds to another $\sim$6.4 keV Gaussian line and simulated contamination spectra from the X-ray burster. The best-fit spectra are shown in Figure 6.7. The best-fit flux of the additional 6.4 keV line in the outside region is $(6.6 \pm 4.0) \times 10^{-6}$ photons cm^{-3} s^{-1}. The 6.4 keV emission of BG1 is $(0.8^{+2.4}_{-0.8}) \times 10^{-6}$ photons cm^{-3} s^{-1}. The maximum uncertainty from background subtraction is less than $\sim$ 10% or $\sim 0.3 \times 10^{-6}$ photons cm^{-3} s^{-1}. This is only $\sim$5% level of the excess emission. Then we perform the F-test and obtain the p-value as 1.3%. We found that the significance level of the additional 6.4 keV line is 2.2σ, thus this is the marginal result.

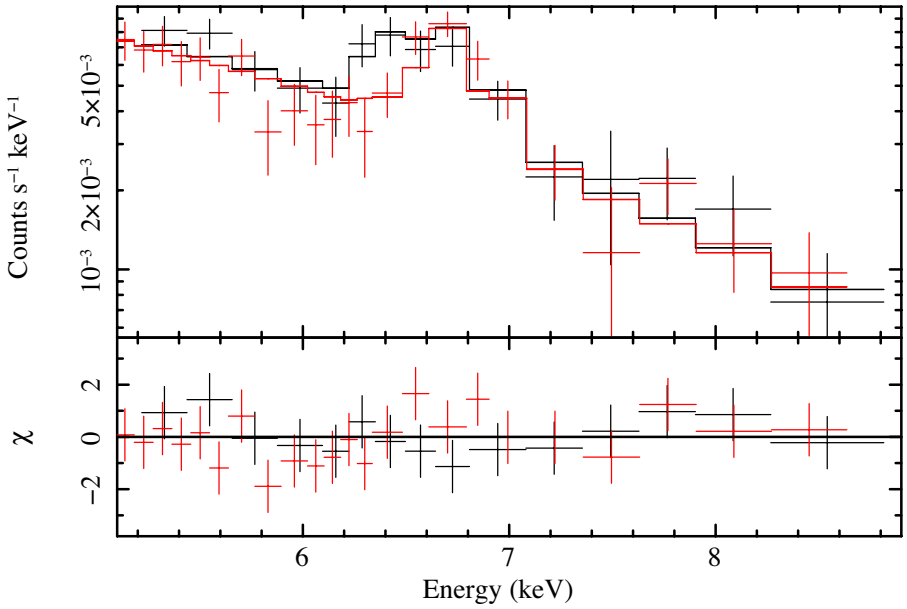

Figure 6.7: The best-fit spectra extracted from the outside (black) and BG1 (red) regions.

6.3 Overview of W44

W44 (also known as G34.7−0.4 or 3C 392) is a Galactic SNR with a elliptical radio shell of non-thermal synchrotron emission (Kundu and Velusamy 1972). The age and distance are estimated $\sim$ 20000 yr (Wolszczan et al. 1991) and $\sim$ 3 kpc (Claussen et al. 1997), respectively. 1720 MHz OH maser emission is also discovered, which indicates the interaction of molecular clouds (Claussen et al. 1997). Seta et al. (2004) performed a high-resolution mapping of molecular environment using ^{12}CO emission with Nobeyama 45-m radio telescope and reported a lot of evidences of shock-molecular interactions including cloud evaporation.

The strong GeV gamma-ray emission is detected from W44 by Fermi and AGILE (Abdo et al. 2010 and Cardillo et al. 2014). In W44, the GeV gamma-ray with photon index of $\sim$ 3 has good correlation with the radio shell . W44 is confirmed as a CR proton accelerator. The gamma-ray spectrum of W44 has a cutoff around $\sim$200 MeV, which provides clear evidence of the pion-decay origin (Ackermann et al. 2013).

Center-filled X-ray emission from W44 was first discovered by ROSAT (Rho et al. 1994). W44 is the typical core-collapse MM-SNR with the radio shell and center-filled X-ray. Suzaku observation of W44 previously reported a detection of the RRCs of highly ionized atoms (Uchida et al. 2012). While the electron temperature of W44 is about 0.5 keV, the arc-like feature of hard X-ray emission was also detected. However, since Uchida et al. (2012) analyzed Suzaku data only below 6 keV, the Fe Kα emission has not yet been investigated. Figure 6.8 shows an XIS image in the energy bands of 0.8–3.0 keV. Here the X-ray events of XIS 0, 1 and 3 are combined, with corrections for the vignetting effect and subtraction of the NXB. We can clearly see the center-filled X-ray inside the radio shell.

6.4 Analysis and Results of W44

6.4.1 Background Estimation and Hard X-ray Sources

Figure 6.9 shows an XIS image in the energy range from 6.2 keV to 6.5 keV excluding XIS 1, with corrections for the vignetting effect and subtraction of the NXB. To determine the local background level of 6.4 keV, we define the reference region which shows relatively low 6.4 keV emission indicated by green dashed line in Figure 6.9. There are two bright sources as shown by red (Source 1) and yellow (Source 2) ellipses in Figure 6.9. The magenta cross is the position of a pulsar, PSR B1853+01 (Wolszczan et al. 1991).

We examine the 6.4 keV excess emission of W44 by the phenomenological model. We then simultaneously fit the phenomenological model to spectra extracted from Source 1, 2 and the reference spectrum. We use the energy range from 5 to 10 keV to avoid the SNR thermal

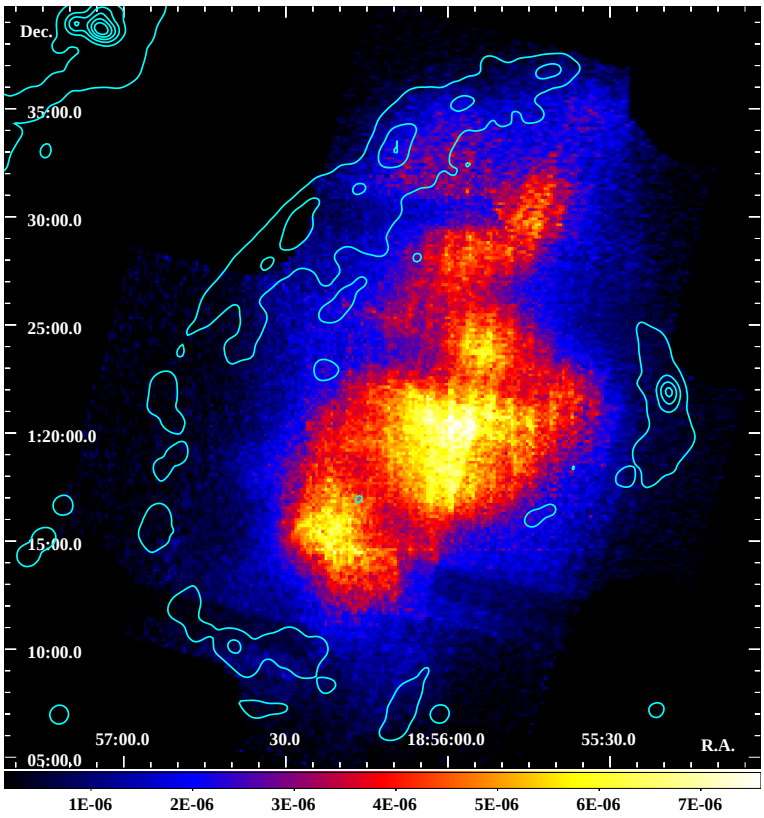

Figure 6.8: NXB-subtracted XIS image (0.8–3.0 keV) after correcting for vignetting and exposure time in units of photons s^{-1} keV^{-1} cm^{-2}. The cyan lines indicate the flux contour of the 1.4 GHz emission (Condon et al. 1998).

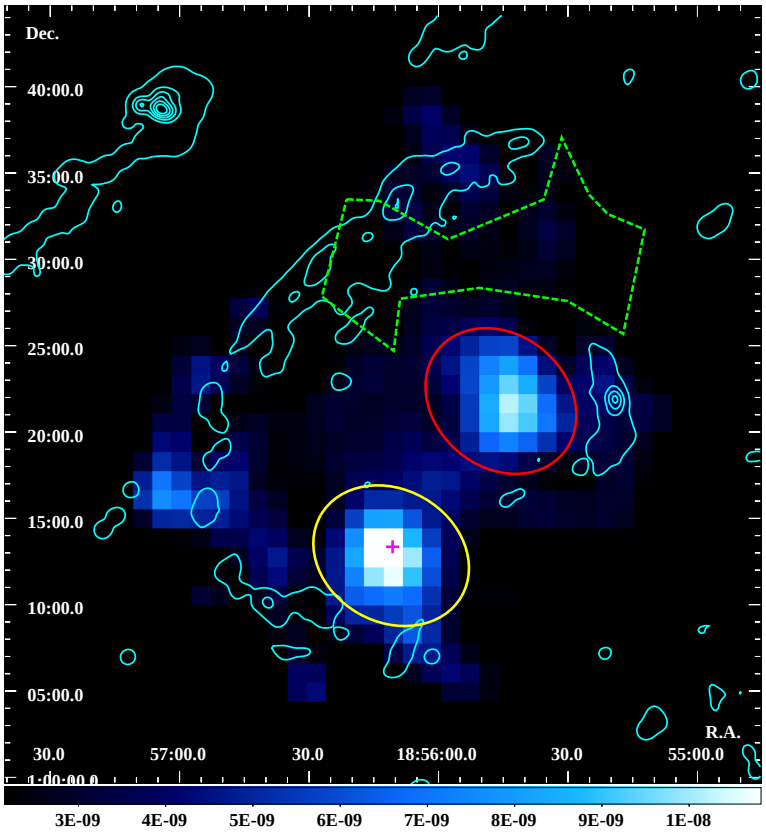

Figure 6.9: NXB-subtracted image (6.2–6.5 keV) after correcting for vignetting and exposure time in units of photons s^{-1} keV^{-1} cm^{-2}. The cyan contours indicate the flux map of the 1.4 GHz emission (Condon et al. 1998). The red, yellow and dashed green lines show Source 1, Source 2 and the reference regions, respectively. The magenta cross is the position of PSR B1853+01 (Wolszczan et al. 1993).

emission in following analyses. We add a powerlaw component to two sources to represent the hard X-ray excess emissions and one Gaussian line at $\sim$ 6.15 keV to Source 1. The best-fit spectra and parameters are shown in Figure 6.10 and Table 6.3, respectively. These two point sources show no evidences of 6.4 keV.

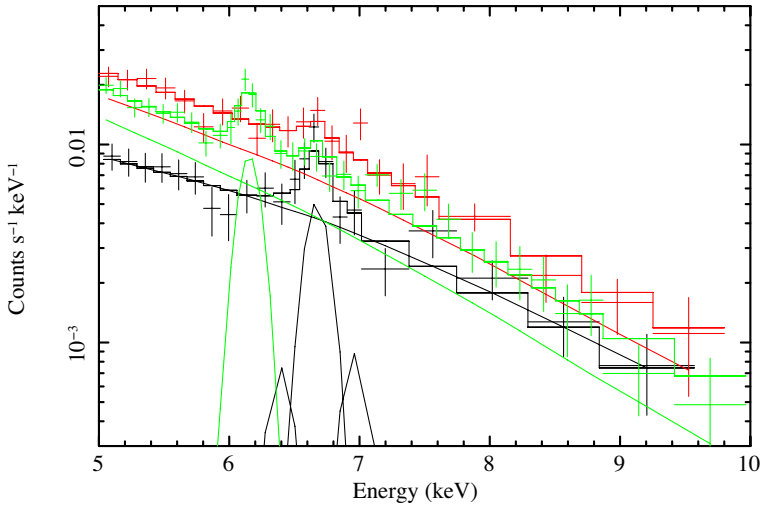

Figure 6.10: X-ray spectra of Source 1 (green), Source 2 (red) and the reference region (black). Only a merged spectrum of FI CCDs are shown for visibility. Each solid line indicates sum of model components.

6.4.2 Spatial and Spectral Analysis of the 6.4 keV Line

In order to investigate the spatial distribution of the excess emission around 6.4 keV, we make a map 6.2–6.5 keV relative to 5.9–6.2 keV shown in Figure 6.11 left. Here, count ratio between the two bands is need to see the excess around 6.4 keV. We find possible spatial association with the 6.4 keV excess and GeV gamma-ray emission shown in Figure 6.11 right (taken from Abdo et al. (2010)). We merge spectra extracted from three regions indicated as green lines in Figure 6.11. Then, we fit the phenomenological model to the extracted spectra and compare it with the reference spectrum shown in Figure fig:W44 comp spec.

The best-fit flux of the additional 6.4 keV line of W44 is $(7.0 \pm 5.0) \times 10^{-6}$ photons cm^{-3} s^{-1}. The 6.4 keV emission of the reference region is $(2.6^{+3.9}_{-2.6}) \times 10^{-6}$ photons cm^{-3} s^{-1}. The maximum uncertainty from background subtraction is less than $\sim$ 10% or $\sim 0.7 \times 10^{-6}$ photons cm^{-3} s^{-1}. This is only $\sim$10% level of the excess emission. Then we perform the F-test and obtain the p-value as 2%. We found that the significance level of the additional 6.4 keV line is 2.1σ, thus this is the marginal result.

Table 6.3: Parameters of the phenomenological model*.

	Reference	
Powerlaw	index	$1.7^{+0.7}_{-0.6}$
	flux (10^{-4} cm^{-2} s^{-1})	$0.9^{+2.0}_{-0.5}$ (5–8 keV)
Emission line†	6.40 keV (Fe I Kα)	$1.1^{+2.1}_{-1.1}$
	6.68 keV (Fe XX Kα)	7.4 ± 2.3
	6.97 keV (Fe XXI Lyα)	$1.5^{+2.3}_{-1.5}$
	Source 1	
Powerlaw	index	$3.3^{+0.8}_{-0.7}$
	flux (10^{-4} cm^{-2} s^{-1})	$0.8^{+2.2}_{-0.6}$ (5–8 keV)
Emission line†	6.13–6.19 keV	9.2 ± 2.6
	Source 2	
Powerlaw	index	$2.7^{+0.7}_{-0.6}$
	flux (10^{-4} cm^{-2} s^{-1})	$1.2^{+2.6}_{-0.8}$
χ^2/d.o.f.	44.65/68	

* The uncertainties are the 90% confidence range.

† The units are 10^{-6} photons cm^{-2} s^{-1}.

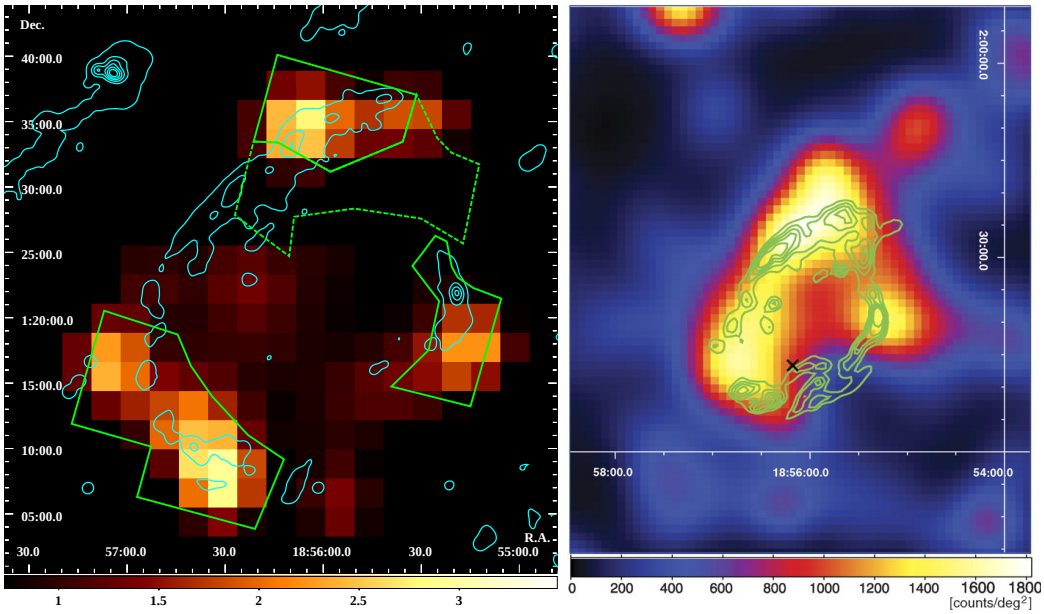

Figure 6.11: Left: NXB-subtracted image (6.2–6.5 keV) after correcting for vignetting and exposure time in units of photons s^{-1} keV^{-1} cm^{-2}. The green lines shows the source regions. Right: The count map image of GeV gamma-rays (2–10 GeV) observed with Fermi LAT. This figure is taken from Abdo et al. (2010).

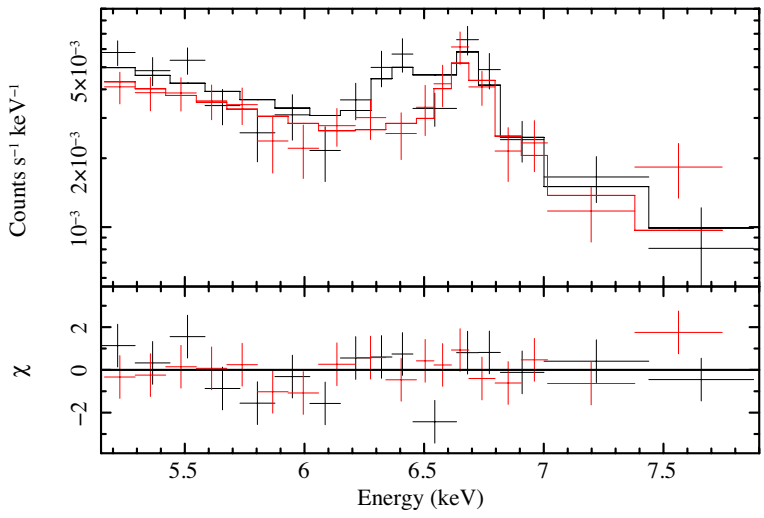

Figure 6.12: X-ray spectra of the sources summed over the three regions (black; see Figure 6.11 left) and the reference region (red). Only a merged spectrum of FI CCDs are shown for visibility.

6.5 Discussion

We obtain hints of the 6.4 keV enhancement from both Kes 78 and W44 with significance level of 2.1σ–2.2σ. Although the observations did not cover the all of molecular clouds interacting with Kes 78, the extracted outside region partially associates with the dense molecular bubble-like structure possibly related to Kes 78 (Zhou and Chen 2011). The possible 6.4 keV emission of W44 is also associated with the GeV gamma-ray emission and molecular clouds (Abdo et al. 2010, Seta et al. 2004).

6.5.1 Abundances and Typing of Kes 78

The obtained X-ray spectrum of Kes 78 is described by the CIE+powerlaw model. Since the abundances of the CIE plasma are far from 1 solar value, the origin of this CIE plasma would be the supernova ejecta. Figure 6.13 shows the abundance of the CIE relative to Ne, together with the nucleosynthesis models (Iwamoto et al. 1999, Woosley & Weaver 1995). The abundance pattern indicates the CC-SN model with a progenitor mass of $\sim 20\ M_{\odot}$. If we assume that the ejecta of Kes 78 has a cylindrical shape whose diameter of $10'$ and length of $20'$ (see Figure 6.1 left) with the distance (D) of 4.8 kpc, the X-ray emitting volume (V) is $5 \times 10^{59}\ d_{4.8}^{3} f^{0.5}$ cm^3, where f is the filling factor. Using He, C and O abundances from ejecta models of 20 $M_{\odot}$ progenitor stars, the total ejecta mass is re-estimated to be $\sim 25\ f^{0.5}\ d_{4.8}^{5/2}\ M_{\odot}$. Since the filling factor is low as shown in Figure 6.6 left, these are reasonably consistent with a $\sim$20 $M_{\odot}$ progenitor star. This value is the roughly same as 22 $M_{\odot}$ estimated by the size of molecular wind bubble structure (Zhou & Chen 2011).

6.5.2 Detection of Non-thermal Sources

Kes 78

We have shown that the X-ray shell structure of Kes 78 associates with the radio shell. We discover the diffuse hard X-ray source around the OH maser which indicates the shock wave strongly interacting with the molecular clouds. The powerlaw component of the Kes 78 spectrum is probably emitted in this region. The possible origin is synchrotron emission from high energy electrons due to a lack of the 6.4 keV emission. The association of TeV gamma-ray emission supports the high energy electron origin (Kosack et al. 2011), because the high energy electrons emit TeV gamma-rays through the inverse Compton scattering off CMB photons (e.g. Aharonian et al. 2007).

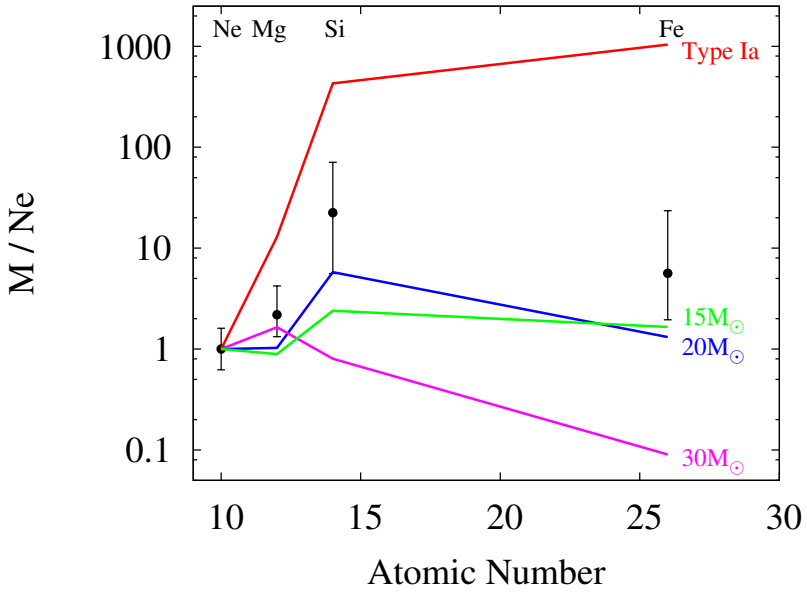

Figure 6.13: Best-fitting metal abundances of Kes 78 relative to Ne abundance as a function of atomic number. The red line shows the Type Ia SN model (CDD1: Iwamoto et al. 1999). The green, blue and magenta lines represent CC-SN models with progenitor masses of 15 $M_{\odot}$, 20 $M_{\odot}$ and 30 $M_{\odot}$, respectively (Woosley & Weaver 1995).

W44

We discover the two hard X-ray point sources inside of W44. Since the spectrum extracted from the southern point-like source (Source 2) is fitted with a single power law function with a power law index of $2.7^{+0.7}_{-0.6}$. According to Petre et al. (2002), the source is identified with a pulsar wind nebula which could accelerate electrons to high energy. The feature-less power law and its spectra index is consistent with the synchrotron emission from high energy electrons. The north one has the 6.13–6.19 keV emission line. We can interpret this line as the redshifted Fe Kα line (6.4 keV) from the extra galaxy. If it is really redshifted 6.4 keV line, the redshift of this source is calculated to be $z \sim 0.034$–0.044, thus, this is an extragalactic source.

Chapter 7

The Origin of Fe Kα Line Emission

7.1 The Origin of Fe Kα Emission Unrelated to Cosmic-rays

7.1.1 Fe Kα emission induced by X-rays

The spacial association between the 6.4 keV emission region and location of a molecular cloud (see Figure 5.7) leads to the hypothesis that the 6.4 keV emission of Kes 79 is emitted from the interaction with a molecular cloud. The empirical relation between the mass and size of molecular clouds (Scovile et al. 1987) gives a mean density of hydrogen as 360 $(D/40 \text{ pc})^{-0.9}$ cm^{-3}. If we use the size of the cloud G33.91+0.11 which is associated with Kes 79 (Scovile et al. 1987), we obtain ~ 200 cm^{-3}. Thus, we use $n = 200$ cm^{-3} in following discussion.

When a molecular cloud absorbs X-rays with energy higher than 7.1 keV, the fluorescent line of 6.4 keV is emitted by the excitation of neutral irons (e.g. Basko 1980). A photon flux of the 6.4 keV line, F (photons s^{-1} cm^{-2}), is calculated by the following equation:

$$F = \epsilon \frac{\Omega}{4\pi} \int_{7.1 \text{ keV}}^{\infty} \left(1 - e^{-N_{\rm Fe}\sigma_{\rm Fe(E)}}\right) P(E) \, \mathrm{d}E, \tag{7.1}$$

where ϵ, Ω, $N_{\rm Fe}$, σ and $P(E)$ are the fluorescence yield of Fe, a solid angle of the molecular cloud from source, the column density of Fe, the cross section of Fe I Kα line excitation and a source spectrum model, respectively.

A transient hard X-ray source emitting X-rays above 7.1 keV was discovered at the south of Kes 79 on September 2008 (Zhou et al. 2014). The unabsorbed flux of this source is $\sim 5 \times 10^{-12}$ erg cm^{-2} s^{-1} in the energy range of 1–10 keV. Using the best-fit model (Resonant Cyclotron Scattering; Rea et al. 2008) with plasma temperature of ~ 0.71 keV as $P(E)$, we can calculate 0.03×10^{-6} cm^{-2} s^{-1} even if we assume that the solid angle of the molecular cloud from this source is 50% ($\Omega/4\pi = 0.5$). This value is smaller than the obtained 6.4 keV emission

of Kes 79 ($\sim 3.0 \times 10^{-6}$) by two orders of magnitude. Since no additional hard X-ray source has been reported around Kes 79, the X-ray inducing origin seems unreasonable.

7.1.2 Origin from the Hot Ejecta

A low ionized plasma can emit Fe Kα line around the energy of ∼6.4 keV (e.g. Yamaguchi et al. 2012). According to the result of the model A (Table 5.1), the abundance of Fe is 0.35 ± 0.05 ($\equiv x$). While the temperature of other elements is <1.0 keV (kT_1, kT_2), Fe plasma possibly distributes the isolated region at the direction to the molecular cloud and becomes thermalized up to 2.0 keV (kT_3) in recent years because of low $n_{\rm e}t$ shown in Table 5.1.

We estimate the emission mass of Fe by the calculated emission measure $EM(n_{\rm e}n_{\rm H}V) = (2.2 \pm 0.4) \times 10^{58}\ d_7^2$ cm^{-3} at 7 kpc. If we assume that the mass fraction of Fe is the solar value as 4.68×10^{-5} (Anders & Grevesse 1989), the density of Fe ($n_{\rm Fe}$) is expressed as

$$n_{\rm Fe} \sim 4.68 \times 10^{-5} x \sqrt{\frac{EM}{1.4\ V}}. \tag{7.2}$$

Using $m_{\rm Fe} = 9.27 \times 10^{-26}$ kg, we can obtain the total mass of emitting Fe:

$$M_{\rm Fe} = m_{\rm Fe}\ n_{\rm Fe} V \tag{7.3}$$

$$\sim 7.2 \times 10^{28}\ {\rm kg} \sim 0.04\ d_7^{2.5}\ M_\odot. \tag{7.4}$$

An expected total Fe mass is less than $\sim 5 \times 10^{-2}\ M_\odot$ according to the core-collapse nucleosynthesis model (Woosley & Weaver 1995). If the reverse shock reaches to the iron core of the ejecta, a small fraction of the iron could be partially ionized ($n_{\rm e}t$ ∼10^{-9}–10^{-10} s cm^{-3}) and generate line emission close to ∼ 6.4 keV. This ∼ 6.4 keV emission has been discovered in a young Type Ia SNR which is rich in Fe (RCW 86; Yamaguchi et al. 2012). The spatial distribution of the 6.4 keV line, no emission near the core region and enhanced emission toward the boundary of the SNR, is against the idea of the ejecta origin.

The progenitor of Kes 79 is the core-collapse supernova confirmed by the abundance pattern and the mass estimation. Figure 7.1 (Yamaguchi et al. 2014) shows the centroid energy of Fe Kα line. The centroid energies of the core-collapse SNRs are 6.6–6.7 keV, which is emitted by the highly ionized Fe. Yamaguchi et al. (2014) concluded that it probably suggests a crucial gap of ambient environment interacting with SNRs. This is strongly supported by a recent theoretical model by Patnaude et al. (2015). Again, this empirical law also does not favor the origin from the hot ejecta.

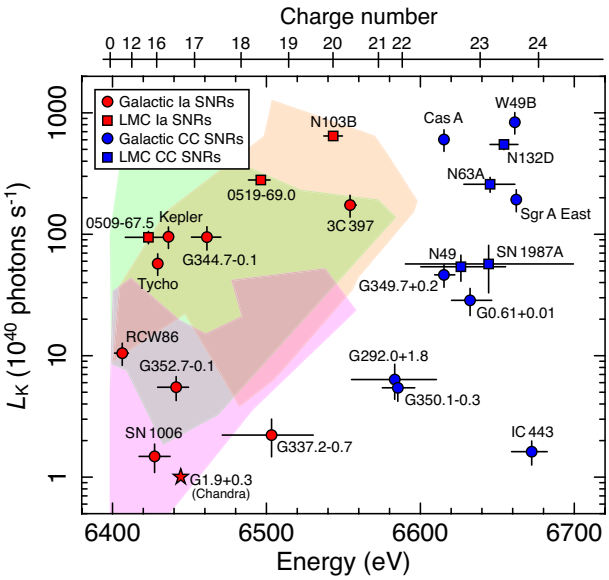

Figure 7.1: Centroid energies and line luminosities of Fe Kα emission from various SNRs. The corresponding effective charge number is also given at the top of this plot. Red and blue points represent the type Ia and core-collapse SNRs or their candidates, respectively. This figure is taken from Yamaguchi et al. (2014).

7.2 The 6.4 keV Emission Induced by Low Energy Cosmic-rays

The remaining possibility is the particle origin because the X-ray and hot plasma are unlikely the origin of 6.4 keV line. The neutral irons in molecular clouds ionized by particles excite the neutral Fe Kα line (6.4 keV). The possible main contributors are electrons and protons. If the origin is electrons, the strong Bremsstrahlung emission can be detected (see Section 2.4.1). According to figure 2.15, the equivalent width of the 6.4 keV line is around 0.2 keV in the case of electrons. The observed spectrum of Kes 79 only shows the strong 6.4 keV emission with the best-fit equivalent width of $0.8^{+0.7}_{-0.5}$ keV. This result favors the proton origin or little contribution of electrons.

The most plausible scenario is the inner-shell ionization by the locally accelerated CRs at lower energies in MeV energy range (e.g. Valinia et al. 2000, Dogiel et al. 2011, Nobukawa et al. 2015). These CRs also produce the observed gamma-rays in GeV energy range through the π^0-decay mechanism (e.g. Lee et al. 2015). Simultaneously, these CRs bombard with the lowly ionized cold dense molecular clouds and give rise to the 6.4 keV Fe Kα line. To put a test to this scenario, it is useful to compare the energetics of the CR protons estimated separately from the observed gamma-ray flux and the Kα line flux. For the simplest assumption, the

flux of the 6.4 keV line is given by $\frac{1}{4\pi D^2}\sigma_{6.4\ \mathrm{keV}}\, v\, n_{\mathrm{p}}\, N_{\mathrm{H}}$, where $\sigma_{6.4\ \mathrm{keV}}$ is the cross section to produce the 6.4 keV line by protons (Equation 2.46), v and n_{p} are the velocity and density of the protons, respectively. The 6.4 keV flux measured from Kes 79 is 3.0×10^{-6} cm^{-2} s^{-1}. The cross section $\sigma_{6.4\mathrm{keV}}$ has a peak of $\sim 1.3 \times 10^{-26}$ cm^2 hydrogen-atom^{-1} at 10 MeV in solar abundance (see Figure 2.13). If we extrapolate the density of lower energy CRs from the momentum distribution of high energy CRs estimated by Auchettl et al. (2014), the observed 6.4 keV emission is lower than the expected value by about order of magnitude.

Note that the effect of ionization energy loss of CRs is important in MeV energy range in a dense molecular cloud (Lerche &Schlickeiser 1982). On the other hand, the π^0-decay gamma-rays are produced by protons of energies above the pion production threshold (∼280 MeV; Ackermann et al. 2013) and thus are not much affected by ionization losses (Mannheim & Schlickeiser 1994). We assume that the GeV gamma-rays and 6.4 keV X-rays are emitted from the same region of a molecular cloud interacting with the same distribution of CRs accelerated by Kes 79. Figure 7.2 shows a probable picture of Kes 79 whose forward shock is propagating into the molecular cloud. In this assumption, emission of both GeV gamma-rays and the 6.4 keV X-rays and also ionization loss occur at the same region inside the molecular cloud.

7.2.1 Time-dependent Momentum Distribution of Protons

We estimate the momentum distribution of CRs in the molecular cloud taking into account the ionization momentum loss. The proton momentum loss by ionization or excitation of a molecular cloud is calculated from Bethe-Bloch formula taking into account the ionization potential and the chemical composition (e.g. Schuppan et al. 2012):

$$\dot{p} \equiv \frac{\mathrm{d}p}{\mathrm{d}t} = -1.5 \times 10^{-16} n p^{-2} \left[\frac{\mathrm{GeV}/c}{s}\right] \tag{7.5}$$

$$\equiv -k n p^{-2} \tag{7.6}$$

where n is the number density of the molecular cloud. Protons which have low kinematic energy rapidly lose their energy by ionization ($\equiv p^{-2}$) and the ionization loss timescale for protons is calculated as

$$\tau_{\mathrm{i}} = |\dot{p}|^{-1} p \sim 3.3 \times 10^7 \left(\frac{n}{200\ \mathrm{cm}^{-3}}\right)^{-1} \left(\frac{p}{10\ \mathrm{MeV}/c}\right)^3\ \mathrm{s} \tag{7.7}$$

Assuming $n = 200$ cm^{-3}, the ionization timescale of ~ 10 MeV protons which efficiently excite the 6.4 keV (see Section 2.4) is a few years.

The time-dependent momentum distribution of CRs is described by the following kinetic equation:

$$\frac{\partial}{\partial t} N(p,t) + \frac{\partial}{\partial p}[\dot{p} N(p,t)] = Q(p), \tag{7.8}$$

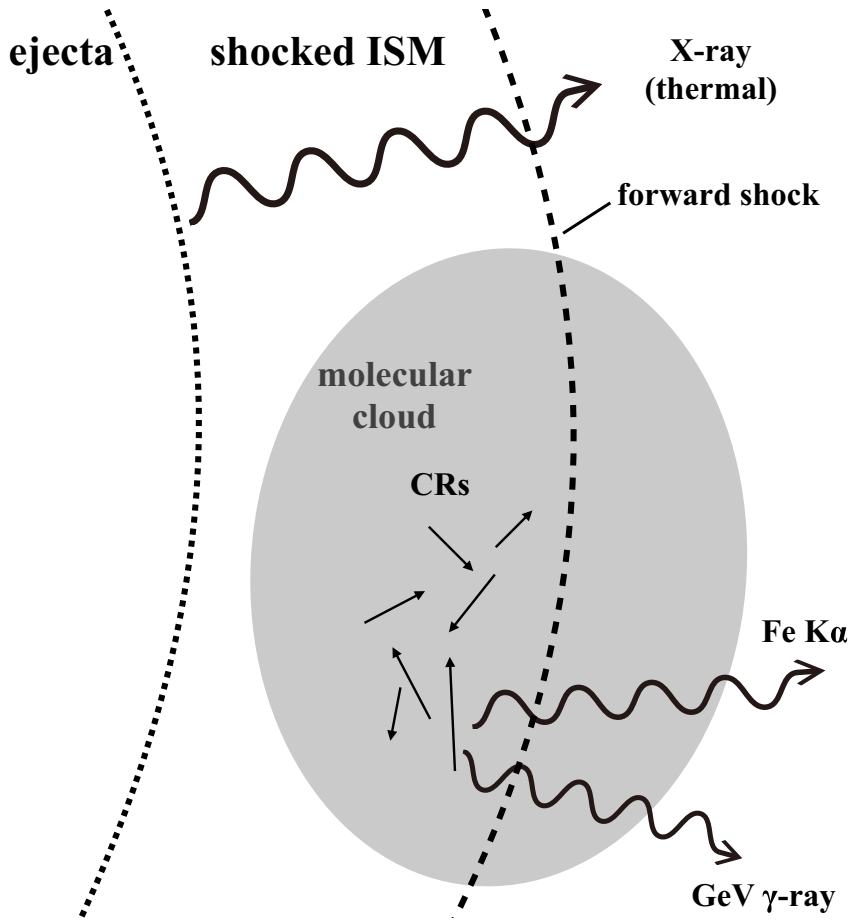

Figure 7.2: The probable scenario in Kes 79. The dashed and dotted lines indicate the forward and reverse shocks, respectively. The gray region is shocked molecular clouds in which CRs are accelerated. The Fe Kα line and GeV gamma-rays are simultaneously emitted by the interaction with molecular cloud different from the region emitting X-rays from thermal plasma.

where $N(p,t)$ is the time-dependent momentum distribution of protons and $Q(p) = Qp^{-\alpha}$ is the proton injection rate by acceleration. For $p \gg 10$ MeV/c, $\dot{p}$ is negligible and the second term on the LHS goes away, and injection Q alone dictates the evolution of N. We can analytically solve this differential equation parameterized by changing variable from time t to momentum p' as follows:

$$t = \int_p^{p'} \frac{\mathrm{d}p''}{|\dot{p}(p'')|} \tag{7.9}$$

$$N(p,t) = \frac{1}{|\dot{p}_{\mathrm{i}}(p)|} \int_p^{p'} Q(p'')\mathrm{d}p''. \tag{7.10}$$

Then, we can obtain

$$N(p,t) = \frac{1}{knp^{-2}} \int_p^{p'=(p^3+3k\ nt)^{1/3}} Qp''^{-\alpha}\mathrm{d}p'' \tag{7.11}$$

$$= \frac{p^2 Q}{kn(\alpha-1)} \left[p^{-(\alpha-1)} - (p^3 + 3k\ nt)^{-(\alpha-1)/3}\right]. \tag{7.12}$$

As a result, the momentum distribution depends on the product of the target density and time (nt). Figure. 7.3 shows a plot of the normalized evolution spectrum with the proton injection index of 4 (DSA; see Section 2.3.2) taking into account the derived exponential cutoff of Kes 79 (Auchettl et al. 2014). We see that low energy CRs lose their energy along with the increase of nt.

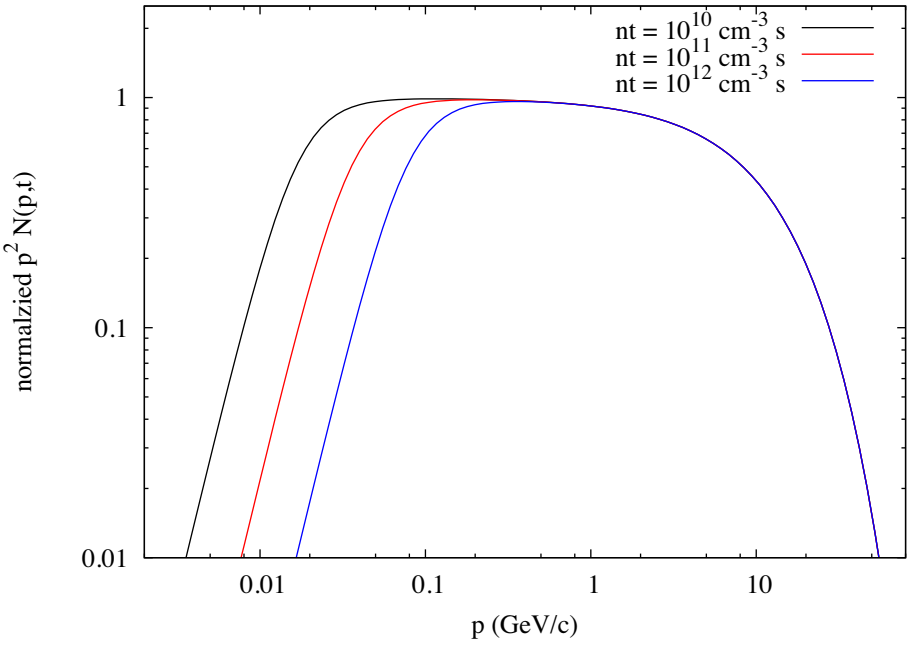

Figure 7.3: The normalized momentum spectrum of the constructed model.

7.2.2 GeV Gamma-ray spectrum of Kes 79

The distribution of high energy CRs above ∼280 MeV, which can produce π^0 emitting gamma-ray (Ackermann et al. 2013), can be estimated from the observed GeV gamma-ray spectrum. Analysis of *Fermi* data by Auchettl et al. (2014) revealed a hadronic origin for the GeV gamma-rays. They also reported that the photon spectrum can be well-described by a cutoff power-law with an photon index of 2.00 ± 0.38 and cutoff energy of 2.71 ± 0.64 GeV. Assuming a purely hadronic scenario, the underlying momentum distribution of the CR protons is a power-law with an exponential cutoff:

$$N(p) = 4\pi A p^{-a} \exp\left(-\frac{p}{p_{\rm cut}}\right), \tag{7.13}$$

where A, $a(=\alpha-2)$ and $p_{\rm cut}$ are the normalization value, the momentum index and the cutoff, respectively. The gamma-ray flux ($F_\gamma(E)$) can be calculated as follows:

$$F_\gamma(E) = n\mu_{pp}\frac{1}{4\pi D^2}\int_0^\infty N(p)\frac{{\rm d}\sigma(K(p),E)}{{\rm d}E}\, v_{\rm p}(p)\, {\rm d}p \ [{\rm GeV}^{-1}\ {\rm cm}^{-2}\ {\rm s}^{-1}], \tag{7.14}$$

where D and $v_{\rm p}$ are the distance to the SNR and the velocity of each protons, ${\rm d}\sigma(K,E)/{\rm d}E$ is the differential cross section of π^0-decay gamma-ray emission (Kamae et al. 2006). A factor of $\mu_{pp} = 1.85$ is to take helium and heavier nuclei into account, as suggested by Mori (2009). Here, we assume an isotropy of momentum in the phase space. Using $D = 7$ kpc, we fit this emission model to the GeV gamma-ray fluxes derived by Auchettl et al. (2014). Figure 7.4 and Table 7.1 show GeV gamma-ray spectrum with the best-fit model and the best-fit parameters.

Table 7.1: Best-fit parameters of the proton momentum distribution derived by fitting the Fermi data (see Figure 7.4)*.

parameter	
$A/(D^2/\mu_{\rm pp})$	$1.9 \pm 0.2 \times 10^8$
α	4.07 ± 0.04
$p_{\rm cut}$ (GeV/c)	12 ± 10

* The uncertainties are the 90% confidence range.

7.2.3 Observational Constraints on Momentum Distribution of Low Energy Cosmic-rays

To explain both the 6.4 keV and the GeV gamma-rays of GeV bright SNRs, we construct the unified model where input parameters are flux of the 6.4 keV and a GeV gamma-ray spectrum

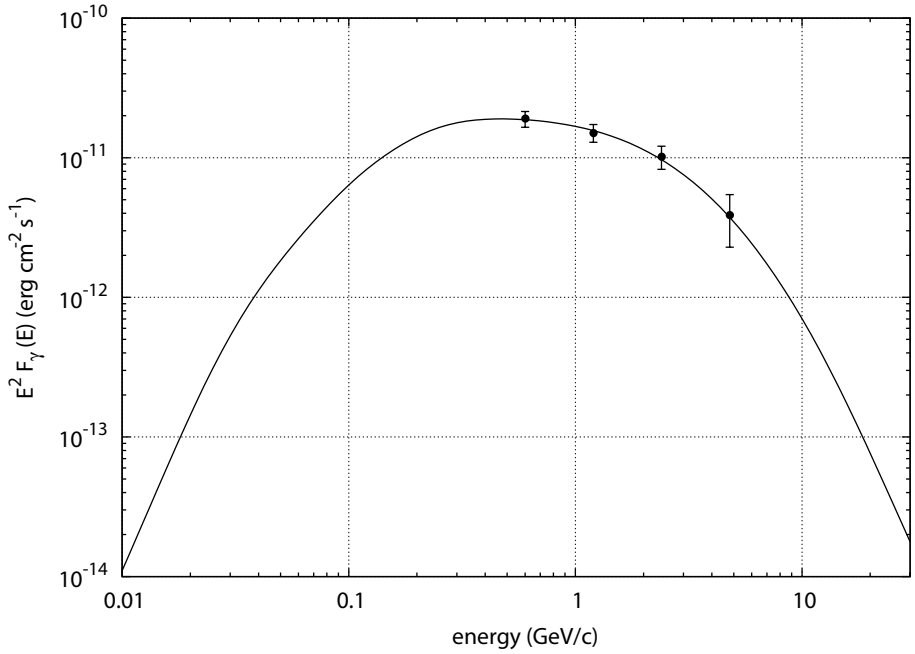

Figure 7.4: The best-fit spectrum of GeV gamma-ray emission from Kes 79. The GeV fluxed shown by black dots are taken from Auchettl et al. (2014).

based on Equation 2.45, 7.12 and 7.14, assuming the emission and loss occur at the same region inside of a molecular cloud. We can obtain the unknown parameter nt cm^{-3} s by our model. We obtain an observational constraint on the momentum distribution of low energy CRs by using the 6.4 keV for the first time.

The black line in Figure 7.5 is the calculated flux of the 6.4 keV as a function of nt using the best-fit value of the GeV spectrum of Kes 79. The red line in Figure 7.5 indicates the best-fit value of the 6.4 keV flux (3×10^6 photons cm^{-3} s^{-1}). We fit the constructed model to the observational result of Kes 79 and finally obtain nt value of $1.8^{+4.8}_{-1.3} \times 10^9$ cm^{-3} s. If the density of molecular cloud is 200 cm^{-3}, time t is a month to a year which is much lower than the estimated age of Kes 79 (2.7×10^4 yr in Section 5.3.2). If the molecular cloud is clumpy as shown in Figure 7.6, the energy loss of some low energy CRs is lower than that in dense clumps. If CRs avoiding ionization loss emit the 6.4 keV line at the dense clamp, we can explain the apparent low nt value. Our model is here the simplest one-zone model. We are ignoring the time evolution of $Q(p_{\rm cut}, A, \alpha)$, the hydro evolution of the shocked cloud, clumpiness of the cloud, different densities sampled by the GeV and 6.4 keV emitting CRs because of their different penetration power in dense clumps and more. We need more improvement of our model to explain what really happens in the GeV-bright SNRs.

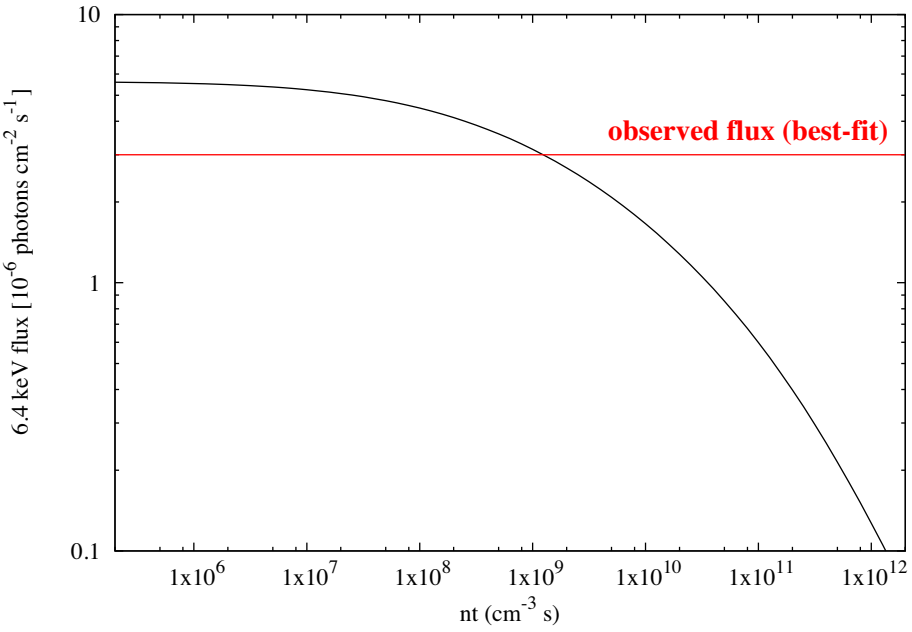

Figure 7.5: The calculated flux of the 6.4 keV whose model parameters are fixed to the best-fit value (summarized in Table 7.1) as a function of nt indicated as the black line. The red line indicates 3×10^{-6} photons cm^{-2} s^{-1} as the best-fit flux of the 6.4 keV detected in Kes 79.

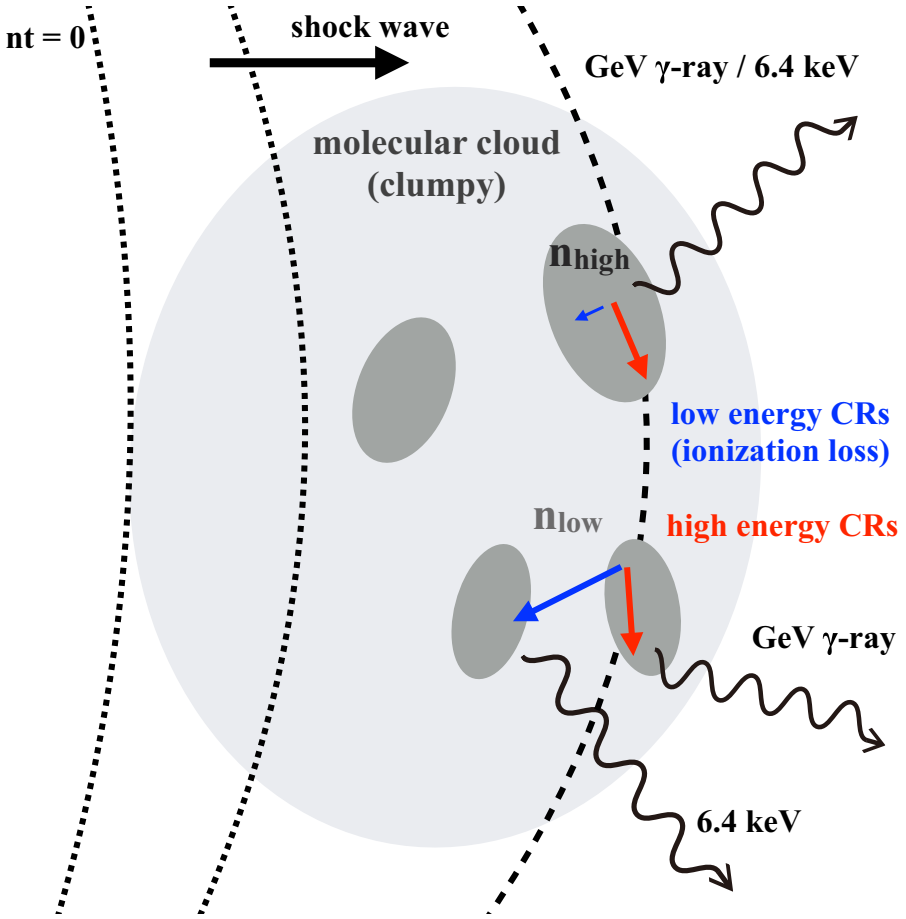

Figure 7.6: The interpreted picture of the emission from Kes 79 on the basis of our model. The SNR shock wave propagate from left to right. The accelerated low energy CRs lose their energy through the ionization depending on the density of the molecular clumps.

Chapter 8

Conclusions and Future Work

We analyzed the Suzaku X-ray data of four Scutum Arm SNRs (3C 391, Kes 79, Kes 78 and W44) observed with Suzaku satellite. The total observation time is about 697 ksec for this systematic study. In the observed region (l = 32–35°, $b \sim 0°$; see Figure 1.1), the GRXE background emission is comparable to the SNR flux, and hence it is essential to evaluate the contamination. We carefully estimated X-ray flux of the SNRs by reducing the uncertainties of the background subtraction.

8.1 Thesis Summary

The Suzaku data analysis of the SNR 3C 391 shows that the soft X-ray (< 3 keV) is enhanced at the east region outside of the radio shell. By using one-temperature plasma model in CIE to fit the X-ray spectrum of 3C 391, we found a significant excess at < 1.5 keV, 2.006 keV line and the hump-like structure around 2.5 keV. Instead, we obtained a reasonable fit with the model of CIE+RP model with χ^2/ d.o.f ~ 1.15. The best-fit parameters show no significant differences between the east and west region of 3C 391.

The Suzaku X-ray images of SNR Kes 79 show the partially shell-like (0.7–1.5 keV) and center-filled (2.0–4.0 keV) spatial structures. The best-fit plasma model of Kes 79 is the CIE+multi-temperature NEI model. Different from other GeV-bright SNRs, Kes 79 shows no RRC emission. We found that the apparent diameter of the low temperature plasma (CIE) is twice as large as that of the high-temperature component (NEI). The ~ 6.4 keV emission is concentrated at the direction of the molecular cloud. We discovered the neutral or lowly-ionized iron Kα emission (~ 6.4 keV) with the significance level of 3.5σ.

Our results of the systematic study in the Scutum Arm SNRs are summarized in Table 8.1. All of these GeV-bright SNRs are core-collapse SNRs with the molecular interaction and radio-bright shell. The SNRs with the RP show the center-filled X-ray and the strong molecular

interaction indicated by the OH maser. From Kes 79, we discovered the ∼6.4 keV excess emission with the significance level of 3.5σ, and we obtained a strong hint of the 6.4 keV emission with the significance level of 2.1σ–2.4σ from the other GeV-bright SNRs.

Table 8.1: The systematic review of the 4 Scutum Arm SNRs*.

SNR	MC*1	OH maser	GeV	radio*2	X-ray*2	RP	SN type*3	6.4keV
3C 391	◯	◯	◯	shell	center	◯	CC	△
Kes 79	◯	×	◯	shell	center & shell	×	CC	◯
Kes 78	◯	◯	◯	shell	shell	×	CC	△
W44	◯	◯	◯	shell	center	◯	CC	△

*◯, △ and × indicate "detect", "possible" and "not-detect", respectively.

*1The association with molecular clouds.

*2The emission structure, shell-bright or center-filled.

*3The estimated supernova type, Type Ia or core-collapse (CC).

8.2 Future Work

In the case of Kes 79, the plausible origin of the 6.4 keV emission is the excitation by low energy CR-protons. The X-ray, CR-electrons and hot ejecta origin is unlikely to explain the ∼ 6.4 keV. The number density of the low energy CR-protons is lower than that extrapolated from the high energy CR-protons possibly due to the ionization loss. We constructed the time-dependent model to calculate the evolution of the momentum distribution of the CRs. We applied the constructed model to Kes 79, then we obtained the nt value as $1.8^{+4.8}_{-1.3} \times 10^9$ cm^{-3} s. This low nt is interpreted as that the molecular cloud interacted with Kes 79 is clumpy.

In order to draw a more conclusive picture of GeV bright SNRs, we need deeper observations. The next-generation X-ray satellite "ASTRO-H" is scheduled to be launched in 2016 (Takahashi et al. 2010). Since ASTRO-H has capabilities to observe Fe Kα lines with higher energy resolution, we can confirm the enhancement of 6.4 keV with more confident level. Moreover, ASTRO-H can observe the hard X-ray band above 10 keV with high sensitivity. We can probably detect the non-thermal Bremsstrahlung (see Section 2.4.1) because the GRXE no longer contributes to this energy range. If this is the case, we can directly observe the energy spectrum of accelerated protons. In order to know what really happens in GeV-bright SNRs, we also need to improve the numerical model of the SNR evolution, the CR acceleration and X-ray/gamma-ray emissions. In any case, if the origin of the 6.4 keV emission of GeV-bright SNRs

is the excitation by low energy CRs, the Kα X-rays from neutral or lowly ionized Fe become a direct probe of low energy CRs which are important for completing our understanding of CR acceleration processes.

Bibliography

Abdo, A. A., Ackermann, M., Ajello, M., et al. 2009, ApJL, 706, L1

Abdo, A. A., Ackermann, M., Ajello, M., et al. 2010, ApJ, 712, 459

Abdo, A. A., et al. 2010, ApJ, 718, 348

Abdo, A. A., et al. 2010, ApJ, 722, 1303

Abdo, A. A., Ackermann, M., Ajello, M., et al. 2010, Science, 327, 1103

Ackermann, M., Ajello, M., Allafort, A., et al. 2013, Science, 339, 807

Aharonian, F. A., et al. 2004, Nature, 432, 75

Aharonian, F., Akhperjanian, A. G., Bazer-Bachi, A. R., et al. 2007, A&A, 464, 235

Anders, E., & Grevesse, N. 1989, Geochim. Cosmochim. Acta, 53, 197

Arnaud, K. A. 1996, Astronomical Data Analysis Software and Systems V, 101, 17

Auchettl, K., Slane, P., & Castro, D. 2014, ApJ, 783, 32

Basko, M. M. 1980, A&A, 87, 330

Ballantyne, D. R., & Fabian, A. C. 2003, ApJ, 592, 1089

Bell, A. R. 1978, MNRAS, 182, 147

Benson, P. J., & Myers, P. C. 1989, ApJS, 71, 89

Blandford, R., & Eichler, D. 1987, Phys. Rep., 154, 1

Boumis, P., Xilouris, E. M., Alikakos, J., et al. 2009, A&A, 499, 789

Brandt, T. J., Acero, F., de Palma, F., et al. 2015, arXiv:1507.03633

Brickhouse, N. S., Dupree, A. K., Edgar, R. J., Liedahl, D. A., Drake, S. A., White, N. E., & Singh, K. P. 2000, ApJ, 530, 387

Brown, J. C. 1973, Sol. Phys., 28, 151

Cardillo, M., Tavani, M., Giuliani, A., et al. 2014, A&A, 565, A74

Case, G. L., & Bhattacharya, D. 1998, ApJ, 504, 761

Castro, D., & Slane, P. 2010, ApJ, 717, 372

Caswell, J. L., Murray, J. D., Roger, R. S., Cole, D. J., & Cooke, D. J. 1975, A&A, 45, 239

Chen, Y., & Slane, P. O. 2001, ApJ, 563, 202

Chen, Y., Su, Y., Slane, P. O., & Wang, Q. D. 2004, ApJ, 616, 885

Chevalier, R. A. 1974, ApJ, 188, 501

Cioffi, D. F., McKee, C. F., & Bertschinger, E. 1988, ApJ, 334, 252

Claussen, M. J., Frail, D. A., Goss, W. M., & Gaume, R. A. 1997, ApJ, 489, 143

Condon, J. J., Cotton, W. D., Greisen, E. W., Yin, Q. F., Perley, R. A., Taylor, G. B., & Broderick, J. J. 1998, AJ, 115, 1693

Cronin, J. W. 1999, Reviews of Modern Physics Supplement, 71, 165

Decourchelle, A., Sauvageot, J. L., Audard, M., et al. 2001, A&A, 365, L218

Decourchelle, A. 2010, SPIE Newsroom. DOI: 10.1117/2.1201004.002923

Dogiel, V., Chernyshov, D., Koyama, K., Nobukawa, M., & Cheng, K. 2011, PASJ, 63, 535

Emslie, A. G. 1978, ApJ, 224, 241

Fermi, E. 1949, Physical Review, 75, 1169

Figer, D. F., MacKenty, J. W., Robberto, M., et al. 2006, ApJ, 643, 1166

Frail, D. A., Goss, W. M., Reynoso, E. M., Giacani, E. B., Green, A. J., & Otrupcek, R. 1996, AJ, 111, 1651

Gaetz, T. J., & Salpeter, E. E. 1983, ApJS, 52, 155

Gaetz, T. J., Butt, Y. M., Edgar, R. J., et al. 2000, ApJL, 534, L47

Giacani, E., Smith, M. J. S., Dubner, G., Loiseau, N., Castelletti, G., & Paron, S. 2009, A&A, 507, 841

Gosachinskii, I. V., & Khersonskii, V. K. 1985, Ap&SS, 108, 303

Green, D. A. 1989, MNRAS, 238, 737

Green, D. A., & Dewdney, P. E. 1992, MNRAS, 254, 686

Green, D. A. 2014, Bulletin of the Astronomical Society of India, 42, 47

Ghavamian, P., Laming, J. M., & Rakowski, C. E. 2007, ApJL, 654, L69

Gryziński, M. 1965, Physical Review, 138, 336

Hayakawa, S and Kitao, K 1956, Progr. Theor. Phys. 16, 139

Hess, V. F., 1912, Phys.. Z, 13 1084.

Hickox, R. C., & Markevitch, M. 2006, ApJ, 645, 95

Hickox, R. C., & Markevitch, M. 2007, ApJL, 661, L117

Hillas, A. M. 2006, arXiv:astro-ph/0607109

Ishisaki, Y., et al. 2007, PASJ, 59, 113

Itoh, H., & Masai, K. 1989, MNRAS, 236, 885

Itoh, N., Sakamoto, T., Kusano, S., Kawana, Y., & Nozawa, S. 2002, A&A, 382, 722

Iwamoto, K., Brachwitz, F., Nomoto, K., Kishimoto, N., Umeda, H., Hix, W. R., & Thielemann, F., 1999, ApJS, 125, 439

Kaastra, J. S., Mewe, R., & Nieuwenhuijzen, H. 1996, UV and X-ray Spectroscopy of Astrophysical and Laboratory Plasmas, 411

Karzas, W. J., & Latter, R. 1961, ApJS, 6, 167

Kassim, N. E. 1992, AJ, 103, 943

Kawasaki, M. T., Ozaki, M., Nagase, F., Masai, K., Ishida, M., & Petre, R. 2002, ApJ, 572, 897

Kawasaki, M., Ph.D. thesis; The University of Tokyo

Kinugasa, K., & Tsunemi, H. 1999, PASJ, 51, 239

Kokubun, M., Makishima, K., Takahashi, T., et al. 2007, PASJ, 59, 53

Koralesky, B., Frail, D. A., Goss, W. M., Claussen, M. J., & Green, A. J. 1998, AJ, 116, 1323

Kosack, K., Chaves, R. C. G., & Acero, F. 2011, International Cosmic Ray Conference, 7, 76

Koyama, K., et al. 2007, PASJ, 59, 23

Kundu, M. R., & Velusamy, T. 1972, A&A, 20, 237

Kushino, A., Ishisaki, Y., Morita, U., Yamasaki, N. Y., Ishida, M., Ohashi, T., & Ueda, Y. 2002, PASJ, 54, 327

Lagage, P. O., & Cesarsky, C. J. 1983, A&A, 125, 249

Lee, S.-H., Patnaude, D. J., Raymond, J. C., Nagataki, S., Slane, P. O., & Ellison, D. C. 2015, ApJ, 806, 71

Lerche, I., & Schlickeiser, R. 1982, MNRAS, 201, 1041

Mangum, J. G., & Shirley, Y. L. 2015, PASP, 127, 266

Mannheim, K., & Schlickeiser, R. 1994, A&A, 286, 983

Masai, K., Dogiel, V. A., Inoue, H., Schönfelder, V., & Strong, A. W. 2002, ApJ, 581, 1071

McKee, C. F. 1974, ApJ, 188, 335

McKee, C. F., & Ostriker, J. P. 1977, ApJ, 218, 148

Miceli, M., Bocchino, F., Decourchelle, A., Ballet, J., & Reale, F. 2010, A&A, 514, L2

Minkowski, R. 1939, ApJ, 89, 156

Mitsuda, K., Bautz, M., Inoue, H., et al. 2007, PASJ, 59, 1

Morrison, R., & McCammon, D. 1983, ApJ, 270, 119

Mott, N. F and Massey, H. S. W 1965, The Theory of Atomic Collisions, Oxford University Press, 3rd ed., p.516

Nobukawa, M., Koyama, K., Tsuru, T. G., Ryu, S. G., & Tatischeff, V. 2010, PASJ, 62, 423

Nobukawa, K. K. et al. 2015, ApJ, 807, 10

Nomoto, K. 1982, ApJ, 253, 798

Ohira, Y., Murase, K., & Yamazaki, R. 2010, A&A, 513, A17

Ohira, Y., Murase, K., & Yamazaki, R. 2011, MNRAS, 410, 1577

Ohnishi, T., Koyama, K., Tsuru, T. G., Masai, K., Yamaguchi, Hiroya., & Ozawa, M., 2011, PASJ, 63, 527

Ozawa, M., Koyama, K., Yamaguchi, H., Masai, K., & Tamagawa, T. 2009, ApJL, 706, L71

Petre, R., Kuntz, K. D., & Shelton, R. L. 2002, ApJ, 579, 404

Putze, A., Derome, L., Maurin, D., Perotto, L., & Taillet, R. 2009, A&A, 497, 991

Quarles, C. A. 1976, Phys. Rev. A, 13, 1278

Radhakrishnan, V., Goss, W. M., Murray, J. D., & Brooks, J. W. 1972, ApJS, 24, 49

Rea, N., Zane, S., Turolla, R., Lyutikov, M., Götz, D. 2008, ApJ, 686, 1245

Reynolds, S. P., & Moffett, D. A. 1993, AJ, 105, 2226

Reynolds, S. P., Borkowski, K. J., Green, D. A., et al. 2008, ApJL, 680, L41

Rho, J., Petre, R., Schlegel, E. M., & Hester, J. J. 1994, ApJ, 430, 757

Rho, J., & Petre, R. 1998, ApJL, 503, L167

Romo-Kröger, C. M. 1998, Nuclear Instruments and Methods in Physics Research B, 136, 196

Sawada, M., & Koyama, K. 2012, PASJ, 64, 81

Schuppan, F., Becker, J. K., Black, J. H., & Casanova, S. 2012, A&A, 541, A126

Scoville, N. Z., Yun, M. S., Sanders, D. B., Clemens, D. P., & Waller, W. H. 1987, ApJS, 63, 821

Sedov, L. I. 1959, Similarity and Dimensional Methods in Mechanics, New York: Academic Press, 1959

Serlemitsos, P. J., et al. 2007, PASJ, 59, 9

Seta, M., Hasegawa, T., Sakamoto, S., et al. 2004, AJ, 127, 1098

Seward, F. D., Slane, P. O., Smith, R. K., & Sun, M. 2003, ApJ, 584, 414

Shimizu, T., Masai, K., & Koyama, K. 2012, PASJ, 64, 24

Smith, R. K., Brickhouse, N. S., Liedahl, D. A., & Raymond, J. C. 2001, ApJL, 556, L91

Spitzer, L. Jr. 1962, Physics of Fully Ionized Gases 2nd ed. (New York: Wiley)

Stage, M. D., Allen, G. E., Houck, J. C., & Davis, J. E. 2006, Nature Physics, 2, 614

Sugizaki, M., Mitsuda, K., Kaneda, H., et al. 2001, apjs, 134, 77

Sun, M., Seward, F. D., Smith, R. K., & Slane, P. O. 2004, ApJ, 605, 742

Takahashi, T., Abe, K., Endo, M., et al. 2007, PASJ, 59, 35

Takahashi, T., Mitsuda, K., Kelley, R., et al. 2010, Proc. SPIE, 7732, 77320Z

Tanaka, T., Uchiyama, Y., Aharonian, F. A., et al. 2008, ApJ, 685, 988

Tawa, N., et al. 2008, PASJ, 60, 11

Taylor, G. 1950, Royal Society of London Proceedings Series A, 201, 159

Truelove, J. K., & McKee, C. F. 1999, ApJS, 120, 299

Tsunemi, H., & Enoguchi, H. 2002, PASJ, 54, 735

Uchiyama, H. et al. 2009, PASJ, 61, 9

Uchiyama, H., Nobukawa, M., Tsuru, T., Koyama, K., & Matsumoto, H. 2011, PASJ, 63, 903

Uchiyama, Y., Funk, S., Katagiri, H., et al. 2012, ApJL, 749, L35

Uchiyama, H., Nobukawa, M., Tsuru, T. G., & Koyama, K. 2013, PASJ, 65, 19

Uchida, H., et al. 2012, PASJ, 64, 141

Uchida, H., Yamaguchi, H., & Koyama, K. 2013, ApJ, 771, 56

van Paradijs, J., Sztajno, M., Lewin, W. H. G., et al. 1986, MNRAS, 221, 617

Valinia, A., Tatischeff, V., Arnaud, K., Ebisawa, K., & Ramaty, R. 2000, ApJ, 543, 733

Valinia, A., Tatischeff, V., Arnaud, K., Ebisawa, K., & Ramaty, R. 2010, ApJ, 543, 733

Velázquez, P. F., de la Fuente, E., Rosado, M., & Raga, A. C. 2001, A&A, 377, 1136

Velusamy, T., Becker, R. H., & Seward, F. D. 1991, AJ, 102, 676

Vink, J. 2008, ApJ, 689, 231

Vink, J. 2012, A&AR, 20, 49

Yamaguchi, H., Ozawa, M., Koyama, K., Masai, K., Hiraga, J. S., Ozaki, M., & Yonetoku, D. 2009, ApJL, 705, L6

Yamaguchi, H., Bamba, A., & Koyama, K. 2009, PASJ, 61, 175

Yamaguchi, H., Ozawa, M., & Ohnishi, T. 2012, Advances in Space Research, 49, 451

Yamaguchi, H., Koyama, K., & Uchida, H. 2012, arXiv:1202.1594

Yamauchi, S., Nobukawa, M., Koyama, K., & Yonemori, M. 2013, PASJ, 65, 6

Yasumi, M., Nobukawa, M., Nakashima, S., Uchida, H., Sugawara, R., Tsuru, T. G., Tanaka, T., Koyama, K. 2014, PASJ, 59

Yamaguchi, H. et al. 2014, ApJL, 785, LL27

Yusef-Zadeh, F., Muno, M., Wardle, M., & Lis, D. C. 2007, ApJ, 656, 847

Webbink, R. F. 1984, ApJ, 277, 355

Wilner, D. J., Reynolds, S. P., & Moffett, D. A. 1998, AJ, 115, 247

Wolszczan, A., Cordes, J. M., & Dewey, R. J. 1991, ApJL, 372, L99

Woosley, S. E., & Weaver, T. A. 1995, ApJS, 101, 181

Zhou, P., & Chen, Y. 2011, ApJ, 743, 4

Zhou, X., Miceli, M., Bocchino, F., Orlando, S., & Chen, Y. 2011, MNRAS, 415, 244

Zhou, P., Chen, Y., Li, X.-D., et al. 2014, ApJL, 781, L16

Acknowledgement

I thank to all people supporting my dissertation. I deeply appreciate the guidance by my supervisor Professor Tadayuki Takahashi. I have been given many opportunities to grow professionally through an encounter with many researchers. I would like to express my deep gratitude to Professor Katsuji Koyama for providing me with a deep insight into the analysis and nature of supernova remnants. I am very much thankful to Dr. Shiu-Hang Lee for many helpful discussion especially the theoretical model of supernova remnants. I thank Dr. Yasuyuki Tanaka for carefully reading this dissertation and encouraging me. I am very grateful to the members of the high energy astrophysics laboratory at the Institute of Space and Astronautical Science and the cosmic-ray laboratory in Kyoto University. I also express sincere thanks to all the Suzaku team members.

Tamotsu Sato